

Interfacing EuO in confined oxide and metal heterostructures

Patrick Lömker

Schlüsseltechnologien / Key Technologies

Band / Volume 174

ISBN 978-3-95806-337-2

Forschungszentrum Jülich GmbH
Peter Grünberg Institut (PGI)
Elektronische Eigenschaften (PGI-6)

Interfacing EuO in confined oxide and metal heterostructures

Patrick Lömker

Schriften des Forschungszentrums Jülich
Reihe Schlüsseltechnologien / Key Technologies

Band / Volume 174

ISSN 1866-1807

ISBN 978-3-95806-337-2

Bibliografische Information der Deutschen Nationalbibliothek.
Die Deutsche Nationalbibliothek verzeichnet diese Publikation in der
Deutschen Nationalbibliografie; detaillierte Bibliografische Daten
sind im Internet über <http://dnb.d-nb.de> abrufbar.

Herausgeber und Vertrieb: Forschungszentrum Jülich GmbH
Zentralbibliothek, Verlag
52425 Jülich
Tel.: +49 2461 61-5368
Fax: +49 2461 61-6103
zb-publikation@fz-juelich.de
www.fz-juelich.de/zb

Umschlaggestaltung: Grafische Medien, Forschungszentrum Jülich GmbH

Druck: Grafische Medien, Forschungszentrum Jülich GmbH

Copyright: Forschungszentrum Jülich 2018

Schriften des Forschungszentrums Jülich
Reihe Schlüsseltechnologien / Key Technologies, Band / Volume 174

DE 290 (Diss. Dortmund, Univ., 2017)

ISSN 1866-1807
ISBN 978-3-95806-337-2

Vollständig frei verfügbar über das Publikationsportal des Forschungszentrums Jülich (JuSER)
unter www.fz-juelich.de/zb/openaccess.



This is an Open Access publication distributed under the terms of the [Creative Commons Attribution License 4.0](https://creativecommons.org/licenses/by/4.0/), which permits unrestricted use, distribution, and reproduction in any medium, provided the original work is properly cited.

Kurzzusammenfassung

EuO ist ein ferromagnetischer Isolator, eine seltene Materialklasse, welche ferromagnetische und isolierende Eigenschaften verbindet. Wir präparieren EuO schichten auf SrTiO₃ (001) und anderen Oxiden in dem wir einen neuen Ansatz, die Redox Reaktion mit dem Substrat, verwenden. Indes entwickeln wir eine XPS Anpassungsroutine auf der Basis vorher gemessener Spektren des Eu 3d Kernniveaus. Die Redox Wachstumsmethode funktioniert im Temperaturbereich $T_S = 300\text{ }^\circ\text{C}-600\text{ }^\circ\text{C}$, in dem wir stöchiometrisches EuO erhalten, abzüglich einer kleiner überoxidierten Region nahe der Grenzfläche. Wir analysieren die Wachstumsrate und finden ein Mott-Cabrera-artiges Wachstum, welches durch die ionische Sauerstoffleitfähigkeit des Substrates begrenzt wird. Die Kristallstruktur wird analysiert und wir finden eine epitaktische Beziehung von EuO(110)/SrTiO₃(100) und EuO(001)/SrTiO₃(001). Die magnetischen Eigenschaften sind vergleichbar mit denen von "bulk" EuO und eine maximale Schichtdicke von $d_{\text{EuO}}=15\text{ nm}$ wird beobachtet. Die hier vorgestellte Methode reduziert die Komplexität des Wachstums, da die Sauerstoffpartialdruckkalibration wegfällt. Um Filme $d > 15\text{ nm}$ zu erhalten lässt sich die bekannte adsorptionslimitierte Methode, nachdem das Redox Wachstum abgeschlossen ist, verwenden.

Die elektronischen Eigenschaften von EuO/Oxid Heterostrukturen und EuO/Metall Grenzflächen werden analysiert. Indem ARPES an EuO/SrTiO₃ gemessen wird, entdecken wir ein 2DEG, welches mit der Literatur von LAO/SrTiO₃ übereinstimmt. Unsere Messung erweitert die bisherigen Arbeiten in zwei Gesichtspunkten, insofern, als dass wir ein 2DEG durch eine kontrollierte Redox Reaktion an der Grenzfläche hervorrufen und nun eine magnetische Wechselwirkung direkt am 2DEG angekoppelt ist. In einer weiteren Messung beobachten wir ein weiteres 2DEG, jedoch nun an der EuO/BaTiO₃ Grenzfläche. Das besondere Interesse liegt hierin begründet, als dass andere Studien zeigten, dass für ein BaTiO₃ 2DEG die ferroelektrischen Eigenschaften des BaTiO₃ erhalten bleiben. Andererseits ist das EuO/BaTiO₃ Interface dafür bekannt, dass der Magnetismus von der im Substrat herrschenden ferroelektrischen Polarisation abhängt. An der dritten Grenzfläche, EuO/Pt wird ein gegenteiliger Effekt, ein 2DHG, vorausgesagt. Wir messen mit HAX-MCD die elementspezifischen magnetischen Eigenschaften und finden eine erhöhte Curietemperatur. Diese wird erwartet für genau die Wechselwirkung, welche auch zu dem 2DHG führt, welches wir als erstes Anzeichen für das Vorhandensein des vorausgesagten 2DHG verstehen.

Im letzten Teil werden die magnetischen Eigenschaften von Co/EuO, erneut elementspezifisch, mit XMCD studiert. Wir benutzen die Summenregeln, welche auch für Seltene Erden angewendet werden können. Hiermit bestimmen wir die Austauschwechselwirkungslänge $2\lambda_{AFM} = (5.6 \pm 1.4)\text{ nm}$. Dies zeigt, dass sich der Effekt nur auf dünne EuO Filme auswirkt. Indem wir eine Hystereseschleife messen, entdecken wir auch Ferromagnetismus an Raumtemperatur, was deutlich über der Curietemperatur von EuO $T_C = 69\text{ K}$ liegt. Wir benutzen die Daten der Hysterese um die Stärke der Austauschwechselwirkung zu bestimmen und erhalten $J = 0.278\text{ meV} \approx 5J_{\text{bulk}}$. Wir ordnen diesen Effekt als magnetischen Nachbarschaftseffekt ein. Auch ultra-dünne filme $d_{\text{EuO}} = 2\text{ ML}$ werden untersucht und zeigen ähnliche Ergebnisse und $M(300\text{ K}) = 1\text{ } \mu_B/\text{f.u.}$, so dass sich mit Sicherheit sagen lässt, dass auch ultra-dünne EuO filme einen Raumtemperaturferromagnetismus durch die Grenzflächenwechselwirkung mit Co erhalten.

Zusammengefasst haben wir eine neuartige Synthesemethode für hochwertiges EuO entwickelt, indem wir eine Substratreduoxreaktion ausnutzen. Dadurch war es uns möglich faszinierende Grenzflächenphänomene in Oxid- und Metallheterostrukturen zu beobachten, welche von zwei-dimensionaler Leitfähigkeit bis hin zu der Entdeckung von Raumtemperatur Ferromagnetismus in EuO Filmen erstrecken. Auf diesem Wege eröffnen sich möglicherweise neue Richtungen im Bezug auf zukünftige EuO Studien.

Abstract

EuO is a ferromagnetic insulator, a rare material class combining ferromagnetic properties and insulating electronic behavior. We synthesize EuO on SrTiO₃ (001) and other oxides using a novel approach, the redox reaction with the substrate. For this we develop a quantitative XPS fitting routine on the basis of a set of Eu 3*d* reference spectra. The redox growth is possible for $T_S = 300^\circ\text{C}$ - 600°C , where we detect stoichiometric EuO except for a small interfacial region. The growth rate was evaluated and we find a Mott-Cabrera like growth limited by ionic oxygen conductivity of the substrate. The crystal structure is analyzed and epitaxial integration of EuO(110)/SrTiO₃ (100) and EuO(001)/SrTiO₃ (001) is obtained. We detect bulk-like magnetic properties and a maximal thickness of $d \approx 15$ nm for this growth method. The proposed growth method reduces the complexity, as the necessity to calibrate the oxygen pressure is circumvented. For films $d > 15$ nm the well known adsorption limited deposition method can be employed after the redox growth.

The electric properties of EuO/oxide and EuO/metal heterostructures are analyzed. Performing ARPES on the EuO/SrTiO₃ interface, we detect a 2DEG which shows comparable properties as the classical 2DEGs like LAO/STO. Our approach provides two novel prospects. First, the preparation of a 2DEG is achieved by a redox-controlled interface reaction and, second, the integration of a ferromagnetic insulator with the 2DEG. Hereby, a 2DEG is prepared in direct contact with a ferromagnet. This interface could be interesting to study the transport properties and elucidate whether the 2DEG is spin-polarized. The integration of EuO with BaTiO₃ was studied in a second experiment. Again, a 2DEG is created by the redox process between Eu metal and BaTiO₃. This interface could be of special interest, as other studies have shown BaTiO₃ to retain its ferroelectric properties at the 2DEG interface, while we find that $d_{\text{EuO}} = 2$ ML exhibits sizable magnetic properties. This combination with a 2DEG at the interface could pave the way towards a multiferroic device, as the EuO/BaTiO₃ interface could influence the magnetic properties as a function of the ferroelectric polarization. The EuO/Pt interface reveals the opposite electric effect. Here a 2DHG is predicted by theoretical modeling and we measure, with element specific HAX-XMCD and volumetric magnetometry, an enhanced Curie temperature. This can be interpreted as a first sign of a magnetic interaction at the EuO/Pt interface, which leads to the 2DHG.

The magnetic properties of Co/EuO heterostructures are studied with XMCD. We find that the sum rules can be applied to this rare earth material. We use this to determine the exchange length at the Co/EuO interface to $2\lambda_{AFM} = (5.6 \pm 1.4)$ nm, which shows, that the effect is localized to the interface and only thin films of EuO will experience the Co/EuO exchange. Measuring a hysteresis loop at room temperature we observe ferromagnetic properties of EuO, far above its bulk $T_C = 69$ K. We utilize the hysteresis loop to obtain the Co/EuO exchange coupling strength $J = 0.278$ meV $\approx 5J_{\text{bulk}}$. We interpret this behavior as a magnetic proximity effect. A EuO ultra-thin film of $d_{\text{EuO}} = 2$ ML is prepared at room temperature and the Co/EuO interface is also studied. We obtain comparable results and $M(300\text{ K}) = 1 \mu_B/\text{f.u.}$. This shows that a significant magnetic moment is retained at room temperature even for ultra-thin EuO films.

In conclusion, we have developed a novel route to synthesize high quality EuO by utilizing a redox reaction with the substrate. This further enabled us to observe fascinating interfacial phenomena in oxide and metal heterostructures ranging from two-dimensional conductivity to magnetic proximity effect induced room temperature ferromagnetism in EuO. This can open up new directions in EuO related research.

Contents

1. Introduction	1
2. Background	5
2.1. The ferromagnetic insulator EuO	5
2.1.1. Properties and synthesis of EuO thin films	5
2.1.2. Magnetism of EuO	7
2.1.3. Spin filtering	8
2.2. Aspects from physical chemistry	10
2.2.1. Ellingham diagram	11
2.2.2. Surface dynamics of SrTiO ₃	12
2.3. Photoelectron and X-ray absorption spectroscopy	14
2.3.1. X-ray absorption spectroscopy	15
2.3.2. Three step model of photoemission	16
2.3.3. Spectral features	19
2.3.4. Implications of hard X-ray photoelectron spectroscopy	21
2.3.5. X-ray magnetic circular dichroism	24
2.3.6. Thickness determination by AR-XPS	25
3. Experiment	27
3.1. Preparation of SrTiO ₃ substrates	28
3.2. Oxide MBE for the preparation of ferromagnetic oxides	30
3.3. Patterning EuO based transport structures	34
3.4. <i>In situ</i> characterization techniques	34
3.4.1. X-ray photoelectron spectroscopy (XPS)	35
3.4.2. Reflection high energy electron diffraction (RHEED)	36
3.4.3. Low energy electron diffraction (LEED)	37
3.5. <i>Ex situ</i> characterization techniques	38
3.5.1. Atomic force microscopy (AFM)	38

3.5.2. Volumetric magnetometry	39
3.5.3. X-ray diffraction and reflection (XRD,XRR)	41
3.6. Synchrotron-based photoelectron spectroscopy	43
3.6.1. Hard X-ray photoelectron spectroscopy	44
3.6.2. UV and soft X-ray angle-resolved photoelectron spectroscopy	45
3.6.3. Soft X-ray absorption spectroscopy and magnetic dichroism	46
Results	46
4. Oxygen-free growth of thin EuO films	49
4.1. From europium to europium-oxide	49
4.2. Stoichiometric growth of EuO on yttria-stabilized zirconia	51
4.3. XPS-based stoichiometry determination of Eu compounds	53
4.4. Determination of the Eu-metal content	55
4.5. Limitations of the distillation condition: EuO/ITO	56
4.6. Oxygen free growth of EuO/SrTiO ₃	68
4.7. Application of oxygen free growth of EuO on other oxides	79
5. Two-dimensional electron gas	83
5.1. Magnetically tunable EuO/SrTiO ₃ 2DEG	83
5.2. Towards multiferroic two-dimensional electron gases: EuO/BaTiO ₃	90
5.3. First indication of a two-dimensional hole gas at the Pt/EuO interface	97
6. Room temperature magnetism of EuO	105
6.1. Co/EuO interfacial magnetism	105
6.1.1. Sum rules and exchange interaction length	106
6.1.2. XAS-MCD results	109
6.2. Room temperature magnetism in ultra-thin Co/EuO interfaces	113
6.3. Origin of the antiferromagnetic Co/EuO exchange interaction?	114
7. Conclusion and Outlook	115
A. Appendix	119
A.1. Umweganregungen	119
Bibliography	121
Acknowledgment	139

CHAPTER 1

Introduction

Today's computer-based electronics has become a major part of our everyday life and to a certain degree shapes the development of our society. The applications of computers are vast and an ever growing portion of energy is devoted to powering information technology related infrastructure. According to a recent study, 270 TWh of energy were annually used by data centers world wide, while an increase of annually 4% is reported in the years 2007-2012 [1]. As the resources for generating power are limited, it is a topical quest to minimize the energy per operation and the number of operation needed to perform a certain task. The first can be influenced by producing what has come to be known as green IT - low powered hardware utilizing less power for the same amount of operations. The latter can be influenced by finding new algorithms that solve existing problems more efficiently.

A second component of the evolution of information technology is the ever increasing demand for storage devices. A well known law is the Moore scaling, where every 2 years the storage capacity per area is doubled. However, there are of course fundamental limitations to this scaling law, as the minimal area per information unit would be reached at one information per atom. Consequently, the search for improved storage technology is equally important. In 2007, the Nobel prize in physics was awarded to Albert Fert and Peter Grünberg for the discovery of the giant magnetoresistance effect (GMR), which can be considered the birth of spintronic research, where the spin degree of freedom is applied in electronics. Indeed, the read heads of current magnetic hard drives are based on the tunnel magnetoresistance effect (TMR), which belongs to the family of magnetoresistance effects explored after the discovery of the GMR effect.

Current computer technology relies on the integration of electronic devices on silicon wafers. The first step towards a silicon-based spintronics, i.e. the injection of spin into Si poses significant challenges, as the resistance mismatch between the substrate and the injection layer frequently limits the achievable spin-polarization to low values

[2]. In this regard, other approaches need to be considered – such as oxide spintronics, a recently developed field in which Si is replaced by oxides such as SrTiO₃, which is considered the workhorse of oxide nano-electronics. In oxide spintronics a rich variety of properties are intrinsically available, ranging from ferroelectricity, to magnetism and interfacial conductivity. By this oxide electronics exceeds silicon nano-electronics in terms of electronic functionalities.

In order to generate spins in oxide electronics, ferromagnetic insulators (FMIs) can be used as a spin filtering tunnel barrier with high spin-polarizations up to 100% [3]. This is due to the combination of insulating behavior and the conduction band splitting caused by the ferromagnetism. The material class of ferromagnetic insulators is small and contains binary oxides, ternary oxides and dichalcogenides. In this regard, a oxide spintronic device based on a ferromagnetic insulator can provide a large spin-polarization. To date, the integration of ferromagnetic insulators on SrTiO₃ has posed significant experimental challenges and often times buffer layers were used [4–6]. This motivates a thermodynamic analysis of the SrTiO₃ and FMI interface to develop a route for a successful integration into the substrate lattice, in order to realize spin injection into oxide electrodes.

The class of magnetic oxides can be broadly categorized in four classes by their magnetic ordering temperature T_C . Europium dichalcogenides (EuO, EuS, EuTe), possess a low $T_C < 70$ K, manganites (BiMnO₃, LaMnO₃, LaSrMnO₃) show close to room-temperature T_C , garnets (Y₃Fe₂(FeO₄)₃, Gd₃Ga₂(GaO₄)₃) have moderate T_C above room temperature and in ferrites (NiFe₂O₄, CoFe₂O₄ and MnFe₂O₄) the ordering temperatures can be as high as $T_C = 865$ K, which largely exceeds room temperature. However, the magnetic ordering temperature is only one critical parameter. The exchange splitting in the conduction band causes the spin-polarization effect and is largest for EuO $2\Delta E_{exch} = 0.6$ eV [7]. The synthesis of EuO/SrTiO₃ is a key component in the preparation of EuO based heterostructures. In fact, the oxygen affinity of EuO, often only recognized as a nuisance in the experimental preparation, can be turned into an advantage by using substrate supplied oxygen, a novel growth method relying on the redox process between Eu metal and SrTiO₃, which will be introduced in this thesis.

In 2004, a fascinating state of matter was found at the LaAlO₃/SrTiO₃ (LAO/STO) oxide interface [8]. Upon deposition of four uc of LAO on STO, a two dimensional electron gas (2DEG) is observed between these two wide band gap insulators. Even though the cause of this 2DEG is still under debate, this has motivated a wide range of 2DEG related research. The observation of a injected spin current into Nb-doped SrTiO₃ [9] has lead the research to find new ways of injecting spin into conductive SrTiO₃. Combining these two effects, first reports of spin-injection into the LAO/SrTiO₃ 2DEG have been reported using a Co over layer as a ferromagnetic polarizator [10]. The success of these experiments, however, is limited by the spin-polarization of the injecting layer – Co with a spin-polarization less than 50%. To operate such a device efficiently, the spin-polarization needs to be as high as possible.

In this regard, EuO is an interesting candidate for spin filtering tunnel barriers on SrTiO₃, as the spin filter efficiency has been demonstrated [3] and calculated to be up to 100% [11]. From a more fundamental point of view, it is also an interesting path to

study the interfacial phenomena of EuO with metals, as predictions of a two dimensional hole gas (2DHG) at the interface of Pt/EuO could simultaneously enhance the Curie temperature and thereby provide one route towards room-temperature ferromagnetism of EuO based devices.

The thesis is structured in the following way. In **Chapter 2**, we first introduce the properties of EuO and its ferromagnetism. Then the theoretical basis for a novel growth mode is addressed, the Ellingham diagram, by which we will govern the suitability of oxidic substrate materials in terms of thermodynamic stability. The different crystalline surface terminations of SrTiO₃, one of the most frequently used oxide substrates in this thesis, have a significant effect on the surface properties. The last part of this chapter is devoted to the introduction of photon-based interactions, which were used to thoroughly characterize the samples and determine electronic, magnetic and chemical properties of bulk EuO and EuO based confined oxide and metal heterostructures.

Next, the experimental setup utilized at the Peter-Grünber-Institute, advanced local characterization techniques and the synchrotron beamlines where experiments were performed are introduced in **Chapter 3**. As a new MBE system was commissioned during the time frame of the thesis, the system is described in detail. Moreover, *in situ* surface science structure determination tools and *ex situ* magnetometry, and X-ray diffraction is described.

The next three chapters present the results, obtained in this thesis. We start from the oxide growth in **Chapter 4**, move on to the aspect of electrical structure in **Chapter 5** and close with results concerning the magnetism of the grown heterostructures in **Chapter 6**.

In **Chapter 4** we first use a well known substrate (yttria-stabilized zirconia) to evaluate the growth of EuO in the new MBE system and develop at the same time a set of reference XPS spectra which we use to quantify the chemical composition of the EuO films. We then present a case using indium tin oxide (ITO) as a substrate, where the well known adsorption limited growth method is not successful due to the thermodynamic properties of the substrate. This apparent disadvantage is utilized in a second step on SrTiO₃ to develop a novel synthesis approach based on a redox process with the underlying oxidic substrate.

These results have enabled an electronic structure study which demonstrates the creation of a 2DEG between EuO/SrTiO₃, where we find that the EuO retains its ferromagnetic properties at the EuO/SrTiO₃ interface. This finding is extended also to BaTiO₃ where a similar behavior is observed, combining ferroelectric and ferromagnetic with interfacial conductivity. Finally, we study the metal/oxide interface of EuO/Pt. This ferromagnetic insulator/metal interface is of interest, as a two dimensional hole gas is predicted at the interface. The enhanced magnetic properties that we observe at this interface are a first sign of the existence of this predicted interface state.

In the last chapter, **Chapter 5**, we study the regular 3d ferromagnet Co integrated with EuO to form a Co/EuO heterostructure. We use the element selective magnetic probe XMCD to elucidate the interfacial magnetism of Co/EuO and find a significant enhancement of T_C up to room temperature and thereby overcome one of the most significant limitations of EuO.

CHAPTER 2

Background

Europium monoxide (EuO) belongs to the rare class of ferromagnetic insulators. The class is defined by the simultaneous existence of ferromagnetic and insulating behavior. In this chapter, the background of this thesis with a focus on properties, preparation and application of EuO is presented in [Section 2.1](#). This approach is based on a controlled chemical reaction as described in [Section 2.2](#). Finally, the main techniques to study the prepared films, i.e. photoelectron and X-ray absorption spectroscopy, are introduced in [Section 2.3](#).

2.1. The ferromagnetic insulator EuO

The general properties of EuO are presented in [Subsection 2.1.1](#). There is an established method for the preparation of EuO thin films that poses a high experimental challenge. This method is here reported and a novel approach to reduce the complexity is introduced in [Section 4.6](#). The magnetic properties of EuO are the deciding parameters for spintronic applications, however, as we show in [Subsection 2.1.2](#), the bulk of EuO is ferromagnetic only below $T_C = 69$ K. EuO can be used to construct spin-electronic devices as described in [Subsection 2.1.3](#).

2.1.1. Properties and synthesis of EuO thin films

Europium monoxide crystallizes in a simple face-centered cubic crystal structure, as rock salt (NaCl) does, with a lattice constant of 5.1420 \AA [[13](#), page ID 53437]. The constituents of EuO are Eu^{2+} and O^{2-} and the Eu atom has an electron configuration of $[\text{Xe}] 4f^7 5d^0 6s^0$. Below the Fermi level, the two contributing valance states are a localized Eu $4f^7$ state and the completely filled O $2p^6$ band.

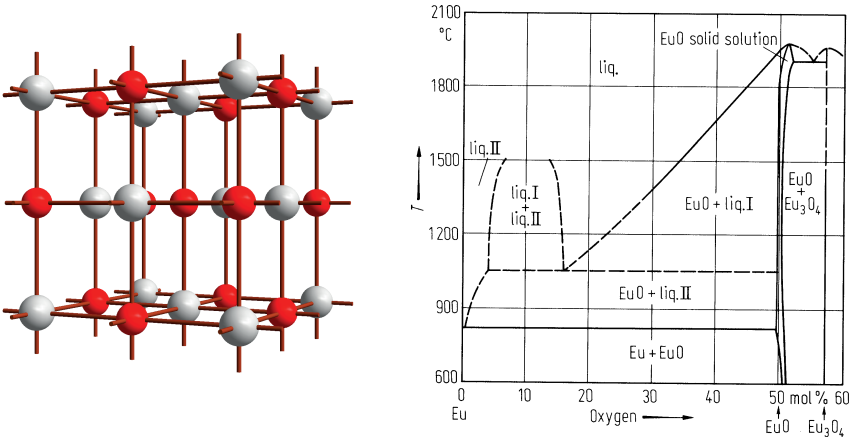


Figure 2.1.: Left: NaCl (rocksalt) crystal structure of EuO. Shown in red are Eu atoms and O atoms in grey. Right: Phase diagram of Eu as a function of temperature T and oxygen content [12].

It is an experimental challenge to synthesize EuO. This is because EuO is not the stable oxide of Eu, which would be Eu_2O_3 (as shown in Section 4.6). Therefore, considerable experimental work has been done in the past to synthesize EuO thin films.

A bulk EuO crystal can be prepared by heating appropriate contents of Eu and O in a tungsten or molybdenum crucible at different temperatures and considering the phase diagram shown in Figure 2.1. As is evident by the very narrow region of stoichiometric EuO, even the preparation of bulk EuO samples is a challenge.

The preparation of EuO thin films on suitable oxide substrates, like yttria stabilized zirconia (YSZ) or YAlO_3 , by MBE posed a significant challenge until the discovery of the adsorption limited synthesis of EuO [14]. Herein the observation of the fact that excess Eu metal can re-evaporate from the EuO surface was utilized. Due to this, the oxygen pressure during the deposition can be reduced below the stoichiometric value and therefore a range of p_{ox} leads to the formation of stoichiometric EuO. In this way, the availability of oxygen is the determining factor for the growth rate and at constant Eu flux, the growth rate of stoichiometric EuO depends directly on the oxygen pressure as can be seen in Figure 2.2.

Over time, this method has been refined and newer approaches have been introduced, as for example the topotactic growth of EuO [15]. Here, epitaxial Eu_2O_3 is sputtered onto YAlO_3 substrates and capped with Ti metal. Then the heterostructure is heated and the oxygen from the Eu_2O_3 reacts with Ti to form TiO , while Eu_2O_3 is reduced to EuO. This method shows a crystalline integration with the substrate and magnetic properties of bulk EuO. However, the method is restricted to using a Ti layer on top. Also the thickness of Eu_2O_3 and Ti need to be controlled carefully, such that a full

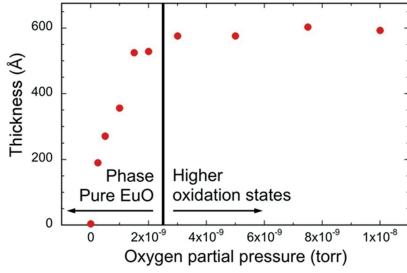


Figure 2.2: Growth rate of stoichiometric EuO using the adsorption limited growth method on YAlO₃ substrates [14].

conversion of the available Ti and Eu₂O₃ is achieved.

2.1.2. Magnetism of EuO

From the electron configuration of EuO $4f^7$, seven unpaired spins are located in the outer shell and lead to $l = 0$ and $s = 7/2$. If EuO fully magnetizes, then a saturation moment of $M_S = 7 \mu_B/\text{f.u.}$ is expected. Europium oxide is a band insulator and considered an ideal Heisenberg ferromagnet, due to the fact that $l = 0$ and only spin-spin interactions govern the magnetic properties.

Within the Heisenberg model of magnetism the Hamiltonian describing the magnetism of the system is given by [16]

$$\mathcal{H} = \sum_{i,j} -J_{i,j} \mathbf{S}_i \mathbf{S}_j \quad (2.1)$$

where $J_{i,j}$ is the exchange interaction strength between site i and j and \mathbf{S}_i is the spin state of the electron at site i . For $J > 0$ a ferromagnetic material is obtained, while $J < 0$ leads to antiferromagnetic behavior. The exchange interaction strength $J_{i,j}$ is determined by the so called exchange-integral, which is a measure for the wave function overlap of the two involved states.

The Bloch law for magnetism is an approximate solution for the aforementioned Hamiltonian and connects the exchange interaction strength J with the Curie temperature T_C so that

$$M(T) = M_S \left[1 - \frac{\alpha}{S} \left(\frac{k_B T}{2SJ} \right)^{3/2} \right] \quad (2.2)$$

where $M(T)$ is the temperature dependent magnetization, k_B is the Boltzmann constant, S is the total spin-moment and M_S is the magnetization of the saturated film. As $M(T_C) = 0$ it follows directly, that $T_C = 2S^{5/3}/(k_B a^{2/3}) \cdot J \propto J$, i.e. the Curie temperature is proportional to the exchange interaction strength.

The shape of $M(T)$ is best described with a Brillouin function [16]

$$M(T) = M_S = a_J \coth(a_J x) - b_J \coth(b_J x) \quad (2.3)$$

$$a_J = \frac{2J+1}{2J}, \quad b_J = \frac{1}{2J} \quad x = \frac{g\mu_B J B}{k_B T} \quad (2.4)$$

To evaluate $M(T)$ curves the Brillouin function is calculated using an available program and plotted for comparison [17].

The origin of the ferromagnetism in stoichiometric EuO has been reported in literature [18]. The dominant parts of the EuO exchange interaction $J_{i,j}$ can be reduced to two contributions J_1 and J_2 , which resemble the indirect exchange and the superexchange mechanisms.

Due to the fact, that EuO has localized $4f$ states, no itinerant direct exchange interactions like RKKY take place. Instead, the indirect exchange between Eu $4f$ and Eu $5d$ on the same Eu site lead to the ferromagnetism in EuO.

The superexchange mechanisms involve the next-nearest neighbor and are therefore transitions of electrons from Eu $4f$ to O $2p$. Three mechanisms are identified: Kramers-Anderson, superexchange via $d-f$ interaction and the so-called crossed term, a mixing of the first two mentioned mechanisms.

The Kramers-Anderson mechanism involves the virtual transfer of an electron from the $4f^7$ level of a next-nearest neighbor via the anion to a $4f^7$ site of a nearest neighbor, while the superexchange via $d-f$ interaction mechanism involves an electron transfer from the anion p to a nearest neighbor Eu site. Finally the indirect exchange interaction acts upon the electron.

The literature reports $J_1 = 5.2 \times 10^{-5}$ eV and $J_2 = 0.1 \times 10^{-5}$ eV [18]. The Curie temperature can be calculated by using [17]

$$T_C = 2/3J(J+1)J_{4f}/k_B = 69 \text{ K} \quad (2.5)$$

for the reported values of $J_{4f} = J_1 + J_2$.

The magnetic properties of thin films can deviate from the bulk, as the exchange interaction relies on the availability of nearest and next-nearest neighbors. In the surface layer, the amount of nearest and next-nearest neighbors is reduced and thereby the local values of J_1 and J_2 are smaller. This has been evaluated in the literature [19] and can be summarized by Figure 2.3. The study shows, that an ideal EuO bulk-like crystal $d > 25$ ML = 6.42 nm exhibits the expected bulk $T_C = 69$ K. Reducing the layer thickness, the influence from the surface layers is enhanced and leads to a reduction of $T_C = 15$ K for $d = 1$ ML.

EuO is regarded as a model system for Heisenberg ferromagnets that exhibits a high magnetization of $7 \mu_B/\text{f.u.}$ at a $T_C = 69$ K.

2.1.3. Spin filtering

Transport structures of the form non-magnetic conductor/ferromagnetic insulator FI/non-magnetic conductor (NC/FI/NC) can act as a spin filtering tunnel barrier as shown in

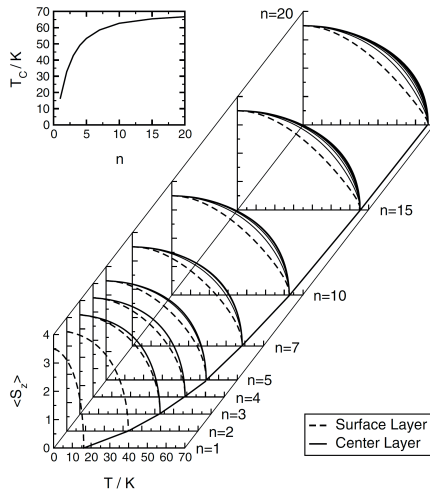


Figure 2.3: Layer dependent magnetization as function of the temperature. The inset shows $T_C(n)$, where n is the number of the n^{th} monolayer [19].

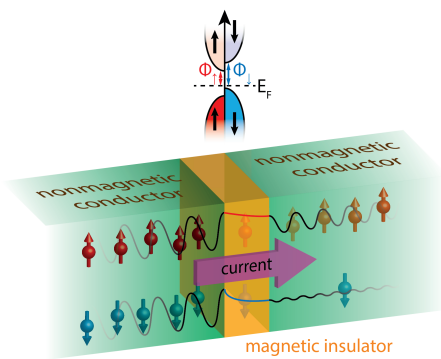


Figure 2.4: Schematic representation of a spin filter tunneling barrier composed of a non-magnetic conductor/magnetic insulator/non-magnetic conductor structure [20].

Figure 2.4. This is due to the spin-split conduction band of the FI. Due to the different tunnel barrier heights $E_T = E_{T,0} \pm E_{exch}$ for spin up and spin down electrons, the transmission probability $T^{\uparrow\downarrow}$ of electrons is either enhanced or suppressed with respect to the transmission for $E_{T,0}$, the tunnel barrier height above T_C where $E_{exch} = 0$.

The transmission probability $T^{\uparrow\downarrow}$ determines the tunnel electron current $I \propto T$ through a tunnel barrier. Using the WKB approximation this can be written as

$$T^{\uparrow\downarrow} \propto \exp\left(2d\sqrt{2m/\hbar^2 \cdot (E_T - E)}\right) \quad (2.6)$$

where d is the thickness of the barrier and E is the energy of the electron. Due to this, the transmission probability is highly dependent on the spin character of the electron and therefore an initially unpolarized electron current is spin-polarized upon its transmission through the tunnel barrier.

The degree of spin-polarization P is given by

$$P = \frac{I_{\uparrow} - I_{\downarrow}}{I_{\uparrow} + I_{\downarrow}} \quad (2.7)$$

where I denotes the current of the respective electron spin character.

In the literature the spin-polarization of thin EuO films was predicted for example on a Cu/EuO/Cu structure by density functional theory in the LDA+U approximation for correlated materials [11]. Here, the authors report a system that combines spin filtering as it was introduced above with a second filtering aspect, namely the so-called symmetry filtering. Symmetry filtering was first observed in the Fe/MgO/Fe system [21], where the symmetry of the transmitting bands in the MgO tunnel barrier causes the spin filter effect. The thickness of the EuO over layer in the Cu/EuO/Cu structure is varied in the range of $d = 15 \text{ \AA}$ to 35 \AA and very high spin polarizations of $P > 90\%$ are reported for the lower limit. For $d = 35 \text{ \AA}$ the report presents a full polarization of $P = 100\%$, demonstrating the suitability of EuO for the construction of ultra-thin tunnel barriers with very high spin-polarization.

2.2. Aspects from physical chemistry

Due to the fact that highly reactive metals such as Sr, Ti and Eu are used it is of importance to study the interaction of all three components to predict, whether chemical reactions between the reagents lead to unwanted products. In this regard, the Gibb's free energy of formation is of importance and can be used as a guide to predict the thermodynamically induced direction of a reaction and is introduced in [Subsection 2.2.1](#)

More over, the surface behavior of SrTiO₃, due to its layered structure, is different depending on the termination and we introduce one aspect in [Subsection 2.2.2](#).

2.2.1. Ellingham diagram

In physical chemistry a so-called Ellingham diagram is commonly used to determine whether an oxidic reaction



will progress in a certain direction, indicated by the direction of the arrows. In this diagram, the Gibbs free energy of formation difference $\Delta_R G^0$ between a product B and its reagents A

$$\Delta_R G^0 = \Delta_R G^0(B) - \Delta_R G^0(A + O_2) \quad (2.9)$$

is plotted as a function of the temperature T normalized to moles of O_2 . If $\Delta_R G^0 < 0$ ($\Delta_R G^0 > 0$) the reaction will progress in to the direction of B (A)



and an oxidation (reduction) reaction is expected to happen.

A prominent example for this Ellingham analysis is the thermite reaction, where iron oxide is reduced to iron by oxidizing aluminum, as described by this reaction $Fe_2O_3 + 2Al \longrightarrow 2Fe + Al_2O_3$. This redox reaction can be analyzed by plotting the two reactions



into one diagram as shown in [Figure 2.5](#). As the Al_2O_3 reaction has a more negative $\Delta_R G^0$ the direction of the reaction is towards this product. In general a reaction is expected to progress if the difference is larger than $\Delta = 250 \frac{\text{kJ}}{\text{mol}}$.

It is important to stress, that these diagrams *only* show which direction is thermodynamically favored and not which reaction is actually taking place, as this is also dependent on the reaction kinetics, i.e. how fast a reaction progresses.

In order to derive an Ellingham diagram from tabulated thermodynamic data it is necessary to calculate $\Delta_R G^0(T)$, because usually only $\Delta_R G^0(T_0)$ is available, i.e. the Gibbs free enthalpy of formation at standard conditions.

It holds, that

$$G(p, T) = H - TS \quad (2.14)$$

where G is the Gibbs free energy, p is the pressure and T is the temperature of the system, while H is the enthalpy and S the entropy. Therefore, $\Delta_R G^0(T)$ can be calculated from $\Delta_R G^0(T_0)$ if $H(T)$ and $S(T)$ are known.

From statistical mechanics it is known that the entropy and free enthalpy behave as

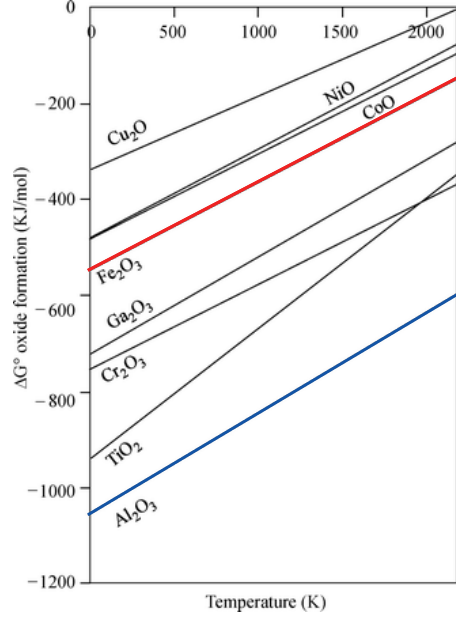


Figure 2.5: Ellingham diagram showing the oxidation reactions of $\frac{4}{3}\text{Fe} + \text{O}_2 \longrightarrow \frac{2}{3}\text{Fe}_2\text{O}_3$ (red) and $\frac{4}{3}\text{Al} + \text{O}_2 \longrightarrow \frac{2}{3}\text{Al}_2\text{O}_3$ (blue) normalized to mol O_2 . Since the $\Delta_R G^0(\text{Al}_2\text{O}_3) < \Delta_R G^0(\text{Fe}_2\text{O}_3)$ a reaction between Al and Fe_2O_3 will reduce Fe_2O_3 producing Al_2O_3 and Fe.

[22]

$$S(T) = S(T_0) + C_p \ln\left(\frac{T}{T_0}\right) \quad H(T) = H(T_0) + C_p(T - T_0) \quad (2.15)$$

where T_0 is the temperature at which $S(T_0)$ and $H(T_0)$ are defined, C_p is constant and represents the heat capacity at constant pressure. The change in Gibbs free energy of formation can then be written as

$$\Delta_R G^0 = H(T_0) + C_p(T - T_0) - T \left(S(T_0) + C_p \ln\left(\frac{T}{T_0}\right) \right) \quad (2.16)$$

This Ellingham analysis is used in [Section 4.5](#) and [Section 4.6](#) to provide a tool for the prediction of the stability of the highly meta-stable europium monoxide on oxidic substrates and can also be extended to predict the chemical stability of other heterostructures.

2.2.2. Surface dynamics of SrTiO_3

The surface properties of SrTiO_3 (001) crystals depend on the surface termination, i.e. TiO_2 or SrO . A parameter that influences the thin film growth is the diffusion of adatoms on a surface. For SrTiO_3 , the diffusion of Sr was studied as a function of the surface termination [23]. In this study, the relative energy for an adatom on the TiO_2 -

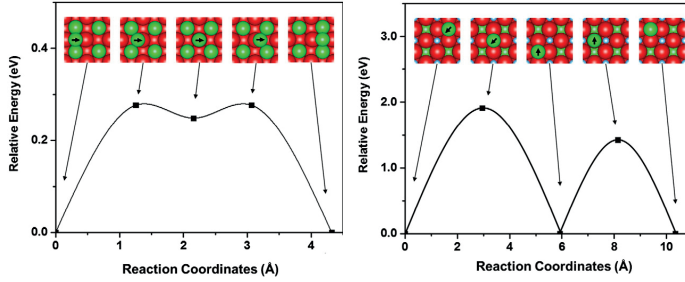


Figure 2.6.: (a) Sr diffusion mechanism for SrO terminated SrTiO₃. (b) Sr diffusion mechanism for TiO₂ terminated SrTiO₃.

and SrO-terminated SrTiO₃ surface was calculated and can be used as a measure for the surface diffusion.

Shown in Figure 2.6 is the surface diffusion mechanism for the (a) SrO- and (b) TiO₂-terminated SrTiO₃ surface. In both cases, the Sr adatom is diffusing over the surface by a hopping mechanism. The energy barrier between two sites is $E_R < 0.3$ eV, while in the latter case $E_R > 1.4$ eV. The distance between jumps a depends on the termination for which $a_{\text{SrO}} = 4.2$ Å and $a_{\text{TiO}_2} = 6$ Å is reported.

The diffusion length d_{RMS} can be estimated as a random walk caused by the thermal activation. In this regard, the energy barrier E_R is necessary to calculate the jump-frequency Γ and the diffusion coefficient D

$$\Gamma = \nu \exp(-E_R/k_B T) \quad D = \frac{a^2 \Gamma}{4} \quad d_{RMS} = \sqrt{Dt} \quad (2.17)$$

here d_{RMS} denotes the average distance a particle travels due to the random walk, k_B is the Boltzmann constant, t is the time and ν the attempt frequency.

We assume, that $\nu_{\text{TiO}_2} = \nu_{\text{SrO}}$ and obtain

$$\frac{d_{\text{SrO}}}{d_{\text{TiO}_2}} = \frac{a_{\text{SrO}}^2}{a_{\text{TiO}_2}^2} \exp(-(E_{R,\text{TiO}_2} - E_{R,\text{SrO}})/k_B T) = 2.6 \times 10^3 \sqrt{t} \quad (2.18)$$

a much faster diffusion on the SrO surface. In this regard, it is interesting to study the over layer growth of EuO on SrTiO₃ using both TiO₂- and SrO-terminated SrTiO₃, as an enhanced crystallization is expected for the first layer of EuO due to the enhanced surface mobility of adatoms on SrO with respect to the TiO₂ termination.

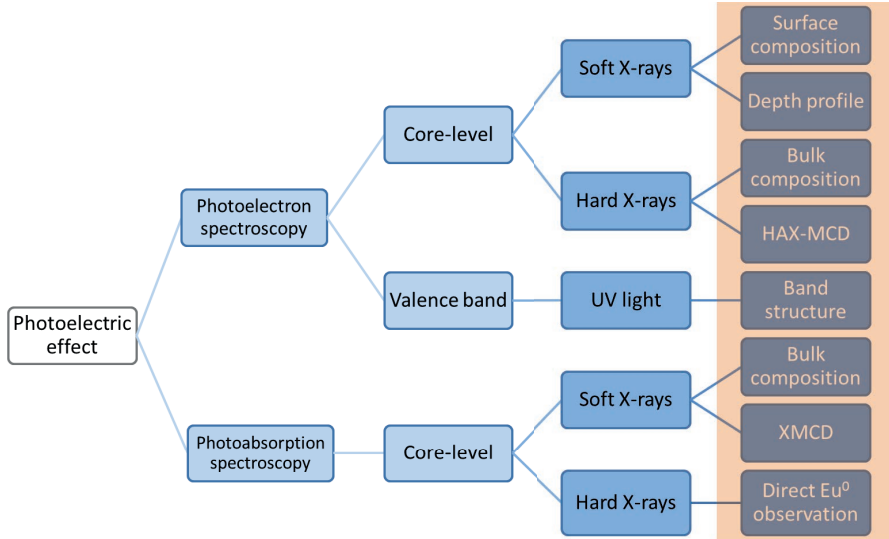


Figure 2.7.: Overview of properties and effects (shown in blue on the right) accessible with techniques based on the photoelectric effect relevant in the scope of this thesis.

2.3. Photoelectron and X-ray absorption spectroscopy

The discovery of the photoelectric effect has led to the development of a powerful technique, which can measure a multitude of properties in an element selective way.

In [Figure 2.7](#) an overview of the properties and effects that can be studied by techniques based on the photoelectric effect (PE) is depicted. All of this is based on the fact, that light quanta (photons) are absorbed by solid material and interact with its electrons. The electrons can either be excited into an unoccupied state, as would be the case in photon absorption or the material can be ionized, where the electron is emitted (photoemission) and the electron intensity $I(E_{kin})$ can be detected (photoelectron spectroscopy) with an electron analyzer as a function of the kinetic energy (angle-integrated photoelectron spectroscopy, see [Subsection 2.3.4](#) and additionally with respect to the angles ϕ, θ (angle-resolved photoelectron spectroscopy, see [Subsection 2.3.2](#)).

Depending on the photon energy E_γ the interaction of the light applies to either core-level electrons or valence-band electrons. Soft ($E_\gamma = 1200 \text{ eV}$ to 1500 eV) and hard ($E_\gamma = 2000 \text{ eV}$ to $10\,000 \text{ eV}$) X-rays interact with deeply bound core-level electrons. Using soft X-ray photoelectron spectroscopy (XPS) information of the surface composition and a limited chemical depth-profiling is available. Hard X-ray photoelectron spectroscopy (HAXPES) has an enhanced probing depth and can be used to study the bulk properties of thin films. Additionally, circularly polarized photons can be employed to study the

hard X-ray photoelectron spectroscopy magnetic circular dichroism (HAX-MCD), an element selective probe for the bulk magnetic properties of a thin film. Photons with smaller energies of $E_\gamma = 10 \text{ eV}$ to 100 eV are used to assess the valence electrons of the material. Due to the fact, that the momentum of the electron in the solid $\hbar\mathbf{k}_{i\parallel}$ is conserved during the emission process, angle-resolved photoelectron spectroscopy (ARPES) can be used to study the valence-band structure and thereby determine the electronic structure.

2.3.1. X-ray absorption spectroscopy

In X-ray absorption spectroscopy experiments the absorption of an X-ray beam through matter is recorded as a function of the photon energy E_γ . According to the Beer-Lambert law of the transmission of (X-ray) light of energy E_γ , is given by

$$I_L(d) = I_{L,0} \exp(-\mu(E_\gamma)d) \quad (2.19)$$

where $I_L(d)$ is the intensity of light transmitted through a material of thickness d , $I_{L,0}$ is the intensity of the light and $\mu(E_\gamma)$ is the linear absorption coefficient. Therefore, the absorption A can be determined from the transmitted intensity as

$$A = \left(1 - \frac{I_L(d, E_\gamma)}{I_{L,0}} \right). \quad (2.20)$$

However, due to the small effective absorption length of X-rays in matter $EAL = 1/\mu(E_\gamma) \approx 100 \mu\text{m}$, experiments in transmission geometry are limited to very thin samples. Instead, the intensity $I(E_\gamma)$ of secondary processes caused by the X-ray absorption is observed. Two processes occur mainly when X-rays are absorbed. Either secondary electrons are emitted or sample fluorescence is observed.

In the first case an Auger excitation takes place and the excited Auger electron travels to the sample surface and escapes into the vacuum. This leads to an electron cascade, as the Auger electrons interact with electrons on their way to the sample surface and cause secondary excitations. These electrons are summed together as the total electron yield (TEY) spectrum and can be measured as a sample current, as electron currents are needed to replace the emitted electrons (charge neutrality). This process is limited to small escape depths, i.e. close to the sample surface, as the inelastic mean free path of the electrons $\lambda_{IMFP}(1000 \text{ eV}) \approx 2 \text{ nm} \ll \lambda_{EAL}$ is much smaller than the X-ray absorption length. A second limitation is imposed by the necessary electron conduction, only conductive samples can be measured without charging effects. In this way, the TEY spectrum resembles the XA spectrum close to the sample surface for conductive samples.

The second case of X-ray fluorescence (XRF) can be measured using an X-ray detector, like Li doped Si crystals. Here the X-rays are absorbed and produce electron hole pairs that can be measured as a current in the detector. The sample fluorescence does not depend on the conductivity of the sample and has a similar effective attenuation length like the incoming photons λ_{EAL} . Therefore, the XRF spectrum contains bulk-like information of the sample and can be used on insulating samples, as well as for conductive

samples.

In the scope of this thesis XAS spectra are recorded with circularly polarized light in order to observe the XMCD effect as described in [Subsection 2.3.5](#).

2.3.2. Three step model of photoemission

The photoemission process can be approximated by the three step model of photo emission. Photoelectron spectroscopy in all energy ranges is based on the fact, that light quanta excite electrons in a solid. These electrons are emitted at a kinetic energy E_{kin} described by the following relation [24]

$$E_{kin} = E_{\gamma} - \Phi - E_B. \quad (2.21)$$

where Φ is the material specific work function. The consequence of this equation is depicted in [Figure 2.8](#) (a). Detecting the electrons as a function of their kinetic energy an electron spectrum $I(E_{kin})$ is obtained and resembles the binding energy of core-level and valence electrons. As shown in [Figure 2.8](#) (b) the angle-resolved spectrum $I(E_{kin}, \phi, \theta)$ can be measured by rotation of the sample along the respective axis (or by using electrostatic lenses and a 2D detector). This is important for the valence-band spectra, as they show a strong dispersion $E(\mathbf{k})$ which can be measured in this way (see [Subsection 2.3.2](#)).

Optical excitation: Fermi's golden rule

In order to understand the spectral features of a photoelectron spectrum, it is necessary to determine the probability of photoexcitation. In this regard the initial state of a solid is described by the ground state (initial state) N electron wave function. After the photoexcitation and the ionization the excited electron, the system is in an excited state described by the $N - 1$ electron wave function (final state). The final state is described by the creation of core hole and the occupation of the N th electron in a (previously) unoccupied state above the Fermi-level E_F .

The correct description of a solid is achieved by solving the many body Hamiltonian \mathcal{H} to obtain all initial and final states $\phi_{i,f}$. This Hamiltonian needs to contain all interactions of all particles in the solid and is consequently very complex and not analytically solvable. Therefore, approximations are introduced. First the interactions in the solid are considered to be small and much slower than the photoemission process (Sudden approximation). This reduces the many body Hamiltonian to the single particle Hamiltonian. Secondly the vector potential of the incoming photon is described by a small perturbation, allowing the treatment with established perturbation theory, as is presented in standard text books [25]. This leads to the derivation of Fermi's golden rule

$$W_{i,f} \propto |\langle \phi_f | \mathbf{T} | \phi_i \rangle|^2 \cdot \delta(E_f - E_i - E_{\gamma}) \quad (2.22)$$

which describes the probability W that an electron is transferred from the ground state ϕ_i to the excited state ϕ_f (here we show the angle integrated form only). The transition is assumed to be an electronic dipole transition induced by the dipole operator \mathbf{T} . The

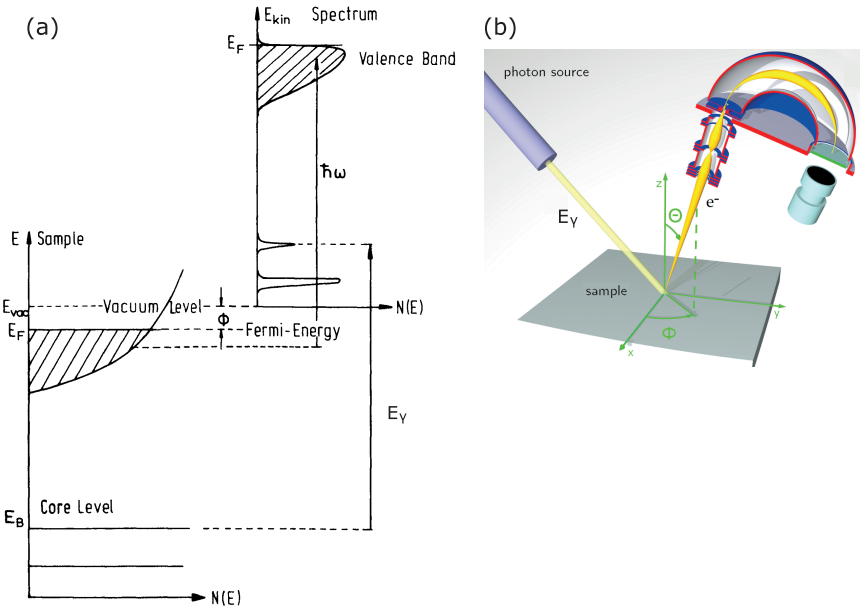


Figure 2.8.: (a) Initial electronic structure of a solid. Excitation of a bound electron with a photon to a state above the vacuum level. This leads to photo-ionization and the electrons can be detected in a spectrum as a function of their kinetic energy E_{kin} . Deeply bound electrons, core-level electrons, are illustrated with a sharp peak due to their localization, while the valence bands show a strong dispersion and are therefore energetically broadened (adapted from [25]) (b) Sketch of a photoemission setup. Photons with energy E_γ irradiate the surface of a sample. The azimuth angle ϕ and polar angle θ with respect to the crystal lattice of the solid are marked and the electron intensity is measured as a function of these $I(E_{kin}, \phi, \theta)$ as described in Subsection 2.3.2.

δ function ensures energy conservation and only allows a transition where the difference is given by the photon energy.

The consequence of the electronic dipole operator \mathbf{T} is that only states fulfilling the dipole selection rules can contribute to the spectrum. The dipole selection rules are given by the difference in the quantum numbers

$$\Delta J = 0, \pm 1 \quad \Delta M_J = 0, \pm 1 \quad \Delta S = 0 \quad (2.23)$$

where J , M_J and S are the total quantum numbers for the total angular momentum, secondary total angular momentum and the spin.

Due to the energy selectivity shown in Equation 2.22 the element selectivity of this technique is achieved, as E_B is often different for different atoms, and also depends on

the chemical environment as shown in [Subsection 2.3.3](#).

Angle-resolved photoelectron spectroscopy

Angle-resolved photoelectron spectroscopy (ARPES) is a technique that enables a measurement of the valence band structure. Herein low energy photons in the UV range ($E_{\Gamma} = 10 \text{ eV}$ to 100 eV) are used to excite the electrons. Due to the lower kinetic energy of the electron the Debye-Wallerfactor is large (see [Figure 2.11](#)) and the information from the dispersion inside the crystal $E(\mathbf{k})$ is conserved. Electrons of different \mathbf{k}_{\parallel} are emitted from the surface under different angles, thereby the measurement of the angular distribution with respect to ϕ, θ of the emitted electrons is a direct observation of \mathbf{k}_{\parallel} . In this regard the observed intensity $I(E, \theta, \phi)$ is given by ¹

$$I(E, \theta, \phi) \propto \sum_{i,f} W_{i,f} \propto \sum_{i,f} |\langle \phi_f | \mathbf{T} | \phi_i \rangle|^2 \underbrace{\delta(\mathbf{k}_i - \mathbf{k}_f + \mathbf{G})}_{\text{momentum conservation}} \underbrace{\delta(\mathbf{k}_{f,\parallel} - \mathbf{K}_{f,\parallel}(\phi, \theta))}_{\text{parallel momentum conservation}} \quad (2.24)$$

This equation demonstrates, that the momentum of the electrons in the plane \mathbf{k}_{\parallel} is conserved upon transmission through the surface and therefore the measured $\mathbf{K}_{\parallel}(\phi, \theta)$ resembles the dispersion of the electron in the solid.

Propagation through the solid

In this step, the excited electron travels through the solid towards the surface. Electrons that travel through the solid can scatter for example with other electrons, impurities and phonons in the solid. This scattering process can be elastic or inelastic. In the first case, the electron's path is changed and the emission angle will be different. This effect leads to a broadening of the angular resolution in an ARPES experiment. However, elastic scattering conserves the energy and for an angle integrated spectrum like XPS or HAXPES these electrons are counted (as long as they reach the detector). Inelastically scattered electrons loose energy and therefore are detected at $E_{kin} - \Delta$, leading to an inelastic background of electrons. These electrons do not contribute to the spectrum and background treatments are available to subtract this.

The intensity $I(d)$ of elastically scattered electrons from depth d is given by

$$I(d) = I_0 \exp\left(-\frac{d}{\lambda}\right) \quad (2.25)$$

where I_0 is the intensity of all electrons without scattering and λ is the inelastic mean free path. The inelastic mean free path is a material and energy specific parameter. For XPS and UV experiments $5 \text{ \AA} < \lambda < 30 \text{ \AA}$. This limits the probing depth of these photons to the surface and only a few ML thick films. Especially, the first layer contributes the most as $I(0) = I_0$. Therefore, these experiments are very surface sensitive and cannot be used to probe bulk states of materials.

¹ The last term is caused by the transmission through the sample surface and is added here for completeness!

Transmission through the surface

The internal momentum \mathbf{k} of the electron in the solid and the external momentum of the electron after leaving the solid \mathbf{K} are differentiated in Equation 2.24 because on transmission through the surface of the crystal

$$\mathbf{K}_{\parallel} = \sqrt{\frac{2m}{\hbar^2} E_{kin,i} \sin(\phi)} \quad (2.26)$$

$$\mathbf{K}_{\perp} = \sqrt{\frac{2m}{\hbar^2} E_{kin,i} \cos^2(\theta) + V_0} \neq \mathbf{k}_{perp} \quad (2.27)$$

Where V_0 is the inner potential of the crystal from the free electron final state model. This is due to the translation symmetry breaking at the surface. The \mathbf{K}_{\perp} component has to overcome the inner potential, which describes the energy $V_0 = E_0 + \Phi$ needed from the highest valence electron state to the vacuum level (see Figure 2.8).

2.3.3. Spectral features

The approximations made to apply Fermi's golden rule have neglected every interaction of the particles in the solid. Of course this is a very crude assumption and a real photoemission spectrum contains other features. Some well known features relevant in the scope of this thesis will be described in the following.

Spin-orbit coupling

The photoemission process creates a core-hole in the solid. This core hole has a spin-moment $S = 1/2$ and the quantum number $L = 0, 1, 2, \dots$ of the excited electron. For a strong spin-orbit interaction this causes a doublet peak with total momentum $J_{\pm} = L \pm S = L \pm 1/2$ to emerge for $L > 0$ (p, d, f core-levels). The branching ratio is a measure for the relative abundance of initial states in peaks in a certain core-level from the ratio of the degeneracy of the two states. From quantum physics the degeneracy of an energy level is known to be $J(J + 1)$ therefore the branching ratio R is calculated as

$$R = \frac{J_+(J_+ + 1)}{J_-(J_- + 1)} = \frac{L + 1}{L}. \quad (2.28)$$

The branching ratio therefore describes the intensity relationship of a doublet peak and can be applied for XPS peaks and XAS edges.

Chemical Shifts

Different chemical states have a different electron configuration. For example EuO has a Eu^{2+} valence and $4f^7$ electron configuration on the Eu site, while Eu_2O_3 has a Eu^{3+} valence and $4f^8$ configuration. The core-level binding energies of these two different valencies of the Eu atom will be shifted by ΔE_B due to the fact that the core screening of the electrons is weakened. This can be modeled by [25]

$$\Delta E_B = K(Q_A - Q_B) + (V_A - V_B) \quad (2.29)$$

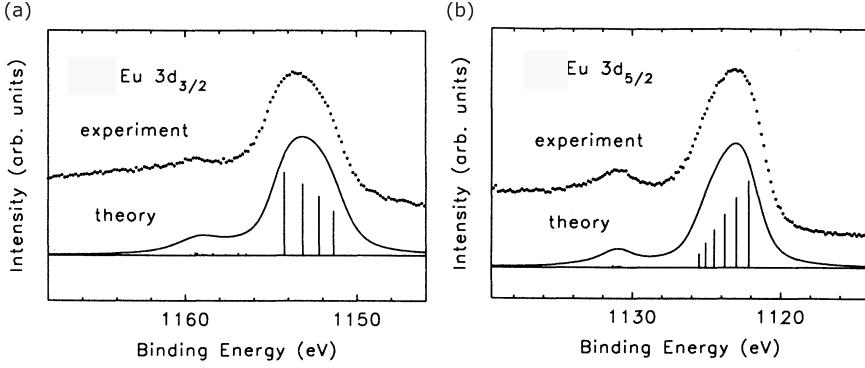


Figure 2.9.: Experimental data and theory for the photoelectron spectrum of (a) Eu $3d_{3/2}$ and (b) Eu $3d_{5/2}$ [26].

where K is an empirical constant describing the strength of weakening of the screening as described above, $Q_A - Q_B$ is the charge difference between the two chemical states A and B and $V_A - V_B$ the potential difference between state A and B constituted by the rest of the electron system.

In this way a chemical change of the material can be identified by changes in the electron binding energy and therefore a composition analysis is possible.

Final-state multiplet satellites

Photoelectron spectra often contain satellite lines. The satellite lines can be broadly categorized in lines due to multi energy X-ray excitation (non-monochromatic source) and satellite lines due to the electronic structure of the material.

In the case of Eu $3d$ spectra a satellite line is observed at the high binding energy site of the Eu $3d_{5/2}$ and Eu $3d_{3/2}$ peaks [26]. Figure 2.9 shows a measurement, a prediction for these core-levels and the final-state multiplet. The calculation is based on the $3d^{10}4f^7 \rightarrow 3d^9 4f^7 + \text{photoelectron}$ states. The ΔE_B for the satellite lines depends on the core-level and the asymmetric line shape of the satellites are the arguments that exclude the possibility of a shake up satellite.

Therefore, both, the main peak and the satellite constitute the spectrum for divalent Eu cations. In conjunction with the chemical shift described above, the peak fitting for divalent Eu becomes quite difficult, as the satellite is intermixed with the chemically shifted binding energy of trivalent Eu, as will be shown in Section 4.3.

Kinks

In ARPES spectra the quasiparticle spectral function is measured [27]

$$A(\mathbf{k}, \omega) \propto \frac{\Im \Sigma(\mathbf{k}, \omega)}{[\omega - \epsilon_{\mathbf{k}} - \Re \Sigma(\mathbf{k}, \omega)]^2 + \Im \Sigma(\mathbf{k}, \omega)} \quad (2.30)$$

where $\epsilon_{\mathbf{k}}$ is the energy of the state in the Hartree potential, $\Sigma(\mathbf{k}, \omega)$ is the quasiparticle self-energy reflecting the many-body interactions. As ARPES can measure the lifetime of a photohole and its energy, the equation can be evaluated. In this way electron-phonon scattering, which causes a change in the self energy, can be observed as a "kink" in the band structure near E_F .

2.3.4. Implications of hard X-ray photoelectron spectroscopy

Using hard X-rays instead of soft X-rays influences a number of properties. Three important consequences are summarized in this section, in order to give an overview, why HAXPES was a necessary tool in the scope of this thesis and what its limitations are.

Information depth

The information depth is limited by the inelastic mean free path (IMFP) λ , as was shown above. Tanuma et al. have predicted the scaling behavior of $\lambda(E_{kin})$ using a modified Bethe equation[28]

$$\lambda = E_{kin} E_p^{-2} \left(\beta \ln(k E_{kin}) - C/E_{kin} + D/E_{kin}^2 \right)^{-1} \quad (2.31)$$

where, λ is in \AA , E_p is the bulk plasmon energy and β, k, C, D are material specific parameters. In Figure 2.10 λ is compared for 41 elemental solids and a universal scaling behavior is observed. In the high energy range $E_{kin} > 100 \text{ eV}$ the authors find a scaling behavior of $\lambda \propto E_{kin}^0$.78.

The high kinetic energy of electrons excited by hard X-rays leads to a significant increase in the inelastic mean free path. A range of 15 \AA to 50 \AA is observable for $E_\gamma = 2000 \text{ eV}$ to 10 000 eV. This leads to a more bulk sensitive measurement and is one of the key advantages of HAXPES and also the reason why it was used in the scope of this thesis. The information depth (ID) is defined as the depth where 95% of all electrons are excited from. ID depends on λ as

$$ID \approx 3\lambda \leftrightarrow I_{tot}(d = 3\lambda)/I_0 \approx (1 - \exp(-3)) = 0.95 \quad (2.32)$$

Therefore, the information depth of HAXPES can be as high as $d = 15 \text{ nm}$ and thereby allow to probe buried interfaces such as capping/EuO/SrTiO₃ heterostructures, as is relevant for this thesis. In general this also allows HAXPES to measure real devices such as Li-ion batteries [29] and spin-filter tunneling junctions.

Photoionization crosssections

On the other hand, the photoionization crosssection σ , depends on E_{kin} . Unfortunately, as the energy increases σ decreases. In fact, the scaling is quite substantial [30]

$$\sigma(E_\gamma) = \begin{cases} E_{kin}^{-3.5} & s - \text{shell} \\ E_{kin}^{-4.5} & p, d, f - \text{shell} \end{cases} \quad (2.33)$$

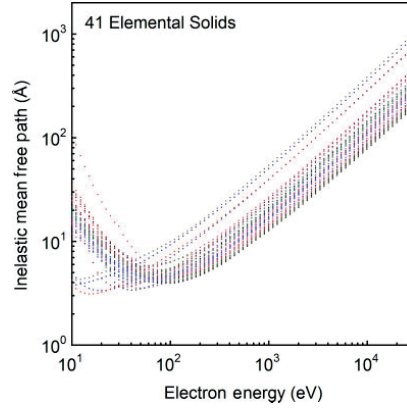


Figure 2.10: Inelastic mean free path as function of the electron escape energy. [28]

This implies, that HAXPES experiments can be performed well only at beamlines with high photon flux of 1×10^{11} Ph/s.

On the other hand, this effect can be used, to compare low and high photon energy experiments, of dissimilar materials having overlapping s and p, d, f core-levels. At going towards high E_γ the spectra will be dominated by s shell emissions and thereby a decomposition with regards to the s and non- s transitions is possible.

HARPES and its limitations

Due to the limited probing depth of UV photons, devices and their interfaces cannot be analyzed with regular ARPES. Consequently, it would be of advantage to utilize the higher probing depth of HAXPES and perform hard X-RAY ARPES, HARPES. Due to the availability of circularly polarized light it is also possible to study the magnetic properties at the same time.

However, the conservation of the angular information of photoemitted electrons depends largely on E_γ as phonon assisted transitions can become dominant, due to a low Debye-Waller factor $W(T, E_\gamma)$. The Debye-Waller factor is a measure for the phonon related smearing of the dispersive direct-transitions.

At high kinetic energies the processes of phonon creation and annihilation become a dominant part in the experiment [31]. These phonon processes scatter the electrons and therefore reduce the intensity of direct transitions. Only the direct transitions result in a clean electronic dispersion $E(\mathbf{k}_\parallel)$. As shown in Figure 2.11 at $T = 20$ K only few materials show a significant degree (i.e. $>50\%$) of direct transitions in the hard X-ray regime $E_\gamma > 2000$ eV. Due to this HARPES (hard X-ray angle-resolved photoelectron spectroscopy) is limited to materials with high $W(T, E_\gamma)$ (commonly high Z materials, like W or Pt). Adding Eu to this graph an estimation of suitable photon energies is possible. Due to its high Debye temperature $\theta_D = 350$ K [32] Eu has $W(T) > 0.5$ at $E_\gamma < 4290$ eV and is therefore a material where HARPES could be performed.

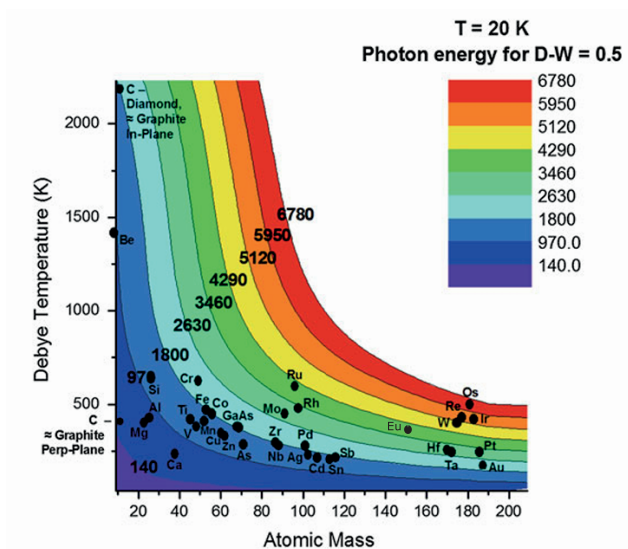


Figure 2.11.: Iso lines at selected photon-energies of the 50% Debye-Waller factors $W(T, E_\gamma)$ for various materials at $T = 20$ K [31]. Expectation for Eu added from calculated Debye Temperature [32].

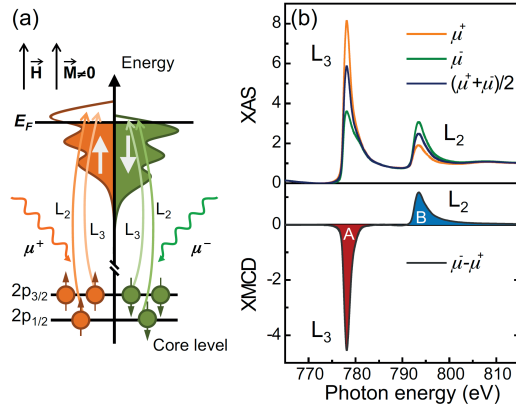


Figure 2.12: Schematic representation of the XMCD effect on a ferromagnetic material using the $L_{3,2}$ edge [33].

2.3.5. X-ray magnetic circular dichroism

X-ray magnetic circular dichroism is an effect that can be observed in (ferro-)magnetic samples. The X-ray absorption coefficient for left circular polarized light μ^- is different than for right circular polarized light μ^+ .

The cause for XMCD can be schematically described as depicted in Figure 2.12. XMCD originates from the electric dipole transitions, caused by the large spin-orbit coupling of all core-levels but the K edges [33]. This can be described in a simple two-step process. A $2p$ core state of a $3d$ metal is split in a $j = 3/2$ and $j = 1/2$ level (L_3 and L_2 edge respectively). In the first step the left (denoted as σ^-) polarization of the light (with respect to the orbital moment of the $2p$ orbital) results in excitation of a spin-up electron. In the second step, this spin-up electron needs to "find" an unoccupied place in the $3d$ valence band. For example in the case of the $3d$ ferromagnets like Co, there are less spin-up and more spin-down holes available. The right polarization of the light leads to the opposite behavior. Therefore, the XMCD spectrum

$$I_{XMCD}(E_\gamma) = I_{\sigma^-} - I_{\sigma^+} \quad (2.34)$$

will be negative at L_3 and positive at L_2 .

This behavior is also reflected by the transition probabilities W as defined by Fermi's golden rule in Equation 2.22, as the initial and final states ϕ_i and ϕ_f have different angular and magnetic quantum number $J_{i,f}$ and $m_{i,f}$. Due to the dipole selection rule these operators act upon the wave functions and cause the differences observed by 2.34. A detailed derivation can be found in [34].

The spectrum $I_{XMCD}(E_\gamma, H)$ depends on the applied magnetic field. It is symmetric under an exchange of the light helicity and an inversion of the magnetic field as $\sigma^- \rightarrow \sigma^+$ and $H \rightarrow -H$ leads to the same spectrum I_{XMCD} .

XMCD spectroscopy is very useful for the analysis of interface effects in magnetic heterostructures, as it is sensitive to the element specific magnetism and can disentangle

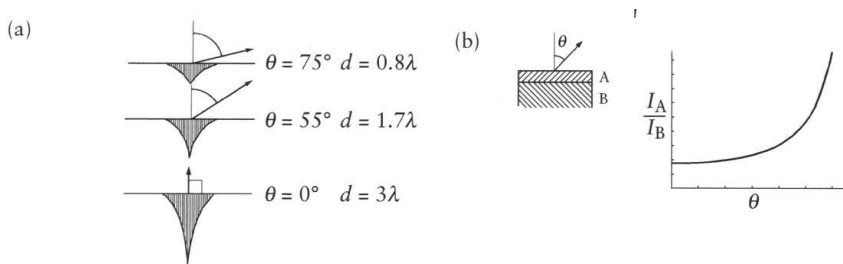


Figure 2.13.: (a) Sketch of the information depth as a function of the emission angle α in units of the inelastic mean free path. (b) Ratio R of over-layer intensity (I_A) and substrate intensity (I_B) as function of the emission angle α . [35]

the magnetic properties contrary to the volumetric magnetometry as in the case of VSM or SQUID (see Section 3.5).

2.3.6. Thickness determination by AR-XPS

In order to non-destructively determine the over layer thickness the integrated Beer-Lambert equation is used to model the substrate and over layer XPS peaks [35]. This is achieved by rotating the sample and thereby performing an angle-resolved XPS spectrum (AR-XPS, shown in Figure 2.13)². In this way, an expression for the intensity of the substrate I_A and the over layer I_B intensity is obtained

$$I_A = I_{A,\infty} [1 - \exp(-d/\lambda_{A,A} \cos(\alpha))], \quad I_B = I_{B,\infty} \exp(-d/\lambda_{B,A} \cos(\alpha)) \quad (2.35)$$

where $\lambda_{B,A}$ denotes the inelastic mean free path for electrons emitted from layer B in layer A and $I_{A,\infty}$ is the intensity of an infinitely thick layer of A . For our studies it suffices to assume $\lambda_{A,A} = \lambda_{B,A}$ as the kinetic energy is similar for both electrons from the substrate and the oxide over layer. Taking the ratio $R = \frac{I_A}{I_B}$ one obtains, after rearranging for d , the over layer thickness

$$d = \lambda_{A,A} \cos(\alpha) \ln [1 + R/R_\infty] \quad (2.36)$$

This equation holds for one angle and can be evaluated for the case of only one measurement, if and only if the layer is a discrete layer. Since this is hardly ever the case, the whole angle dependent XPS data needs to be recorded and a straight line fit can be applied to a plot of d versus $1/\cos(\alpha)$, which produces a straight line with the slope of $d/\lambda_{A,A}$. This technique is used to calculate the over-layer thickness as presented in Section 4.5.

² As there are core-level peaks studied here, the angle resolution causes different escape lengths in the overlayer and does not reflect the band structure dispersion, as would be the case for valence electrons in ARPES.

$\lambda_{A,A}$ can be calculated, as shown above in [Subsection 2.3.4](#). Another way to obtain $\lambda_{A,A}$ is to provide a sample series with known over layer thickness (from XRR for example) and use the AR-XPS technique to obtain not d but $\lambda_{A,A}$ from the $d/\lambda_{A,A}$ slope of [Equation 2.36](#).

CHAPTER 3

Experiment

In this section the experimental details of the oxide growth, laboratory-based characterization and advanced analysis using synchrotron radiation are presented. We utilize these three means to compile a comprehensive study of europium monoxide growth on oxidic substrates with precise knowledge of chemical composition and structure in order to create and understand novel interfacial electronic and magnetic properties.

In order to grow high quality oxide heterostructures every part of the preparation is crucial: The substrate selection determines the growth of the over layer. In this thesis we mostly use SrTiO₃ substrates. The effect of the crystal structure is only one parameter contributing to the growth. Moreover the substrate miscut, chemical treatment and annealing influence the resulting surface quality tremendously, which is shown in section 3.1. We prepare EuO and the substrates in an oxide molecular beam epitaxy (MBE) system that was put into practice in our research group and is described in Section 3.2. The experimental details of the *in situ* structure determination and chemical analysis by reflection high energy electron diffraction (RHEED), low energy electron diffraction (LEED) and *in situ* x-ray photoelectron spectroscopy (XPS) are described in section 3.4. This combination of employing both MBE and XPS *in situ* is an important prerequisite for successful synthesis of the metal stable ferromagnetic oxide. Furthermore the samples are analyzed *ex situ* with regard to their surface morphology by atomic force microscopy (AFM), their magnetic properties by volumetric magnetometry and crystal structure by X-ray diffraction (XRD) or X-ray reflection measurements (XRR) as described in section 3.5).

Finally, this work makes use of synchrotron radiation to assess the chemical composition, to perform element selective depth-profiling, to measure the valence band structure and to determine the element-selective magnetic properties of magnetic heterostructures. The synchrotron experiments are performed at four different facilities in Europe, as described in Subsection 3.6.1.

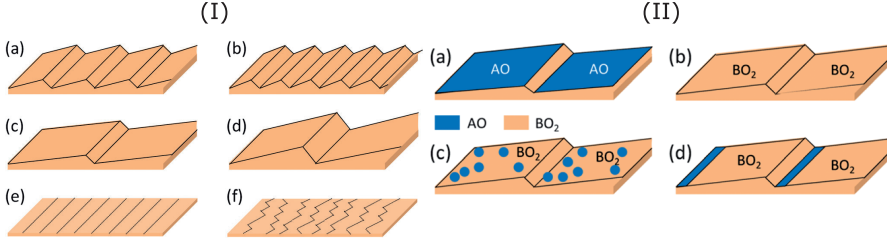


Figure 3.1.: Different surface morphologies (I) and surface terminations (II) of the perovskite (001) surface. In the case of SrTiO₃, the letters on the graph represent A = Sr and B = Ti. For the preparation of high quality oxides, the preparation aims at single-step height terraces (Ic) with straight edges (Ie) and a pure TiO₂ termination (IIb). [36]

3.1. Preparation of SrTiO₃ substrates

Most of the data in this thesis is obtained for magnetic heterostructures prepared on SrTiO₃ (001) substrates. In this section, we present the parameters crucially influencing the SrTiO₃ surface. The employed single crystals are purchased at CrysTec GmbH, Berlin.

SrTiO₃ is a layered crystal and has a cubic perovskite structure with a lattice parameter $a = 3.905 \text{ \AA}$ belonging to the primitive space group Pm3m. Due to its crystal structure, a (001) oriented single-crystal of SrTiO₃ is a stack of alternating SrO and TiO₂ layers. Due to this layered structure, the surface consists either of a SrO, TiO₂ termination or a mixture of both. The first two cases occur when cleaving a SrTiO₃ single crystal perfectly parallel to the (001) plane. This is technically impossible and therefore all substrates have a miscut $\alpha_{mis} > 0$. Due to this fact we perform a particular surface treatment in order to obtain a reproducible surface termination and regular terrace structure. Our aim is the *ex situ* preparation of SrTiO₃ with TiO₂ termination with regular step edges of unit cell height. The different morphologies and terminations of SrTiO₃ are shown in Figure 3.1.

Surface treatments for SrTiO₃

The different surface treatments can be categorized by their goals: either a certain surface morphology or surface termination is the desired result (see Figure 3.1). The surface morphology is mostly influenced by the crystal selection and annealing parameters, while the termination can be prepared by wet-chemical treatment and subsequent annealing.

Annealing of substrates leads to a crystalline reordering of the surface and can turn an atomically unordered surface into an ordered state. This effect can be accompanied by irregularities such as step-bunching. Step-bunching (see Figure 3.1, left (c)) occurs for substrates with a high miscut angle. Consequently, the selection of single crystals is restricted to a maximum $\alpha_{mis} < 0.1^\circ$. The in-plane miscut-angle α_{IP} is associated with a zigzag behavior of the step-edges and should be selected to be sufficiently small, i.e. $\alpha_{IP} < 0.1^\circ$. Finally, the annealing temperature plays a major role and is chosen to be

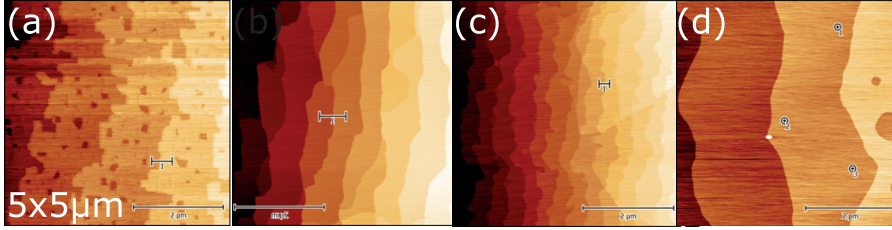


Figure 3.2.: Results of a SrTiO₃ (001) surface treatment study with (a) water-leaching, (b) hydrogen per-oxide bleaching, and (c) etching with acol regia or (d) buffered HF. Images were obtained after 2.5 h annealing at 950 °C in air. Optimal results are found for (d).

$T_A = 950\text{ }^\circ\text{C}$ [37]. At this temperature, the segregation of Nb-dopants and SrO to the surface is minimized, while the surface mobility is enhanced to enable the crystalline reordering effect [36].

Wet-chemical treatments for TiO₂ termination

A multitude of wet-chemical treatments for the TiO₂-terminated SrTiO₃ (001) surface can be found in the literature, ranging from water leaching (a), bleaching with H₂O₂ (b), to etching with acol regia (c) or buffered HF (d) [9, 38–40]. All four treatments report atomically flat SrTiO₃ surfaces with constant TiO₂-termination. In order to obtain optimal parameters for the preparation of the SrTiO₃ surface these methods are compared in the following.

After applying the four different approaches, AFM scans of the obtained surface are shown in Figure 3.2. All treatments lead to a highly ordered SrTiO₃ (001) surface. The water treatment leads, however, to an irregular pattern with a mixture of rectangular incorporations. Apparently, the step-edges have either not completely formed due to a too short annealing time or the water has reacted locally with the SrTiO₃ surface and left these incorporations as etch-pits. Bleaching in H₂O₂ and acol regia etching leads to the formation of double steps on the substrate, which is also not the desired result. Finally, the treatment with BHF for $t = 30\text{ s}$ leads to the formation of regular step edges of unit-cell height. The step width is on the order of $d_{step} \approx 1\text{ }\mu\text{m}$ and we find a miscut of $\alpha_{mis} = 0.02^\circ$. For further information see Table A.1.

Shown in Figure 3.2 (d) we observe circular structures on the SrTiO₃ surface. In order to evaluate their origin, the annealing is repeated, yet the situation is unchanged. We argue, that these are pinned areas belonging to the next lower terraces. These have not occurred in samples with $\alpha_{mis} > 0.05^\circ$ and therefore we decide to limit the lower end of the miscut angle to $0.05^\circ < \alpha_{mis} < 0.1^\circ$.

The etch time $t = 30\text{ s}$ has been chosen, as longer etch times lead to the formation of significant numbers of etch pits. At $t = 1\text{ min}$, we observe 5 large etch-pits with depths $d_{pit} > 3\text{ nm}$ and $A_{pit} > 30\text{ nm} \times 30\text{ nm}$ on a $5\text{ }\mu\text{m} \times 5\text{ }\mu\text{m}$ scan area. These etch-pits are detrimental in that they lead to shorts in a tunnel barrier structure connecting the conductive substrate and the top metal contact.

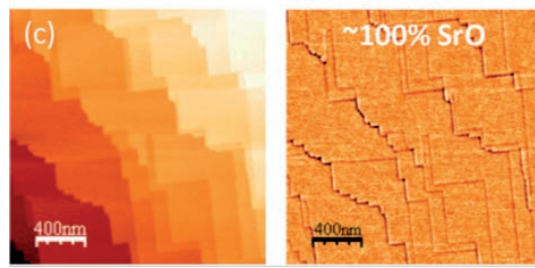


Figure 3.3.: SrO-terminated SrTiO₃ surfaces produced by annealing. Clearly the straight structure of the step edges has been changed to a rectangular pattern. In these crystals so called Ruddlesen-Popper phases (rectangular structure at the step edge) appear [41], we therefore prepare SrO terminated SrTiO₃ by depositing SrO on top of TiO₂ terminated SrTiO₃ substrates in the MBE system.

Preparation of SrO terminated SrTiO₃ (001)

The surface mobility of adatoms on SrO and ionic oxygen conductivity inside SrO crystals is different from that of TiO₂ terminated SrTiO₃ [23], which makes a study of oxide growth on SrO terminated surfaces interesting.

In literature, two different approaches are reported for the preparation of SrO terminated SrTiO₃. Either the substrates are annealed in air for 96 h at 950 °C [36] or (monolayer) thin films of SrO are deposited on TiO₂ terminated surfaces [4]. Figure 3.3 depicts the result of the elongated annealing procedure. So called Ruddlesen-Popper phases are created on the surface. Therefore, this route was not pursued further and we perform SrO deposition in the oxide MBE system to prepare SrO-terminated SrTiO₃ substrates from TiO₂-terminated SrTiO₃ [41].

3.2. Oxide MBE for the preparation of ferromagnetic oxides

A custom MBE and analysis ultra-high vacuum chamber built by SPECS company in Berlin is employed for the preparation of EuO oxide heterostructures. The simultaneous realization of an *in situ* XPS system, while allowing for oxide preparation in a MBE chamber is a rare combination and enables a rapid development of synthesis procedures. Special care was taken to account for the necessary high precision control of the oxygen partial pressure.

The MBE (see Figure 3.4) consists of four parts: load-lock, transfer, MBE and analysis chamber. The samples surface cleanliness is ensured by operating the system at ultra high vacuum (UHV) conditions.

The load-lock is equipped with a six slot sample garage and has a residual gas pressure of 3×10^{-8} mbar. The connecting transfer chamber also has a six-slot sample carousel and the base pressure in this chamber is kept at 1×10^{-10} mbar.

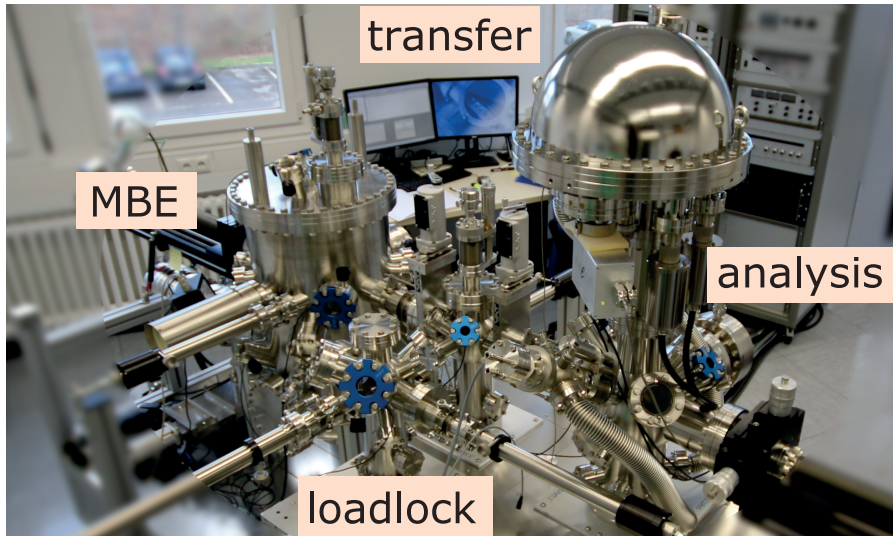


Figure 3.4.: The MBE system at the Oxide Spintronics Laboratory – a combination of all important prerequisites for EuO growth: ultra-high vacuum base pressure, specialized oxygen delivery for reactive oxide-MBE growth, *in situ* XPS for direct chemical analysis of the grown films and surface structure determination with LEED and RHEED. Additionally, sample structuring using shadow masks is possible.

MBE chamber

The MBE manipulator can be used to heat and cool the sample. Heating is realized by electron bombardment applying voltages up to $U_e = 1000\text{ V}$ and emission currents up to $I_e = 50\text{ mA}$. With this sample temperatures of $T_S = 250\text{ }^\circ\text{C}$ to $1200\text{ }^\circ\text{C}$ can be achieved, which we use for *in-vacuo* annealing and can also be used for Si flashing. The manipulator can be cooled with by supplying liquid nitrogen to the manipulator head.

The sample temperature is monitored by a Type K thermocouple soldered to the sample plate holder. However, this method leads to large deviations between the real and the measured temperature on the order of $\Delta T \approx 200\text{ K}$. This is not practical for the deposition of high quality oxide films. In order to improve the resolution of the sample temperature measurement an external pyrometer was installed and calibrated (see Figure 3.5).

Sample temperature measurement: Pyrometer calibration

A pyrometer can offer a rather precise measurement of the sample surface temperature, especially in the case of non-transparent samples, such as 0.5% Nb doped SrTiO_3 . For this, only the emissivity ϵ has to be known, which is $\epsilon = 0.35$ for 0.5% Nb doped SrTiO_3 [42, p. 28].

However, due to the non-zero absorption of the windows (see Figure 3.5 (a)) and

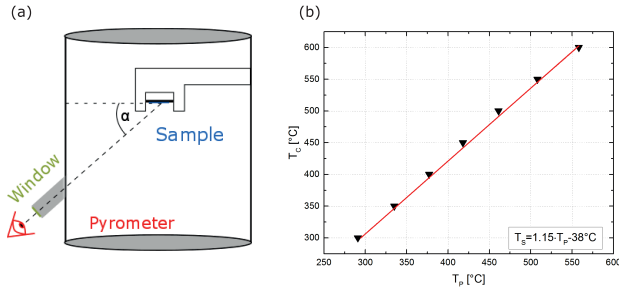


Figure 3.5.: (a) Sketch of the Pyrometer mounted on the MBE chamber. (b) Results of the pyrometer calibration using Nb doped SrTiO₃ and the emissivity $\epsilon = 0.35$. The sample temperature calibration leads to a resolution of $\Delta T = \pm 3.69^\circ\text{C}$.

the misorientation of the pyrometer axis with respect to the sample surface, additional calibration is necessary.

In this regard, we temporarily install a Type K thermocouple vacuum feed through on the MBE. The thermocouple is clamped down onto the sample surface and we perform the calibration using a constant emission voltage $U_e = 500\text{ V}$. We vary I_e so that the surface temperature of the thermocouple T is scanned in 50°C increments in the range 250°C and 600°C . A measurement point is taken when both T and the pyrometer temperature, T_P , are stable.

The results are depicted in Figure 3.5 (b). The measured temperatures exhibit linear behavior and an accurate calibration in the chosen temperature range is possible. The fit result has a accuracy of $\Delta T = \pm 3.69^\circ\text{C}$ and the error on the slope is $\Delta m < \pm 0.01$. With this calibration we regard the accuracy of the sample temperature measurement to be sufficiently high for our application.

Specialized oxygen inlet

The stoichiometry of europium oxide depends sensitively on the oxygen partial pressure supplied during growth (see Subsection 2.1.1). Therefore, the control of the oxygen gas inlet is a crucial part of the synthesis. Two key components were considered for the construction of the chamber with regard to the oxygen delivery: First, a quadrupole mass spectrometer (QMS) is mounted inside the MBE to monitor the O₂ partial pressure in real time. Second, a oxygen pipe is designed so that the oxygen impinges directly onto the sample surface. This circumvents the need to flood the MBE chamber with oxygen and enhances the local oxygen pressure by a factor of about 100 compared to the base pressure in the MBE. We checked this feature using a simulation and found that for our configuration the variation of the oxygen flux is expected to be $< 5\%$ for a $10\text{ mm} \times 10\text{ mm}$ sample (adapted from [43]).

The measurement of the oxygen partial pressure present directly at the sample surface is not possible. Instead, the oxygen feed is branched into two lines of equal length: One gas line supplies the oxygen to the sample surface, while the other is directed at

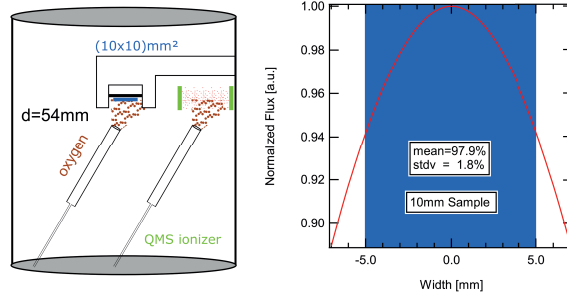


Figure 3.6.: (a) Sketch of the MBE and the branched oxygen inlet pointing at the QMS and the sample. (b) results of a simulation of the oxygen flux as a function of the displacement from the middle. The variation of the O flux is 5% on the scale of a $10\text{mm} \times 10\text{mm}$ sample. Simulation adapted from [43].

the quadrupole mass spectrometer. Keeping the distances equal, comparable oxygen pressures (and thereby the oxygen fluxes) are produced at the sample surface and the mass spectrometer.

The QMS measures a current which is converted to a pressure reading. A careful calibration is needed to measure absolute pressures with a QMS (commonly done with calibrated gas mixtures). In this thesis, we use a calibration method that relies only on the reproducibility of the pressure measurement and not on the absolute value of the pressure measurement (see Section 4.2).

MBE Evaporators

The MBE chamber is equipped with 6 evaporators, A five crucible electron gun (e-gun) and a low temperature Knudsen-cell (K-cell). The evaporators can be operated at the same time and are both equipped with a quartz microbalance with a SQM160 controller.

The five crucibles of the e-gun are filled - depending on the project - either with Pt, Cu, Au, MgO, Sr, Al. We calibrate the quartzes geometrically under the assumption of isotropic evaporation. It holds, that for non-equal distances between source and quartz d_S , source and sample d_Q the detected rate has to be corrected using

$$r_S = \frac{d_S^2}{d_Q^2} r_Q, \quad (3.1)$$

where r_S denotes the rate at the sample location and r_Q the rate of the quartz. The calibration of the quartzes is validated *ex situ* by X-Ray reflectometry (XRR) on a 20 nm thick Cu film on SrTiO_3 and is found to be precise within 5%.

The K-cell is filled with 99.9% pure Eu metal bought from MaTeck company (Jülich). Due to the successful validation of the geometric quartz calibration for the e-gun quartz, we apply the same calibration for the K-cell evaporator.

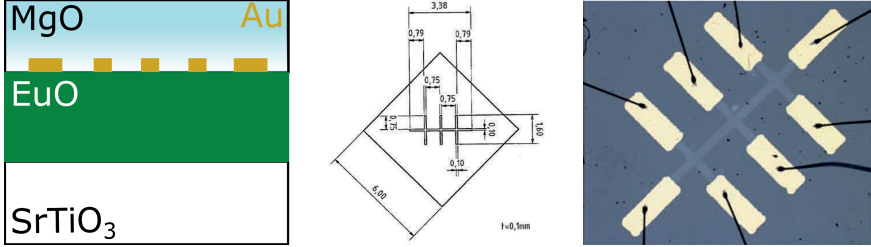


Figure 3.7.: Left: Schematic side-view of a EuO based oxide tunnel barrier. Middle: Drawing of a shadow-mask for *in situ* deposition of a Hall-Bar for transport measurements on a EuO/SrTiO₃ heterostructure and its interfacial two-dimensional electron gas. Right: Optical microscope image of a prepared sample including gold contacts and Al wire bonds. Adapted from [46].

3.3. Patterning EuO based transport structures

As ferromagnetic insulators are materials interesting for spin-dependent transport experiments, the MBE chamber is designed so that a shadow mask can be placed in close proximity to the sample surface and also changed *in situ*. Thereby, a patterning of the film during preparation is possible and in this way electrical measurements can be performed afterwards.

Several publications have proposed transport structures to utilize the spin filter tunnel barrier effect inherent in ferromagnetic insulators below their Curie temperature [3, 11, 44, 45]. The experimental challenge in this regard is the preparation of such structures under vacuum conditions to circumvent the problem of interface over-oxidation of the EuO film.

The oxide MBE chamber is designed to hold six shadow masks simultaneously, which can be brought in close proximity to the sample and allow for structures of $w = 100 \mu\text{m}$. The original design of the mask holder has a distance of approximately 5 mm between sample surface and mask. We construct a tripod holder that reduces the distance of the shadow mask to the sample to below 1 mm. The mask itself is made of a thin foil of a titanium-zirconium-molybdenum alloy cut out with a laser. The structure size is limited by the laser spot size to $d_{\text{Laser}} \approx 100 \mu\text{m}$. Figure 3.7 shows a sample drawing of the shadow-mask for a Hall-Bar structure and a optical microscope image of a finished Hall-Bar structure bonded and equipped with gold contacts. [46]

3.4. *In situ* characterization techniques

The characterization of surface properties for the synthesized films is only possible *in situ* as EuO is a metastable oxide and would degrade quickly under ambient conditions. The MBE is equipped with three surface sensitive probes: X-ray photoelectron spectroscopy (XPS), reflection high energy electron diffraction (RHEED) and low energy electron

diffraction (LEED). Hereby the chemical composition of the film and the substrate can be analyzed, while RHEED and LEED enable structure determination.

3.4.1. X-ray photoelectron spectroscopy (XPS)

Owing to the large oxygen reactivity of Eu metal, the chemistry of the grown film is the first criterion by which a successful growth should be evaluated. X-ray photoelectron spectroscopy enables a chemical analysis of the grown film and a depth profiling as shown in Section 2.3. For this, the valence state of the Eu atom is probed and associated with the three Eu oxidation states ($\text{Eu} \rightarrow \text{Eu}^0$, $\text{EuO} \rightarrow \text{Eu}^{2+}$, $\text{Eu}_2\text{O}_3 \rightarrow \text{Eu}^{3+}$). The MBE is equipped with a SPECS X-ray gun with anodes made from Al and Mg. The anodes produce X-rays with photon energies of 1486.27 eV and 1253.6 eV respectively [48, p 86]. The combination of both anodes allows the identification of Auger lines in the photoelectron spectrum. The X-rays are filtered by a Al foil to reduce the Bremsstrahlung.

The core-levels of interest are shown in Table 3.1. The Eu $3d$ core-level is most often studied, as it allows a chemical analysis of the grown film. We use the Al anode for the study of this core-level only. The kinetic energy of the electrons is very low when the Mg anode is used (≈ 100 eV). At these low kinetic energies a strong background from inelastically scattered electrons and the Bremsberg are present in the spectra and make the chemical analysis impossible. Instead, the Mg anode is regularly used to identify Auger peaks.

The hemispherical analyzer (PHOIBOS 100) and the X-ray gun are mounted at an angle of 20° to enhance the X-ray yield in the sample and bring the nose of the X-ray gun closest to the sample. The detector of the hemispherical analyzer is a 5 zone electron multiplier detector (EMD) and is routinely operated with a pass energy of $E_P = 30$ eV, yielding an instrumental resolution of [49, p 58]

$$E_A \approx \frac{E_p[\text{eV}] \cdot w[\text{mm}]}{R_0[\text{mm}]} \approx 100 \text{ meV} \quad (3.2)$$

where E_A is the energy resolution of the analyzer and $R_0 = 100$ mm the mean radius of the hemisphere.

The spectral width of the non monochromatized X-ray beam is $\Delta E_\gamma \approx 800$ meV

Atom	Core-level	Binding Energy [eV]
Eu	$4d$	128
Eu	$3d$	1155
Sr	$3p$	133
Ti	$2p$	458
O	$1s$	528

Table 3.1.: Binding energies of core-levels for EuO recorded for chemical analysis of heterostructures on SrTiO_3 [47].

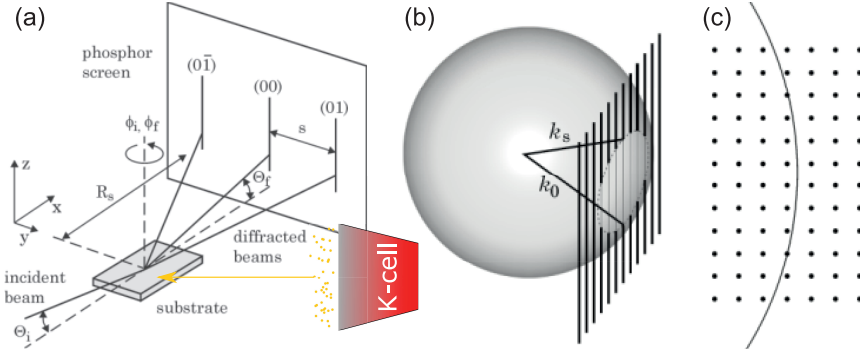


Figure 3.8.: Schematic sketch of a RHEED setup (a) and the Ewald construction (b) for a three dimensional case and (c) a two-dimensional case. The case shown in (c) is observed for flat specimen, while island growth leads to a transmission through the island and (b) is the correct description of the RHEED pattern. Adapted from [50].

therefore this is the resolution limiting factor.

The electrons are accelerated onto the detector with a voltage of $U_{\text{det}} \approx 2500 \text{ V}$. The voltage is responsible for the detection efficiency of the system and is regularly calibrated to ensure consistent intensities.

3.4.2. Reflection high energy electron diffraction (RHEED)

With reflection high energy electron diffraction (RHEED) one can determine the surface structure of samples prepared in ultra high vacuum (UHV). The RHEED technique uses high energy ($E_{\text{kin}} = 20 \text{ keV}$) electrons from an electron gun (e-gun) that impinge on the surface under low incident angle $\alpha_i = 1^\circ - 5^\circ$. The electrons scatter with atoms from the surface and are reflected onto a phosphorus screen, which in turn is observed recorded with a camera.

The reflected electron beam follows the relation

$$\mathbf{k}_S - \mathbf{k}_0 = \mathbf{G} \quad (3.3)$$

with the final and initial impulses \mathbf{k}_s and \mathbf{k}_0 , differing by a reciprocal lattice vector \mathbf{G} . This can be represented for the case of elastic scattering with the Ewald sphere, depicted in Figure 3.8. Scattering occurs for all \mathbf{k}_s that connect the origin of \mathbf{k}_0 and a reciprocal lattice rod. The wavelength of the electrons $\lambda = 0.09 \text{ \AA}$ is much smaller than the unit cell of a typical crystal a_{SrTiO_3} , which causes $\mathbf{k}_0 \gg \mathbf{G}$. Due to the small incidence angle only a small number of sharp reflexes on the so called Laue circle are allowed. In order to address other areas of the reciprocal space the sample should be rotated about its c -axis. As the manipulator does not allow for a rotation in this direction, samples are

mounted in the directions of the expected film (10) direction (the (hk) notation denotes reflexes in the 2D reciprocal space), for example at $45^\circ \parallel (11)$ direction of the SrTiO_3 substrate.

An image of the RHEED screen of a perfect surface shows the sharp diffraction spots on the Laue circle. Imperfect surfaces lead to a broadening of the spots and so called RHEED streaks. RHEED streaks are due to a finite mosaicity of the grown film. A second variation to a RHEED pattern is the observation of all reciprocal space points of the crystal. This indicates an island growth mode as the electrons are transmitted through the island. In this way RHEED reflexes of the whole reciprocal space are visible on the screen instead of being restricted to the a Laue circle.

The lattice parameter of cubic crystals can be obtained by applying Bragg's law

$$n\lambda = 2d \sin(\theta) \quad (3.4)$$

where n is a positive integer denoting the index of the reflex, $d = a$ is the cubic lattice parameter and θ is the angle between two reflexes.

The given equations are based upon a kinematic description of the scattering on the surface. However, RHEED is a technique where strong interactions, like multiple scattering, take place. Therefore, a dynamical treatment of the RHEED technique needs to be applied. In this regard, Kikuchi lines have been identified. They are caused by diffuse scattered electrons and appear as curved lines on the phosphor screen. Clear and sharp Kikuchi lines are an indication of flat and crystalline surfaces.

Due to the reflection geometry, the RHEED technique can be used during growth [50]. However, RHEED cannot be performed during the growth of EuO , due to the fact, that the high kinetic energies of the electrons react with the supplied oxygen and cause over oxidation of the film.

3.4.3. Low energy electron diffraction (LEED)

Low energy electron diffraction can determine the surface structure of crystals. Figure 3.9 shows a schematic sketch of a LEED system. Here, the electron energies are between 20 eV to 200 eV and therefore the penetration depth of these electrons is already in the range of only a few atomic layers even for the normal incidence electron beam. The wavelength of these electrons is on the order of 2.74 \AA to 1.15 \AA , comparable to the lattice parameter of the crystal. Applying again the Ewald construction for the 2-dimensional case one obtains conditions for the reflected beams. The LEED pattern as seen from the camera is an image of the reciprocal net of the crystal surface itself [51].

During the growth of an over layer the structure of the underlying substrate may be imprinted into the growing crystal, which is called epitaxy. If however, the surfaces has a different periodicity or orientation the net of the bulk crystal is used to describe the surface structure. These different morphologies of the surface are called reconstructions and can be as simple as having a doubled periodicity. In that case they are called $p(2 \times 2)$ for cubic system and the reciprocal lattice points of the surface reconstruction are $(0.5, 0.5)$ [51]. The surface reconstruction of the grown oxides can indicate intermixing into the substrate and the surface reconstruction of metal films such as Pt is still under

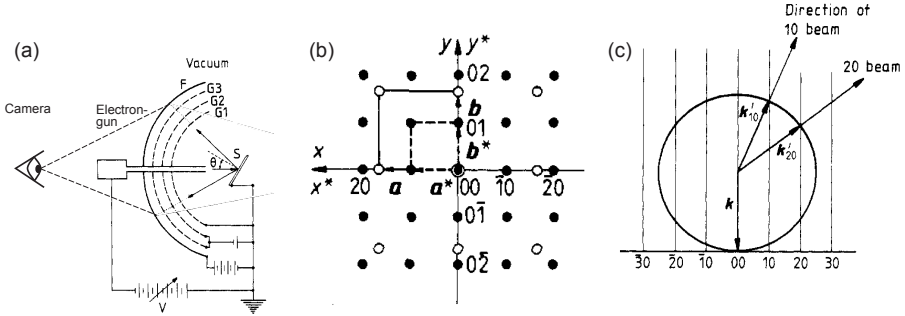


Figure 3.9.: Sketch of (a) a LEED setup and (b) the direct (open circles) and reciprocal lattice (full circles) of a square-symmetric crystal and (c) the two-dimensional Ewald construction of a normal incidence electron beam and the (10) and (20) back-scattered reflex. [51].

debate and has recently been analyzed with SPA LEED, a refinement of the LEED technique [52]. In the scope of this thesis, growth of epitaxial bulk Pt on SrTiO_3 is studied in Section 5.3 and LEED images are routinely taken of the grown EuO film.

3.5. *Ex situ* characterization techniques

Before depositing the oxide film, the substrate surface morphology is measured using atomic force microscopy (AFM) to validate the success of the TiO_2 termination procedure. Since Europium oxide is a ferromagnetic insulator, we are interested in studying the magnetism of the grown specimen. The low ordering temperature of $T_C = 69\text{ K}$ restricts the ferromagnetic properties to the low temperature regime. The magnetic properties of EuO films are evaluated using volumetric magnetometers like the super quantum interference device "SQUID" and vibrating sample magnetometry "VSM". In order to analyze the magnetism element selectively, the reader is referred to the experimental details in Subsection 3.6.1. Finally, the structure of the films is an important parameter, which is investigated by X-ray diffraction (XRD). To obtain the in plane orientation of the grown film on the substrate and to observe the mosaicity, we perform reciprocal space mapping (RSM). The film thickness is measured by X-ray reflectivity (XRR).

3.5.1. Atomic force microscopy (AFM)

In this thesis an Asylum Research "Cypher" AFM is used with an Air holder and a tip of the type Arrow NCR [54]. The scan is performed on a square of $5\ \mu\text{m} \times 5\ \mu\text{m}$ at a repetition rate of 5 Hz with a free amplitude of $a_{\text{free}} = 1\text{ V}$. Detailed scans are performed on a square of $1\ \mu\text{m} \times 1\ \mu\text{m}$. The AFM is operated at high z-feedback loop gains, in order to optimize the sharpness of the image by reducing the reset time.

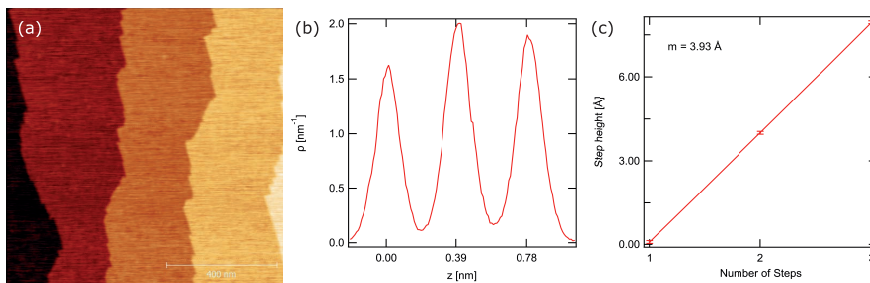


Figure 3.10.: Exemplary AFM data of a Nb:SrTiO₃ substrate: (a) median corrected and leveled image of Nb:SrTiO₃ surface after BHF treatment. (b) height distribution of the scanned 1 μm² area. (c) line fit to the peaks in the height distribution shows step height to be very close to the reported bulk values of $a_{\text{SrTiO}_3} = 3.901 \text{ \AA}$ [53].

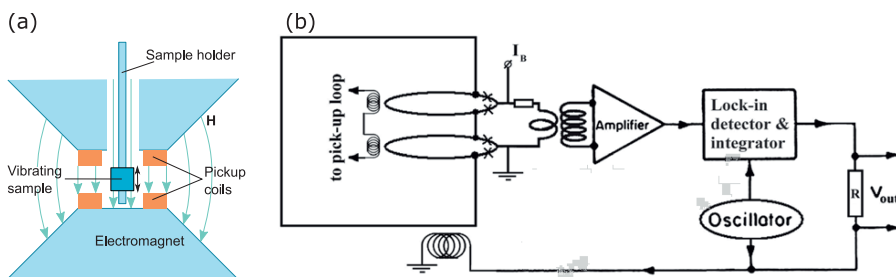


Figure 3.11.: Sketches of the VSM and SQUID apparatus. SQUID setup from [56].

The Gwyddion software is used to analyze the data [55]. To display the images a false color-scale of the type "Gwyddion.net" is used and adjusted to span the complete recorded z -range. The scan data is treated with median correction and either a 3-point level to the largest terrace or a median plane subtraction. Figure 3.10 illustrates the results demonstrated on a Nb:SrTiO₃ substrate after chemical etching and annealing.

3.5.2. Volumetric magnetometry

The magnetic properties of the heterostructures in this thesis are measured in four different ways. Two are based on photoelectron spectroscopy and are element selective. These synchrotron based techniques with limited access are described in Section 3.6, while we describe volumetric magnetometry in this section.

Magnetic measurements are performed using a vibrating sample magnetometer (VSM) and a superconducting quantum interference device (SQUID). Both apparatus are from Quantum Design, the Dynacool physical properties measurement system (PPMS) and the magnetic properties measurement system (MPMS). Both devices offer similar measurement capabilities and are in-house cross calibrated by a Pd and MnO standard based

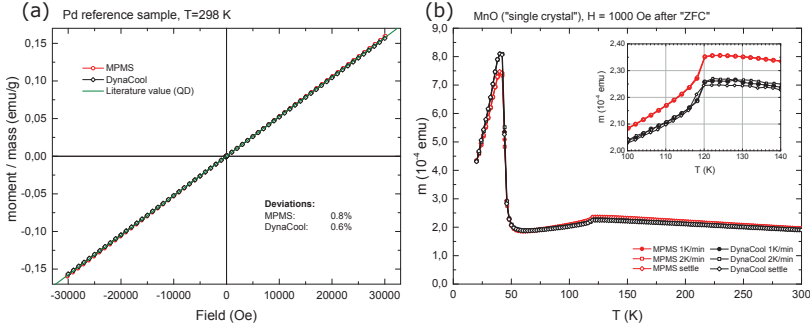


Figure 3.12.: Interchangeable magnetometers: The SQUID (Quantum Design MPMS) and VSM (Quantum Design Dynacool PPMS) magnetometer are two tools to measure the volumetric magnetization. They are calibrated against each other and we find that they comply within 1% of literature values. (a) $M(H)$ for a paramagnetic response of a Pd sample, (b) $M(T)$ showing the Néel transition of MnO. [57]

round robin test. The results (see Figure 3.12 show, that both devices report the magnetic moment and temperatures within very small errors and thereby are accepted to be used interchangeably. In the following, magnetometer measurements will be summarized as measurements from either of the two devices.

The principle of operation of the two devices (see sketch in Figure 3.11) is based upon a pickup coil for detection of the magnetic response of a small samples. Both devices use the point dipole approximation as analytical model to fit the shape of the acquired measurement data and obtain the moment in the pickup coil. The direction of the applied magnetic field is along the (100) axis of the sample. The pickup of the signal differs for the two devices.

Measurement principle of VSM and SQUID

In the VSM the sample is oscillated at a fixed frequency through the pickup coil and thereby induces a voltage proportional to the magnetic dipole strength. To lower the noise the signal is averaged over a period of 2 s at a vibration frequency of 40 Hz and a vibration amplitude of 2 mm. The temperature range available for this device is 1.8 K to 400 K.

In the SQUID a reciprocating sample offset measurement is performed, where the sample is repetitively moved with a low frequency of 1 Hz through the pickup loops. The detection in the SQUID is based on the voltage of a Josephson junction, a quantum interference device, where two superconducting half rings repel the added magnetic flux quanta due to the Meisner Ochsenfeld effect. A sample position vs voltage graph is recorded. The sample is moved through the pickup coil with a total displacement of 3 cm. The mounting procedure of the SQUID allows to mount the sample with either axis (100) and (001) parallel to the field and to the pickup coils to measure in-plane (IP) and out-of-plane (OOP) components of the magnetization.

The measurement routine on the MPMS features an automated sequence to detect

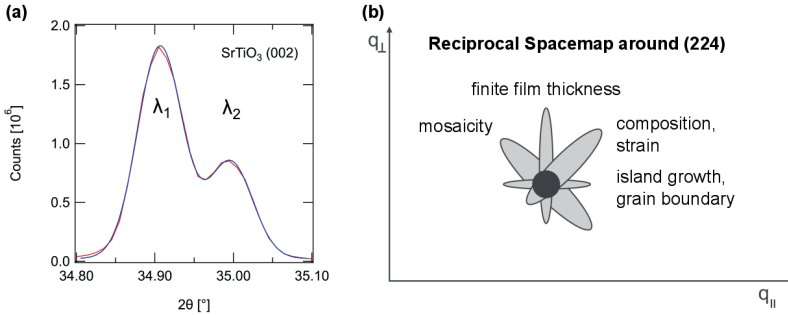


Figure 3.13.: (a) XRD detail scan of the SrTiO₃ (002) peak showing the angular offset and intensity relationship between the two different Cu K α lines. (b) schematic representation of a reciprocal space map of the (224) reflex from a zincblende structure. The various modifications of the peak shape and their origin are illustrated. ((b) modified from [59, p 480])

outlier measurements. The measurement is setup to complete three scans, which are averaged together before storage. This is repeated for another three times to find the average \bar{m} and calculate the standard deviation δm . This in turn is again repeated 3 times comparing the 3 averages \bar{m}_i and their standard deviations δm_i . Measurement are accepted if $\bar{m} - m < 2\delta m$ otherwise the measurement is discarded and remeasured. In this way, outliers are automatically detected and errors are reduced.

Resolution of the magnetometers

The VSM has a total resolution of about 3×10^{-7} emu and a noise level of 1×10^{-7} emu. The SQUID has a total resolution of about 5×10^{-8} emu and a noise level of 1×10^{-8} emu. By comparison a 2ML thin film of EuO on a $5 \text{ mm} \times 5 \text{ mm}$ substrate will yield a magnetization of $50 \mu\text{emu}$ – at least one order of magnitude above the combined detection limit of both magnetometers.

Magnetization as function of the magnetic field is commonly acquired at ± 1500 Oe fields while the magnetization as a function of the temperature is measured between 5 K to 150 K at an aligning field of 500 Oe that ensures that bulk EuO films are saturated. The upper temperature limit is deliberately chosen to be much higher than the bulk Curie temperature of EuO, 69 K [19], because various effects can lead to an enhancement until $T_S \approx 130$ K [58]. This is the case for example for under-stoichiometric EuO_{1-x} films and is used to identify metal inclusions.

3.5.3. X-ray diffraction and reflection (XRD, XRR)

The structure of the grown heterostructure is analyzed with X-ray diffraction. X-ray reflection is used to obtain the thickness of the film.

X-rays impinging on the sample are diffracted according to Bragg's law

$$n\lambda = 2d_{hkl} \sin(\theta) \quad d_{hkl} = \sqrt{\frac{h}{a} + \frac{k}{a} + \frac{l}{a}} \quad (3.5)$$

where θ denotes the incidence angle, d_{hkl} is the the lattice spacing of the crystal planes with index (hkl) , a is the crystal lattice parameter of a cubic crystal and n is an integer number. Often the doubled incidence angle 2θ is presented.

The diffractometer and resolution

In the scope of this thesis a four-cycle diffractometer of type Phillips MRD Pro is used, which has a four circle goniometer in the Bragg-Brentano geometry. The X-ray anode is monochromatized and uses a Cu anode. Through the monochromator Cu K α_{1+2} radiation with wavelength of $\lambda_1 = 1.540\,059 \text{ \AA}$ and $\lambda_2 = 1.541\,070 \text{ \AA}$ is transmitted [60]. In the case of our experiment we find the intensity relationship between the two peaks as $I(\lambda_1) : I(\lambda_2) = 2.2 : 1$. The double peak structure is only resolvable for very sharp peaks like the substrate reflex SrTiO₃ (002) (See Figure 3.13 (a)). Here, the double peak shows a separation of 0.089° , while the FWHM of the peak is 0.04° . For the broader EuO (002) peaks the width of 0.33° will not resolve this double peak and therefore no further correction will be applied. This analysis is helpful to decide whether a specimen is a twinned crystal or a double peak is just caused by the excitation.

Out of plane XRD scan for cubic lattice parameter determination

To determine crystal lattice parameters for the square systems usually the out of plane reflexes suffice. They are located along the $(00l)$ directions and show the highest intensities. Due to the structure factor of the materials symmetries some reflexes are forbidden. For example in fcc materials only reflexes of either purely even or purely odd (hkl) are allowed. Therefore, it is expected to see only EuO (which is a fcc material) reflexes like e.g. (002), (004), (113). In the case of the primitive space group of SrTiO₃ all reflexes are allowed and therefore (001), (002) [...] are possible. [61]

Reciprocal space mapping

Growing two materials on top of each other a multitude of effects can occur. Above a certain thickness, the film will relax to its bulk lattice constant. It can form mosaics or build grain boundaries. Moreover, the limited thickness of the film can broaden the diffraction peak. In order to study these effects reciprocal space mapping of two close lying reflexes from the substrate and the film is performed. In RSM the 2θ axis (detector axis) and the ω axis (sample axis) are scanned simultaneously, measuring a 2D map of both angles. This map represents the momentum transfer of the diffracted X-rays perpendicular to the crystal surface q_\perp and q_\parallel parallel to the crystal surface [59, p 480]. Figure 3.13 (b) shows the effects that lead to a broadening of the the XRD peak in the reciprocal space map. The phase denoted as strain effect is pointing in the direction of the origin where $q_\perp = q_\parallel = 0$. Orthogonal to this is broadening caused by the mosaicity of the film. Film thickness effects are parallel to the q_\perp direction while island growth is indicated by components broadened in the direction of q_\parallel . The direction of the broadening related to mosaicity and composition changes depending on the peak

location in the $(q_{\perp}, q_{\parallel})$ space, therefore we indicate in our RSM always the direction of the origin.

X-ray reflectometry

The thickness of the grown film is an important parameter. As the experimental growth technique for EuO growth heavily relies on the fact, that non-oxidized Eu metal is re-evaporated from the sample surface the reading from the quartz micro balance is not directly related to the thickness of the film (see [chapter 4](#)). Hence the X-ray reflectometry (XRR) technique is employed, by using the same machine above with small incident angles in the range $2\theta \approx 0^{\circ} - 5^{\circ}$. The X-rays are reflected from the interfaces between layers, due to change in optical density. The reflected beams interfere with each other and produce a characteristic oscillation in the intensity. The angle difference between two interference maxima can be used to obtain the thickness and roughness from the films by applying a fit model using the Parrat algorithm [59, p 459].

3.6. Synchrotron-based photoelectron spectroscopy

Europium monoxide and SrTiO₃ feature a rich variety of individual and interface-induced magnetic and electronic properties. This can range from interfacial two-dimensional conductivity, due to a redox process between EuO and SrTiO₃, to the enhancement of the ordering temperature of EuO by the deposition on top of a Co layer. In order to measure these interface properties with X-ray techniques, synchrotron sources are needed, as tunable photon energies and switchable light polarization are not commonly available in lab sources. Furthermore, EuO is a challenging material to prepare due to its metastability and we perform chemical depth profiling to evaluate effects of the substrate supplied oxygen during growth.

We employ synchrotron radiation in threefold ways. First, experiments are performed PETRA III and BESSY II with hard X-rays to study the depth profile of the sample by utilizing the higher information depth of high kinetic energy electrons. Second, experiments at I10 of DIAMOND light source are performed to study the element selective circular magnetic dichroism (XMCD) for soft X-ray absorption spectroscopy (XAS). Hereby the element selective character of this magnetic probe is employed to elucidate the magnetism of EuO and its interface for example with Co. HAXPES can be used at PETRA III with circular dichroism HAX-MCD and allows the study of buried layers and their interface to EuO. Finally the CASSIOPEÉ beamline at synchrotron Soleil provides light from the UV range to soft X-rays to perform angle-resolved photoelectron spectroscopy (ARPES), which allows observations relating to the valence band electronic structure (band structure) of the material and angle-resolved soft X-ray photoelectron spectroscopy (ARXPS) to study the depth structure of interfacial oxides.

The hard X-ray experiments are introduced in the next section. In [Subsection 3.6.2](#) we describe the experiment performed at CASSIOPEÉ and finally in [Subsection 3.6.3](#) the X-ray absorption MCD experiments at Diamond are described.

3.6.1. Hard X-ray photoelectron spectroscopy

HAXPES at HiKE, KMC-1, BESSY II, Berlin

Hard X-ray photoelectron spectroscopy (HAXPES) is a technique where X-rays with photon energies of $E_\gamma = 2\text{ keV}$ to 10 keV are used to irradiate a sample and excite photoelectrons of high kinetic energy. In Europe currently only three beamlines exist, at which this technique is available: HiKE endstation at KMC-1 beamline at BESSY II, Berlin, P09 at PETRA III in Hamburg and GALAXIES at Synchrotron Soleil in Saint-Aubin, France. In the scope of this thesis experiments are performed at the first two mentioned beamlines. The implications of hard X-rays are summarized in [Subsection 2.3.4](#).

The HiKE endstation is located at the KMC-1 beamline at the 3rd generation synchrotron BESSY II. In the storage ring electrons with a kinetic energy of 1.7 GeV are stored with a top-up mode at a current of 300 mA . The beamline features a photon flux of $1 \times 10^{11}\text{ ph/s}$ at 4 keV photon energy from a dipole magnet insertion device. The monochromator of the beamline is a double-crystal monochromator (DCM) with Si(111), Si(311) and Si(422) crystals achieving a beamline resolution of 200 meV at 6 keV with the Si(422) crystal and 50 meV using Si(111) at the 3rd order reflection. In practice a trade off between photon energy and the connected properties penetration depth, photon flux, resolution and the photoelectron cross section has to be made. Using a Scienta R4000 hemispherical analyzer with a retarding voltage of up to 12 kV the photoelectrons are detected. The spectrometer is mounted in a normal emission geometry, while the beam impinges at grazing incidence. The energy limits for the beamline are $h\nu = 2 - 12\text{ keV}$.

Additionally, the endstation is equipped with a X-ray fluorescence spectrometer in back-scattering geometry to detect the partial fluorescence yield of the absorbed X-rays and thereby study the hard X-ray absorption of the sample. A sample current meter allows the measurement of the total electron yield for hard XAS. With the high photon energy supplied by the beamline it is possible to study the Eu L_3 edge at $h\nu = 6975\text{ eV}$ (see [Section 4.4](#)) [[62](#), [63](#)].

HAXPES at P09, PETRA III, Hamburg

The HAXPES endstation is located at PETRA III, DESY, Hamburg. PETRA III is a highly brilliant synchrotron source with a storage ring for 6 GeV electrons at a beam current of 100 mA . The beamline is specified for photons in the range of 2.7 keV to 15 keV . Much higher fluxes of up to $2 \times 10^{13}\text{ ph/s}$ at 8 keV can be achieved. This allows for much faster scans and compensates for the lower cross sections at the higher photon energies.

Upstream of the undulator the beamline has a DCM with two crystal pairs Si (111) and (311) and a channel cut secondary monochromator. The second monochromator is set to a fixed photon energy of 5945.56 eV . Due to this fixed energy, monochromator drift is virtually absent and the photon energy resolution is improved to $<100\text{ meV}$. The electrons are detected with a SPECS PHOIBOS 225 HV analyzer. In total the experimental resolution can be 100 meV . In practice a higher pass energy is used and the total width of a measured Au Fermi-edge results in 308 meV . Using the phase retarder the light is over 99% linearly polarized.

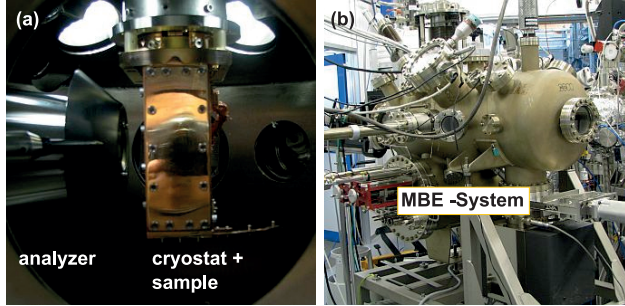


Figure 3.14.: Images of the CASSIOPEE endstation (a) high resolution ARPES chamber, view onto the LHe cryostat and (b) the MBE chamber, where magnetic 2DEG heterostructures were prepared for direct measurement of the valence band structure [68].

XMCD using hard X-rays

The beamline features a transmission diamond phase retarder, which can modify the polarization to left and right circularly polarized light [64]. In this way hard X-ray magnetic circular dichroism can be measured to assess the element selective magnetic properties of buried layers such as *ex situ* EuO films on SrTiO₃.

In order to magnetize the heterostructure, a magnet feed trough is mounted on a z drive and a permanent magnet with an approximate flux of 1 T can be brought into contact with the sample holder. The sample environment is in the UHV range of 1×10^{-9} mbar and can be cooled with a liquid He cryostat to $T < 30$ K. [65–67]

3.6.2. UV and soft X-ray angle-resolved photoelectron spectroscopy

In the following, the high resolution ARPES endstation and the MBE preparation chamber at CASSIOPEE beamline are described.

The beamline is located at the 3rd generation synchrotron SOLEIL with a electron energy of 2.75 GeV and a beam current of 300 mA. The X-rays and the UV light is produced by two different undulators built to span overlapping energy regions. The UV undulator produces photons in the energy range of $E_\gamma = 7.5$ eV to 120 eV, while the high energy undulator operates in the soft X-ray regime in the energy range 100 eV to 1250 eV. The high resolution is achieved using a monochromator consisting of a plane grating and a plane mirror with a resolution of 30 meV. The analyzer is a Scienta R4000 type analyzer. The sample manipulator has four axis of freedom and allows for motion in the x, y, z, and θ_z direction (θ makes rotation axis along the z direction). The sample can be cooled down to 5 K by a liquid He cryostat with a heat shield to completely surround the sample.

The MBE chamber is used for sample preparation. Here temperatures of up to 1000 °C

can be reached, monitored with a pyrometer. For deposition a low temperature Knudsen cell is available with quartz micro balance rate monitoring.

The wide photon energy range of the two undulators is used to not only study the electronic structure of the heterostructures, but also to study the oxidation state of Eu and SrTiO₃ as a function of the angle as described in [Subsection 2.3.6](#).

3.6.3. Soft X-ray absorption spectroscopy and magnetic dichroism

In order to identify which element is responsible for a measured volumetric magnetism it is necessary to utilize an element selective probe. Soft X-ray absorption magnetic circular dichroism (XMCD) is ideally suited in order to analyze magnetic heterostructures (see [Figure 3.15](#)). In this regard we perform XMCD XAS experiments at grazing incidence.

The Diamond Light Source in Didcot, UK is a 3rd generation synchrotron with an electron energy of 3 GeV and a beam current of 300 mA. The beamline I10 "BeamLine for Advanced Dichroism Experiments" (BLADE) is a soft X-ray beamline with an energy range of 0.4 keV to 2 keV. The beamline is equipped with two APPLE II undulators. The undulators utilize a shiftable magnet array, to produce circularly polarized light. A plane grating mirror monochromator is used to reduce the photon energy width down to 300 meV.

BLADE offers two endstations: we performed experiments at the high magnetic field X-ray absorption endstation (XAS). The near grazing incidence geometry $R = 80^\circ$ is chosen, as the thin films are expected to have a mostly in-plane easy axis of magnetization.

The sample environment can be cooled down to 3 K and magnetic fields of 14 T can be applied. The sample chamber is equipped with two X-ray fluorescence diodes in back-scattering geometry and a sample current measurement. Hereby, the fluorescence yield and the total electron yield can be measured simultaneously. Fluorescence yield measurements are sensitive to the bulk of the film (such as the interface region between two magnetically different films). This is due to the fact that the X-ray inelastic mean free path is on the order of several 100 μm . Total electron yield measurements are limited by the much shorter electron inelastic mean free path and due to this fact are a more surface sensitive measurement.

Hysteresis of the samples can be measured by automatically sweeping the field of the magnet and switching the helicity at each point from positive to negative helicity, ensuring two measurements at the same magnetic field and eliminating undulator backlash induced changes in the photon energy or time related effects.

In [Figure 3.15](#) we show exemplary data of DyFe₂/YFe₂. When the film is first analyzed with VSM a complex hysteresis loop is found. Due to the volumetric measurement of the VSM it is not possible to disentangle, which component contributes to which feature. Measuring the XMCD of the same film it can be shown, that the Dy- and Fe-XMCD signal clearly show the inter-layer coupling and thereby allow an understanding of the magnetic heterostructure.

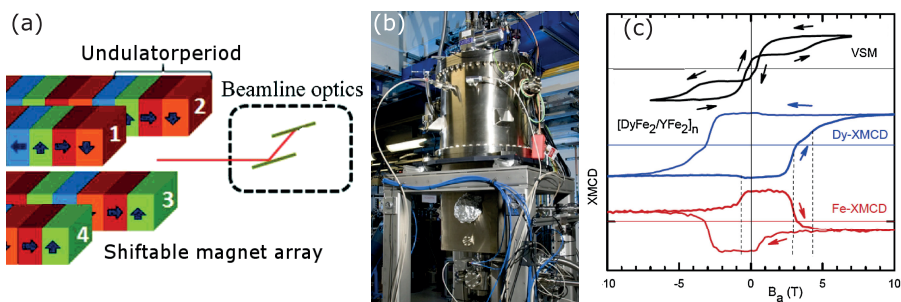


Figure 3.15.: Soft X-ray absorption magnetic circular dichroism (XMCD) measurements are performed at BLADE, Diamond Light Source. (a) Sketch of the APPLE II undulator at BLADE beamline, providing fully configurable polarization (left and right circular polarization). (b) Image of the 14 T high field measurement endstation where the XMCD measurements are performed. (c) Example of the strength of XMCD: element selective probe for magnetism. [33, 69]

CHAPTER 4

Oxygen-free growth of thin EuO films

In this chapter we discuss the synthesis of Europium oxides and their deposition on oxides such as transparent conductive indium tin oxide (ITO) or transition metal dichalcogenides like SrTiO_3 or BaTiO_3 . Since Eu is a highly reactive metal, the synthesis of europium monoxide poses considerable experimental challenges. We demonstrate a new route to prepare EuO films by utilizing the oxidic substrate as the supply of oxygen and controlling the latter by deposition parameters. First, we consider experimental techniques, evaluate the deposition of EuO using a new MBE system on an established substrate and develop a quantitative analysis method for Eu films by utilizing XPS. [Section 4.5](#) shows results from the deposition of EuO on ITO published in Gerber, T., Lömker P. et al., "Thermodynamic stability and control of oxygen reactivity at functional oxide interfaces: EuO on ITO" *J. Mater. Chem. C* 4, 1813–1820 (2016).

In [Section 4.6](#) and [Section 4.7](#) we develop a novel approach of redox EuO growth by utilizing SrTiO_3 substrate supplied oxygen. This technique is then extended to a range of other oxidic substrates to demonstrate the universality of this approach.

4.1. From europium to europium-oxide

The synthesis of EuO is performed using an oxide MBE system. Here, we supply Eu-metal with an e-gun and oxygen molecules with a specialized gas inlet (see [Figure 3.2](#)). Due to the fact, that Eu-metal can re-evaporate from a hot EuO surface (see [Subsection 2.1.1](#)) significant deviations of the sticking coefficient of Eu metal on the substrate are expected. This is due to the varying rate of Eu re-evaporation from an inert surface. However, in this thesis oxide substrates are used. The reactivity of the Eu atom initiates the formation of oxides from the substrate supplied oxygen. Depending on the temperature the thermodynamically preferred oxidation state may change and so does the available oxygen at the interface. Therefore, the properties of over-layers of oxides of europium

	$V_{uc} [\text{\AA}^3]$	f [f.u./u.c.]	ICSD
Eu	95.88	2	44720
EuO	135.96	4	53437

Table 4.1.: Unit cell volume V_{uc} and number of formula units per unit cell f for Eu and EuO.

are complex. In this section the different properties of Eu and its oxides are compiled and considerations for the growth rates are made.

For an analysis of the thermodynamics the reader is referred to [Section 4.5](#) and [Section 4.6](#).

Flux and growth rate

In an ideal case of EuO growth, equal amounts of Eu atoms and oxygen atoms are present in the film and the ratio between the fraction of Eu (O) atoms n_{Eu} (n_O) is

$$R = \frac{n_{Eu}}{n_O} = 1 \quad (4.1)$$

In the experiment we obtain $R = 1$, if $p_{O_2} = p_0$, the pressure of oxygen for deposition of stoichiometric EuO.

In the case of oxidic substrates, oxygen diffusion needs to be taken into account and we realize that

$$n_O = n_{O,substrate} + n_{O,supply}, \quad (4.2)$$

where the substrate and externally supplied oxygen atoms are considered.

The growth rate of the EuO film a_{EuO} can be calculated from j_{Eu} , the rate of impinging Eu atoms, at $R = 1$ and the crystal structure of EuO to yield

$$a_{EuO} = \frac{j_{Eu}}{f_{EuO}} \cdot \frac{V_{EuO}}{A_{sub}}, \quad (4.3)$$

where A_{sub} is the surface area of the substrate and f denotes the number of formula units of EuO per unit cell.

At the oxide MBE we measure the flux a_{Eu} with a quartz micro-balance. To determine a_{EuO} from the quartz reading, the crystal structure of Eu metal needs to be considered. The cell volumes and formula units per unit cell f for Eu and EuO are given in [Table 4.1](#).

Therefore, the growth rate of EuO is determined from the measured parameters as

$$a_{EuO} = \frac{V_{uc,Eu}}{V_{uc,EuO}} \frac{f_{Eu}}{f_{EuO}} a_{Eu} \approx 0.709 j_{Eu} \quad (4.4)$$

This relation holds as long as Eu atoms do not re-evaporate from the surface. An external determination of the true thickness (by XRR for example) will show, that

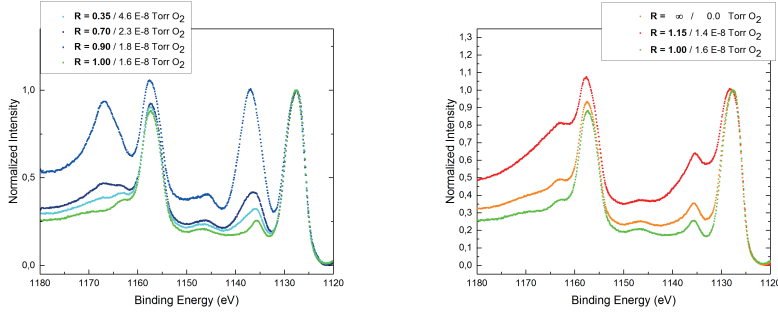


Figure 4.1.: XPS analysis of the influence of p_{O_2} for EuO films on YSZ at $j_{\text{Eu}} = 0.13 \frac{\text{\AA}}{\text{s}}$. Left: $p_{\text{O}_2} \geq p_0$, indicating over-oxidized mixtures of EuO and Eu_2O_3 . Right $p_{\text{O}_2} \leq p_0$ for metal rich EuO_{1-x} . During the measurement $\epsilon = 0.70$ and $T_S = 400^\circ\text{C}$. Measurement performed by Dr. Timm Gerber.

Compound	Valence	E_B [eV]	Reference
Eu	Eu^0	1125.0	[70]
EuO	Eu^{2+}	1124.9	[71]
Eu_2O_3	Eu^{3+}	1135.6	[71]

Table 4.2.: Electron-binding energies of the three Eu valencies associated with Eu, EuO and Eu_2O_3 in the 3d core-level.

$j_{\text{EuO,real}} < j_{\text{EuO}}$, when compared to the expectation we have found for the ideal flux-matched case. Hereby it is possible to quantify the re-evaporation of Eu metal from the surface for cases where $R > 0$, i.e. the oxygen partial pressure is lower than p_0 .

As the reaction of Eu on an oxide substrate can lead to the formation of Eu, EuO, Eu_3O_4 and Eu_2O_3 a chemical analysis of the surface needs to be performed and will be described in the following section.

4.2. Stoichiometric growth of EuO on yttria-stabilized zirconia

The oxygen flux for the synthesis of stoichiometric EuO is a critical growth parameter. To obtain a pressure standard we employ a well studied substrate for a reference synthesis of EuO, namely yttria-stabilized zirconia (YSZ). *In situ* XPS analysis will be used to identify the chemical composition of the prepared films. Thereby an *in situ* determination of critical the growth p_{O_2} is possible and allows a rapid optimization. The XPS spectra recorded in this section will be used in Section 4.3 to provide a set of reference spectra

of the doublet core-level Eu $3d$ and a quantitative fit procedure will be developed for the determination of the chemical composition by XPS analysis.¹

The EuO preparation described in this section is performed at $T_S = 400^\circ\text{C}$, where we find that the re-evaporation of Eu-metal is *not* a dominant process. Contrary to the normally used adsorption-limited deposition of EuO, this leads to stoichiometric formation of EuO, only when the oxygen pressure $p_{\text{O}_2,0}$ is exactly matched to the flux of Eu atoms. Any slight deviation of the flux ratio between Eu and O leads to either metallization or over oxidation.

We use YSZ(001) substrates from Crystec GmbH Berlin. The samples are oriented with (001) out of the plane and (100) parallel to the cut axis, at the factory they are epi-polished. YSZ is a well-suited material for EuO growth, as it has a lattice parameter of $a_{\text{YSZ}} = 5.13 \text{ \AA}$ that matches perfectly with the lattice of EuO. We prepare samples exhibiting all three phases of EuO: stoichiometric, over-oxidized and metal-rich. These three phases can be separated by XPS by observation of the valencies of the Eu atom: Eu, Eu^{2+} and Eu^{3+} , corresponding to Eu metal, EuO and Eu_2O_3 respectively.

Samples are prepared by supplying a Eu flux rate of $r_{\text{Eu}} = 0.13 \frac{\text{Å}}{\text{s}}$ while the growth time is $t \geq 10 \text{ min}$ to produce a significantly thick film $d < 5 \text{ nm}$. The pyrometer is calibrated as mentioned in Section 3.2 for the YSZ substrate and $\epsilon = 0.7$. The oxygen partial pressure is varied between $p_{\text{O}_2} = 0.0 \text{ Torr}$ and $4.6 \times 10^{-8} \text{ Torr}$, corresponding to $0.35 < R < \infty$.

We find, that stoichiometric samples are obtained for $p_0 = 1.6 \times 10^{-8} \text{ Torr}$. In order to prepare over-oxidized samples, the oxygen partial pressure is varied in the range of $p_{\text{O}_2} = 1.6 \times 10^{-8} \text{ Torr}$ to $4.8 \times 10^{-8} \text{ Torr}$, while metallic samples are produced by reducing the $p_{\text{O}_2} < 1.6 \times 10^{-8} \text{ Torr}$.

Figure 4.1 shows the XPS spectra taken of these films on the Eu $3d$ with Al K α radiation. The spectra are presented without background correction and are all normalized to unity on the $\text{Eu}^{2+} 3d_{5/2}$. In figure 4.1 (a), the spectra of over-oxidized films are shown. The spectra show Eu^{2+} at the binding energy of 1125 eV and 1155 eV for the Eu $3d_{5/2}$ and the Eu $3d_{3/2}$ part of the doublet. Eu^{3+} peaks are detected at 1138 eV and 1168 eV. The Eu $3d$ core-level shows high binding-energy peaks at about 10% of the intensity and $\Delta E \approx 10 \text{ eV}$. These are associated with the interaction of the core-hole with the final state multiplet structure [26].

Due to the excitation with non-monochromatic X-rays, satellite lines occur and are detected at binding energies 9.8 eV lower than the peak and with 6.4% of the peak intensity. As the spin-orbit splitting between 3/2 and 5/2 amounts to 30 eV peaks from the X-ray satellite lines are easily identified.

As mentioned before, the spectrum with $p_{\text{O}_2} = 1.6 \times 10^{-8} \text{ Torr}$ shows the XPS fingerprint of stoichiometric EuO. The findings of XPS are supported by magnetic measurements, RHEED, LEED and XRD (not shown). The overall conclusion of all experiments so far is, that indeed stoichiometric EuO is grown. It is worth noting, that a stoichiometric EuO film shows a sharp final-state peak, as it can be easily mistaken with Eu^{3+} , which lies in the same region.

By increasing the O_2 pressure, as described in the previous paragraph, (indicated

¹ The measurements shown here were performed by Dr. Timm Gerber.

by blue lines in Figure 4.1) the spectrum is changed. First only a broadening of the satellite peak is observed. Increasing the pressure further the spectral weight of Eu^{3+} is clearly identified. For $p_{\text{O}_2} = 3 \cdot p_{\text{O}_2,0}$ the ratio between Eu^{2+} and Eu^{3+} is unity with a stoichiometry of $1 \text{EuO} + 1 \text{Eu}_2\text{O}_3$ which corresponds to the next higher oxide of Eu, Eu_3O_4 .

Figure 4.1 (b) shows the metallic Eu films. However, for Eu metal-rich films there is no new peak forming that indicates Eu metal. This is because the binding energy of Eu^0 and Eu^{2+} are virtually the same (see table 4.2). What is characteristic about the reduction of $\text{EuO} \rightarrow \text{Eu}$, is a significant change in the peak shape. Eu metal in the growing film will lead to a finite conductivity in the film and thereby induce a peak asymmetry, caused by the excitation into the conduction band. Hereby the final-state peak is shifted upwards.

We find that for stoichiometric EuO the $3d$ satellite peak has a intensity ratio of 1 : 3 in relation to the $3d_{5/2}$ peak. For increasing asymmetry, this ratio is reduced and can be used as a guide to identify Eu metal in the spectrum. The orange line in figure 4.1 (b) deviates by 15% from $R = 1$ and already shows a significant shift of the satellite and a reduction of the peak intensity ratio to 1 : 2. The magnetic measurement of these films yields a magnetization tail, which is also indicating a metal rich film and thereby confirms the XPS analysis (data not shown).

We have utilized YSZ substrates and XPS chemical analysis in this section to determine the XPS fingerprints of oxide MBE grown Eu, EuO and Eu_3O_4 films. The spectral shapes are checked additionally with magnetic analysis² of the films which confirms the XPS analysis rendering this a suitable reference set to determine the stoichiometry of Eu films.

4.3. XPS-based stoichiometry determination of Eu compounds

From the previous section we have learned, that there are distinct XPS core-level features that enable a chemical discrimination of Eu, EuO and Eu_2O_3 . In order to quantify the chemistry of any grown EuO film by XPS, a routine to fit Eu $3d$ spectra from the obtained components is put into practice.

We model the chemical composition by the spectral weight of an XPS spectrum, which is directly related to the relative abundance of the the three types of Eu oxides. The Eu $3d$ spectrum can be decomposed into

$$I(E) = k_{\text{Eu}} \cdot I(E)_{\text{Eu}} + k_{\text{EuO}} \cdot I(E)_{\text{EuO}} + k_{\text{Eu}_2\text{O}_3} \cdot I(E)_{\text{Eu}_2\text{O}_3} \quad (4.5)$$

where k is the weighting factor of the respective component.

We obtain the intensity functions of the three Eu fractions $I(E)_f$, where f represents

² The magnetic measurements are omitted for brevity.

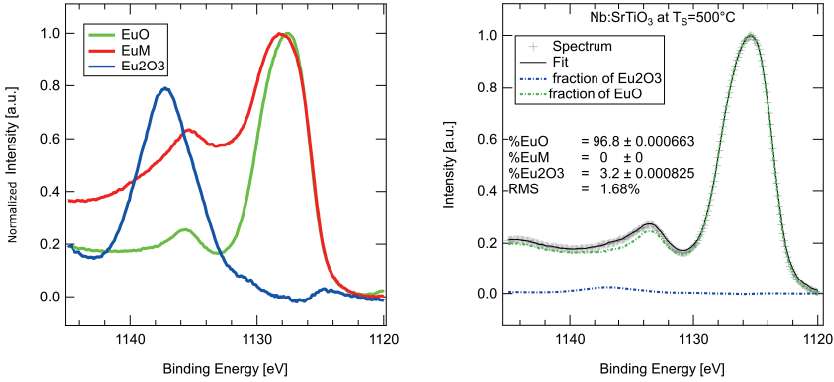


Figure 4.2.: Left: Reference intensity functions for the three Eu fractions: Eu, EuO, Eu_2O_3 . The difference spectra of the metallic and over-oxidized fractions lead to characteristic shapes that are used in a component model fit. Right: Component model fit on exemplary EuO data showing the stoichiometry of the grown film. A high degree of stoichiometric EuO no Eu metal and a small fraction of Eu_2O_3 is detected.

all three pure phases of Eu, EuO and Eu_2O_3 . We define the spectral functions as follows

$$I(E)_{\text{EuO}} = I(E, p_{\text{O}_2} = 1.6 \times 10^{-8} \text{ Torr}) \quad (4.6)$$

$$I(E)_{\text{Eu}} = I(E, p_{\text{O}_2} = 0 \text{ Torr}) \quad (4.7)$$

$$I(E)_{\text{Eu}_2\text{O}_3} = I(E, p_{\text{O}_2} = 4.8 \times 10^{-8} \text{ Torr}) - I(E)_{\text{EuO}} \quad (4.8)$$

Figure 4.2 shows the experimentally determined intensity functions of the data described in section 4.2. It is apparent, that the over-oxidized fractions shown in blue have a characteristic peak shape, as expected by the energetic separation of the Eu^{2+} and Eu^{3+} peaks. The red line indicates $I(E)_{\text{Eu}}$. It is evident, that the asymmetry in the peak of Eu compared to EuO allows a differentiation of the two spectral functions.

This decomposition model works well when the energy region of interest shows negligible additional inelastic background and other Auger and XPS are absent.

The model as described in Equation 4.5 is applied to XPS spectra of Eu films and yields the coefficients k_{Eu} , k_{EuO} , $k_{\text{Eu}_2\text{O}_3}$, which directly quantify the stoichiometry. In the right panel of Figure 4.2, the model is applied to a exemplarily data set of a film described in Section 4.6. It is shown, that the fit to the spectrum represents the data of EuO on SrTiO_3 well and shows that nearly stoichiometric EuO film is prepared. It shows the negligible amounts of Eu metal and a Eu_2O_3 content of 3.2%.

In this way, a method has been developed that allows the quantification of Eu $3d$ core-level data with regards to its chemical composition, despite the fact, that the core-level shift between Eu and EuO is not resolvable with XPS.

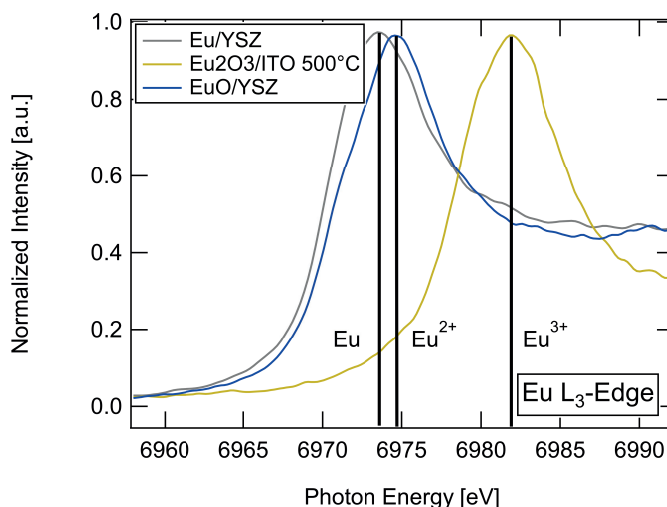


Figure 4.3.: Direct observation of peak energy shift for Eu, EuO and Eu_2O_3 . Using XAS at HiKE endstation at BESSY II a study of the Eu L_3 edge for three samples with the three different valencies of Eu shows, that a resolution of the resonance energy shift is possible using XAS, as the final states are relevant.

4.4. Determination of the Eu-metal content

The determination of the Eu metal content in Eu compounds difficult, because in XPS the binding energy of the electrons in Eu^0 and Eu^{2+} is very similar for the strong core-levels of the Eu atom (Eu $3d$) in the soft X-ray regime ($E_\gamma \leq E(A_{k,\alpha 1}) = 1480.6 \text{ eV}$). As a complementing technique X-ray absorption spectroscopy (XAS) has been performed at the HiKE endstation at BESSY II in Berlin. The L_3 edge of the Eu atoms was studied with 3 samples exhibiting all valencies of the Eu atom $\text{Eu}^{0,2+,3+}$.

The literature agrees, that a direct measurement of the stoichiometry of Eu compounds is difficult. Some models for EuO_{1-x} samples are based on the fact, that the rock salt structure exists only for $x < 4\%$. The models use the breakdown of this structure to discriminate samples below and above this doping concentration [72, 73]. Mauger and Godat state: "A chemical analysis of the EuO_{1-x} samples is of no help to determine the final composition because the O/Eu mass ratio is very small. In addition the variations of the lattice parameter as a function of x , in the range of composition where the material is homogeneous, are smaller than 10^{-3} , and thus negligible[.]. Therefore, the final composition must be estimated from the physical properties of the samples, such as Mössbauer spectra, electrical resistivity, infrared absorption spectra and optical constants." However, the aforementioned methods are all indirect, and require a careful modeling of the derived quantities as a function of the Eu metal content.

We study the L_3 edge of Eu and show the data in Figure 4.3. The spectra taken for

the three samples: Eu, EuO and Eu_2O_3 . The Eu edge is located at 6973.3 eV photon energy. The EuO edge however is shifted by 1.4 eV to 6974.7 eV and Eu_2O_3 is located another 6.9 eV towards higher photon energy. This separation is obviously well above the total instrumental resolution and allows a discrimination of Eu and its oxides. Thereby this route could be pursued in the future to obtain a direct chemical determination of EuO films. The quantitative method developed for the XPS Eu 3d core-level combined with XAS as a qualitative method for the determination of the absence of Eu-metal could be a sensible extension.

4.5. Limitations of the distillation condition: EuO/ITO

Functional metal oxides (MOs) are at the heart of such diverse research areas as nano-, spin- and optoelectronics as well as catalysis, battery- and solid oxide fuel cell technology. An exciting prospect in the field of oxide spintronics is the combination of an insulating magnetic oxide with a conductive oxide electrode. Such a magnetic tunnel junction can be used to generate highly spin-polarized currents [45, 74]. In this work, we propose and study a prototype hetero-structure for such application, which is composed of a ferromagnetic insulator, europium monoxide (EuO), and a transparent conducting electrode, Sn-doped In_2O_3 (ITO) [75]. In addition to the 'spin filter' ability, the transparency of the substrate allows for *in operando* probing of the EuO's magneto-optical response [76].

High-quality MOs are typically synthesized by thoroughly controlled high-temperature metal-oxygen reactions [77]. Integrating MOs into multi-functional oxide hetero-structures requires a fundamental understanding of these chemical processes, in order to prepare stable oxide phases with atomically sharp interfaces. The careful control of elemental fluxes and temperature is particularly important for growing metastable ferromagnetic EuO with its very narrow parameter range for stoichiometric synthesis: If the ratio of europium metal and oxygen flux $J_{\text{Eu}}/J_{\text{O}}$ only slightly deviates from unity, either Eu metal-rich EuO_{1-x} or the over-oxidized, paramagnetic phases Eu_3O_4 and Eu_2O_3 are formed [14]. By applying an adsorption-controlled EuO growth mode, the so-called distillation method, the narrow parameter space can be expanded. This method implies a flux ratio $J_{\text{Eu}}/J_{\text{O}} > 1$ and an elevated growth temperature which is high enough to enable the re-evaporation of excess Eu metal [14, 78–82].

At elevated growth temperatures, however, chemical reactions between the functional EuO layer and the substrate may occur, thereby yielding undesired interface contaminants. On Si substrates, these processes can be suppressed by the careful choice of buffer layers e. g. SiO_x [83] or SrO [84], as well as by surface passivation e. g. through formation of EuSi [85]. Thermodynamic stability of EuO with the substrate or buffer layer is important because it signals the absence of a driving force for such reactions [86]. While an exhaustive knowledge of the thermodynamic stability of semiconductor-oxide [87] and metal-oxide [15, 88] interfaces is available in literature, fundamental insights into the thermochemistry of all-oxide hetero-structures are surprisingly sparse.

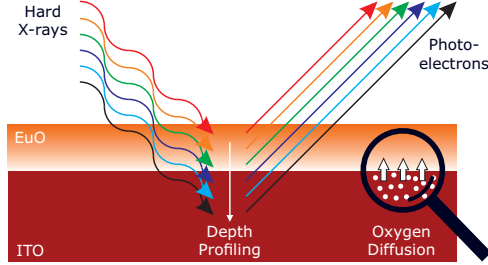


Figure 4.4.: Principle of a HAXPES depth profile: the escape depth of the photoelectrons depends strongly on the chosen excitation energy.

In this regard, we investigate the impact of the thermodynamic properties on the growth, interface chemistry and magnetic functionality of EuO on ITO virtual substrates. We employ hard X-ray photoelectron spectroscopy (HAXPES) as a powerful non-destructive and element-sensitive probing technique [89, 90]. HAXPES enables the chemical depth profiling of the functional oxide layer and the buried hetero-interfaces, as schematically depicted in Fig. 4.4. We show that thermally activated oxygen diffusion at the EuO/ITO interface limits the application of the otherwise beneficial EuO distillation method. Our study is corroborated by a comprehensive thermodynamic analysis of the EuO/ITO hetero-system. Applying these complementary methods yields a fundamental understanding of the origin of the oxygen reactivity at the EuO/ITO interface, and allows us to significantly optimize the stability of ferromagnetic EuO on ITO virtual substrates. In view of the significance to control oxygen reactivity at oxide interfaces, we derive guidelines for a suitable choice of substrates and buffer layer materials for all-oxide hetero-structures

Experimental

Virtual ITO substrates were prepared by depositing 50 nm thick ITO films via pulsed laser deposition (PLD) onto epi-polished (001)-oriented yttria-stabilized zirconia (YSZ, composition $\text{Zr}_{0.87}\text{Y}_{0.13}\text{O}_{1.935}$). ITO/YSZ(001) heteroepitaxy is achievable, because the YSZ lattice constant $a_{\text{YSZ}} = 5.142 \text{ \AA}$ almost equals half that of ITO ($a_{\text{ITO}} = 10.13 \text{ \AA}$), with a tensile lattice mismatch of $a_{\text{ITO}}/(2 \cdot a_{\text{YSZ}}) \approx +1.5\%$ [91]. PLD deposition of ITO was performed using a target with the composition $\text{In}_{1.8}\text{Sn}_{0.2}\text{O}_3$ (MaTeck GmbH, Jülich), a KrF excimer laser (wavelength 248 nm, 40 ns and 1 J per pulse) with an O_2 background pressure $p_{\text{O}_2} = 5 \times 10^{-3}$ mbar [92]. During ITO growth, the YSZ substrate temperature was set to $T_S \approx 300 \text{ }^\circ\text{C}$.

Thereafter, the ITO virtual substrates were transferred *ex situ* to an MBE system with a residual gas pressure $p < 10^{-10}$ mbar, where they were annealed in ultrahigh vacuum at $T_S = 550 \text{ }^\circ\text{C}$ for $t = 2 \text{ h}$ ³. For subsequent EuO growth, the substrate temperature was

³ We note that ITO is stable under these conditions (see Fig. 4.9).

set to either room temperature (RT) or 400 °C. Stoichiometric EuO was synthesized by e-beam evaporating 99.99% pure Eu with a deposition rate of 0.13 Å/s in an O₂ atmosphere. Using specialized gas inlets, the oxygen gas was equally distributed to the sample surface and to a quadrupole mass spectrometer (QMS) which was used to carefully control the partial O₂ pressure. We applied a flux ratio of $J_{\text{Eu}}/J_{\text{O}} = 1$ which in our setup corresponds to $p_{\text{O}_2} = 1.7 \times 10^{-9}$ mbar at the QMS. This value was determined by growing EuO on YSZ with varying O₂ pressure [71]. EuO growth was always initiated by exposing the sample to Eu metal flux. Subsequently, the O₂ flux was ramped to the desired value within approx. 30 seconds.

Structural analysis of the EuO/ITO samples was carried out *in situ* by reflection high energy electron diffraction (RHEED) and low-energy electron diffraction (LEED). Further *ex situ* structural analysis was carried out by X-ray diffraction (XRD) using an Philips X'Pert MRD four-circle diffractometer. Prior to all *ex situ* measurements the samples were capped with an Al layer ($d = 10$ nm) to prevent further oxidation of the metastable EuO films in air.

Magnetic characterization was carried out using a Quantum Design superconducting quantum interference device (SQUID) magnetometer. In-plane hysteresis loops were measured at $T = 5$ K and $M(T)$ curves were recorded warming up the sample in an alignment field of 100 Oe. The data was corrected for a paramagnetic background caused by the substrate and normalized to the nominal thickness of the EuO layer.

For chemical analysis and element-selective depth profiling, hard X-ray photoemission spectroscopy (HAXPES) experiments were conducted at the KMC-1 beamline at BESSY II (Berlin) with the HIKE endstation [63]. Si(111) and Si(311) double crystal monochromator were used to generate photon energies between 2010 eV and 5000 eV. The total energy resolution ranges from 320 meV to 500 meV and the information depth from ~ 10 nm to ~ 25 nm. The binding energy scale was calibrated by measuring the 4f level of an Au foil attached to the sample manipulator. Eu 3d and In 3d spectra were recorded at room temperature and in normal emission geometry. For quantitative analysis the spectra were corrected by Tougaard backgrounds to account for inelastic photoelectron scattering and fitted by convoluted Gaussian-Lorentzian peak shapes. The relative error of intensities estimated in this way is assumed to be 10%.

Three types of EuO/ITO samples are discussed in the following: Type (i): 4 nm EuO/ITO with the EuO layer grown at $T_S = 400$ °C, type (ii): 4 nm EuO/2 nm YSZ/ITO with the EuO layer grown at 400 °C, but with an additional PLD-grown 2 nm thick YSZ buffer layer, and type (iii): 4 nm EuO/ITO with the EuO layer grown at room temperature (RT).

Results and Discussion

ITO Virtual Substrates

First, we characterize the ITO/YSZ(001) virtual substrates utilized for subsequent EuO growth. Fig.4.5 (a) shows the XRD pattern of a 50 nm thick ITO film on YSZ (001). Only intense peaks of ITO (00 l) and YSZ (00 l) are observed, thereby confirming the epitaxial relation ITO(001)||YSZ(001). A rocking curve of the ITO (006) peak (data not

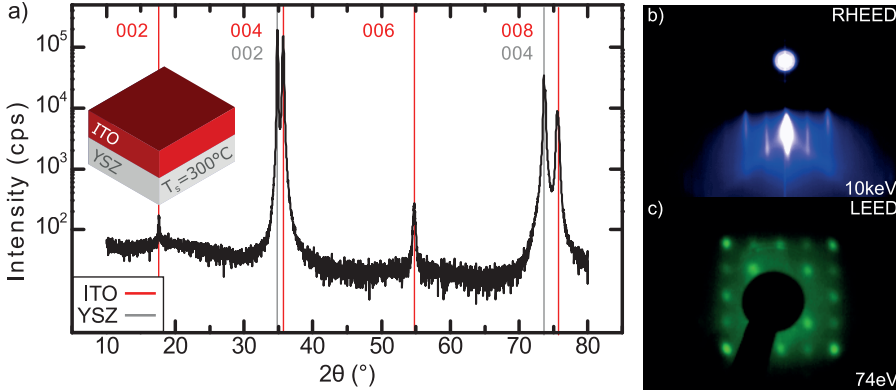


Figure 4.5.: Structural characterization of a 50 nm ITO film deposited on YSZ. (a): XRD scan with out-of-plane diffraction peaks of ITO (red) and YSZ (gray), (b): RHEED image taken with 10 keV at a substrate temperature $T_S = 400^\circ\text{C}$, (c): LEED image recorded with 74 eV at $T_S = 225^\circ\text{C}$.

shown) yields a full width at half maximum (FWHM) of only 0.4° , which is comparable with previous work [91]. From a Nelson-Riley analysis of the ITO (002) and (006) peaks we determine an out-of-plane lattice constant $a_{\text{ITO}} = 10.106 \text{ \AA}$, which is 0.21 % smaller than the ITO bulk lattice parameter. This uniaxial compression of ITO is likely due to the counteracting in-plane tensile strain of 1.5 % induced by the YSZ substrate.

Fig.4.5 (b) and (c) show RHEED and LEED images of the ITO/YSZ(001) substrates after annealing in UHV. We observe sharp streaks in the RHEED pattern, which indicate an atomically flat ITO (001) surface. The LEED pattern shows cubic symmetry, whereby the second-order ITO reflections coincide with the first-order reflections of the YSZ substrate. We thus conclude, that the ITO film grows epitaxial on YSZ with the cube-on-cube orientation $\text{ITO}(001)||\text{YSZ}(001)$ and $\text{ITO}(010)||\text{YSZ}(010)$, fully consistent with the *ex situ* XRD data.

EuO on ITO: Depth-Profiling of Chemical Composition

Next, the properties of EuO ultra-thin films ($d = 4 \text{ nm}$) grown on ITO(001) virtual substrates are discussed. For sample type (i), we applied an EuO growth mode with $T_S = 400^\circ\text{C}$ and a flux ratio $J_{\text{Eu}}/J_{\text{O}} = 1$, which yields perfectly stoichiometric and single-crystalline EuO thin films on cubic oxide substrates as e.g. YSZ [71]. Fig. 4.6 (b) shows the RHEED pattern of sample type (i). We observe diffraction spots characteristic for epitaxial growth. However, the spots are very broad indicating a rough surface and three-dimensional island growth.

In order to examine the depth-dependent chemical properties of EuO/ITO sample type (i), we used HAXPES to investigate the Eu 3d core level. This core level is spin-orbit (SO) split into a $3d_{5/2}$ and $3d_{3/2}$ component separated by $E_{\text{SO}} = 30 \text{ eV}$ [26]. The $3d_{5/2}$

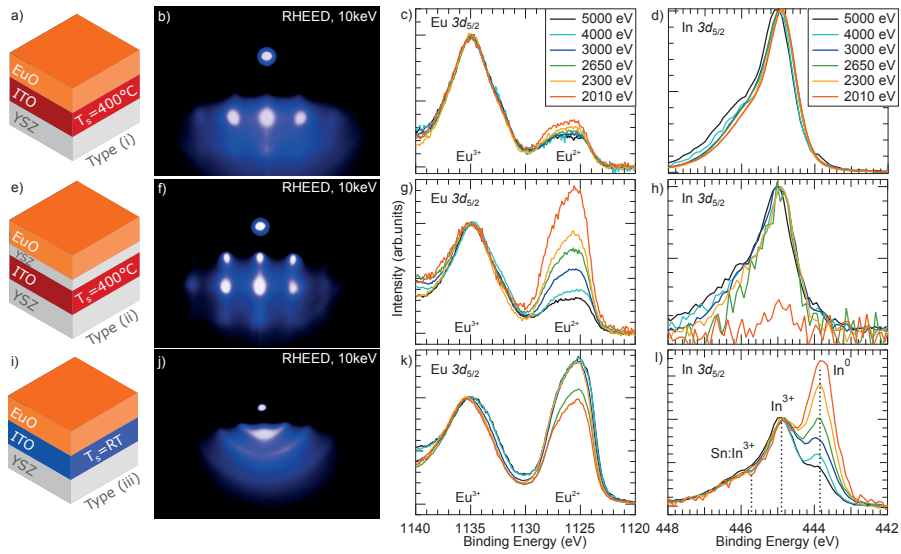


Figure 4.6.: **Top row:** Sample type (i): 4 nm EuO grown at 400°C . **Middle row:** Sample type (ii): 4 nm EuO grown at 400°C with a 2 nm YSZ buffer layer. **Bottom row:** Sample type (iii): 4 nm EuO grown at room temperature. **(a), (e), (i):** Schematic representation of the layer stacking. **(b), (f), (j):** RHEED images taken with 10 keV. **(c), (g), (k):** HAXPES spectra of the Eu $3d_{5/2}$ core level. **(d), (h), (l):** HAXPES spectra of the In $3d_{5/2}$ core level. All spectra are normalized to the Eu^{3+} or In^{3+} components, respectively, except for the 2010 eV spectrum in (h) which could not be normalized due to weak intensity.

component is shown in Fig. 4.6 (c). It reveals a chemical shift between divalent Eu^{2+} contributions – the signature of stoichiometric and ferromagnetic EuO – and trivalent Eu^{3+} , which assigns over-oxidized phases. For a photon energy of 2010 eV, the fit yields a spectral weight of the Eu^{2+} components of 27 % and of $\text{Eu}^{3+} = 73$ %. Obviously, a major amount of over-oxidized phases has formed during growth despite applying a flux ratio of $J_{\text{Eu}}/J_{\text{O}} = 1$.

In order to get depth-sensitive information of the chemical composition, we recorded the Eu $3d_{5/2}$ multiplet with the incident photon energy varying from 2010 eV to 5000 eV, as shown in Fig. 4.6 (c). The corresponding fit results are summarized in Fig. 4.7 (a). We observe, that the relative intensity of the Eu^{2+} component gradually decreases with increasing photon energy, i. e. with increasing bulk sensitivity. This result indicates, that the amount of stoichiometric EuO decreases from the surface towards the EuO/ITO interface.

We therefore conclude that – although the O_2 flux is fine-tuned to match the Eu flux during growth – the ITO virtual substrate likely acts as an additional source of oxygen, resulting in a significantly enhanced fraction of over-oxidized EuO phases mainly located at the EuO/ITO interface. Consequently, the growth conditions need to be refined for synthesis of stoichiometric EuO on ITO.

In the following, we discuss two strategies to suppress the oxygen diffusion from the ITO virtual substrate during EuO growth.

First, we apply the same growth conditions ($T_S = 400^\circ\text{C}$, $J_{\text{Eu}}/J_{\text{O}} = 1$) but insert a 2 nm thick PLD-grown YSZ buffer layer on top of the ITO virtual substrate (sample type (ii)). YSZ was chosen as a buffer layer material, since EuO grows with high crystalline quality directly on YSZ substrates [79]. The results are compiled in the middle row of Fig. 4.6. The RHEED pattern in Fig. 4.6 (f) shows diffraction spots which are characteristic for three-dimensional island growth. However, they are sharper than those observed for sample type (i), thus suggesting a lower surface roughness of the EuO film grown on 2 nm YSZ/ITO. From the HAXPES depth profile in Fig. 4.6 (g), we find that the spectral intensity of the Eu^{2+} components is 60 % for the lowest photon energy (i. e. largest surface sensitivity) and decreases gradually to 25 % for the largest photon energy of 5000 eV (i. e. largest bulk sensitivity). The content of stoichiometric EuO is clearly enhanced compared to sample type (i). However, the EuO/ITO interface is still dominated by over-oxidized phases. Thus, the YSZ buffer layer hinders oxygen diffusion from the substrate but cannot completely prevent it.

Our second strategy to hinder oxygen diffusion from the ITO virtual substrate is to grow EuO directly on ITO using the flux ratio of $J_{\text{Eu}}/J_{\text{O}} = 1$, but with the substrate kept at room temperature. Oxygen diffusion in oxides typically follows an Arrhenius law, and the oxygen mobility in ITO is negligible at room temperature ⁴.

For sample type (iii), the RHEED pattern in Fig. 4.6 (j) reveals diffraction rings that are indicative of a poly-crystalline EuO film. The corresponding HAXPES spectra in Fig. 4.6 (k) show an Eu^{2+} ratio of about 60 % and only small changes of the Eu^{2+} $3d$ spectral intensity within the HAXPES depth profile. The relatively small variations of the

⁴ From the data in ref. [93] the diffusion coefficient was extrapolated to be $1.5 \times 10^{-17} \text{ cm}^2 \text{ s}^{-1}$ at room temperature.

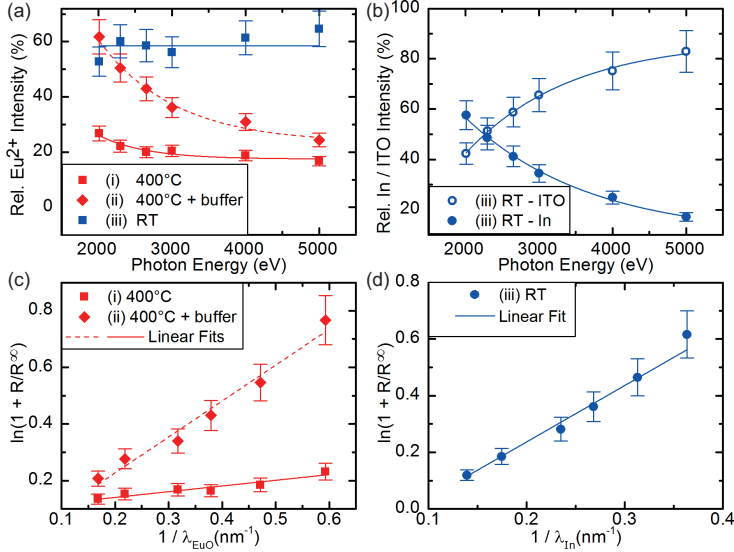


Figure 4.7.: (a): Relative Eu^{2+} intensity as estimated by fits to the HAXPES data shown in Fig.4.6 (c,g,k). (b): Relative intensity I_{ITO} and I_{In} of the HAXPES depth profile shown in Fig.4.6 (l). Lines in (a) and (b) are guides to the eye. (c): Determination of the EuO layer thickness for sample type (i) and (ii) gives $d_{\text{EuO}} = 0.2 \text{ nm}$ and $d_{\text{EuO}} = 1.3 \text{ nm}$, respectively. (d): Determination of the In metal layer thickness for sample type (iii) gives $d_{\text{In}} = 2 \text{ nm}$.

Eu^{2+} intensity indicate that the chemical composition of the EuO layer is homogeneous.

Finally, we performed a complementing HAXPES depth profiling analysis of the In $3d$ core levels of the buried ITO virtual substrate. The spectra of sample types (i) and (ii) are displayed in Fig. 4.6 (d) and (h). They consist of two components: a sharp component located at 444.9 eV, which denotes trivalent In^{3+} (as expected for $\text{Sn}:\text{In}_2\text{O}_3$) [94] and a second, broad component located at 445.7 eV which can be attributed to screening effects caused by the Sn dopants [95].

In contrast, sample type (iii) reveals an additional spectral feature in the In $3d$ core level as depicted in Fig. 4.6 (l). For the largest photon energy (largest bulk sensitivity), the spectra are comparable to those of sample types (i) and (ii), but possess a small shoulder at the low binding energy side of the In^{3+} peak. This feature located at 443.9 eV is characteristic for metallic In^0 [94]. The relative intensities I_{ITO} and I_{In} are shown in Fig. 4.7 (b)⁵. I_{In} increases with decreasing photon energy and dominates the spectrum at the lowest photon energies, i.e. at the highest surface sensitivity. We thus clearly find In metal present at the EuO/ITO interface of sample type (iii).

⁵ I_{ITO} takes both ITO components i.e. In^{3+} and $\text{Sn}:\text{In}^{3+}$ into account (see supporting information).

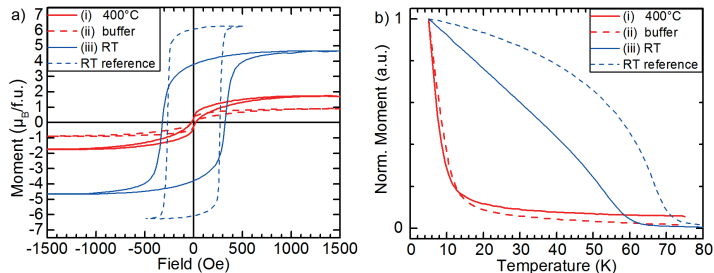


Figure 4.8.: Magnetic characterization of sample types (i)-(iii). For reference, a thicker film is shown (same growth procedure as sample type (iii) but with $d = 9$ nm) **(a):** $M(H)$ hysteresis loops at 5 K. **(b):** $M(T)$ curves with an alignment field of 100 Oe.

In order to estimate the thickness d of the In^0 layer from our HAXPES data we assumed the layer to be discrete. In this case one can apply the relation[35]

$$\ln\left(1 + \frac{R}{R^\infty}\right) = \frac{d}{\lambda_{\text{In}}} \quad \text{with} \quad R = \frac{I_{\text{In}}}{I_{\text{ITO}}} \quad ; \quad R^\infty = \frac{I_{\text{In}}^\infty}{I_{\text{ITO}}^\infty} = \frac{\sigma_{\text{In}}\lambda_{\text{In}}}{\sigma_{\text{ITO}}\lambda_{\text{ITO}}} \quad (4.9)$$

where R is the ratio of the spectral intensities I_{In} to I_{ITO} as they are shown in Fig. 4.7(b), and R^∞ is the ratio of intensities of bulk reference samples of these materials. The latter can be calculated from λ i.e. the respective effective attenuation length (EAL)⁶ and σ i.e. the atomic density. As depicted in Fig. 4.7(d), plotting $\ln(1 + R/R^\infty)$ vs. $1/\lambda_{\text{In}}$ gives a straight line that validates the assumption of a discrete In^0 layer with sharp interfaces and yields a layer thickness $d_{\text{In}} = 2$ nm. The thermodynamic origin of the In layer will be discussed in section 4.5.

In the same way, we analyzed the effective thickness of the EuO layer in samples (i) and (ii), see Fig. 4.7(c). Here, we assume that a discrete EuO layer is present on top of an Eu_2O_3 layer which is in contact with the substrate. For sample (ii), this approach yields a thickness of $d_{\text{EuO}} = 1.3$ nm. This is about 1/3 of the total film thickness which is agreeing reasonably well with the chemical composition of the film (approx. 1/4 Eu^{2+}). For sample (i), we find a value of $d_{\text{EuO}} = 0.2$ nm which would be only 1/20 of the film's thickness. This is much less than expected from the chemical analysis. We conclude that in the case of this sample we cannot assume that a discrete EuO layer is present but rather EuO islands on top of Eu_2O_3 .

Magnetic Properties

We complement the structural and chemical characterization of the EuO/ITO samples by probing their magnetic properties. Fig. 4.8 (a) shows the respective $M(H)$ hysteresis

⁶ EALs are calculated with formula (8) of ref.[96]. The therefor necessary inelastic mean free path (IMFP) and transport mean free path (TMFP) were simulated in SESSA [97].

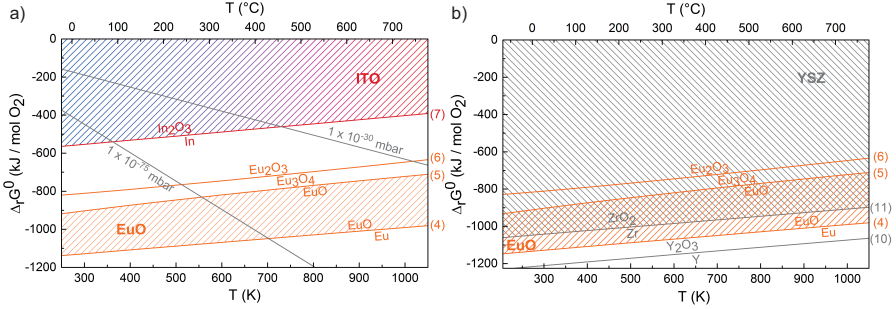


Figure 4.9.: (a): Ellingham diagram for oxygen reactions at the EuO-ITO interface calculated with thermodynamical data from refs. [98, 99]. Gibbs free energy change of reactions (4) - (7) are indicated by straight lines. Stable conditions for EuO and ITO are marked by the hatched areas. Gray lines show constant O_2 -pressures. (b): Ellingham diagram for oxygen reactions at the EuO-YSZ interface.

loops recorded at $T = 5$ K and (b) shows $M(T)$ curves with an alignment field of 100 Oe.

As a reference, we show the magnetic properties of a thicker EuO film ($d = 9$ nm) which was grown in the same way as sample (iii) i. e. deposition onto an ITO virtual substrate at room temperature. For this reference sample, we observe a square magnetic hysteresis loop with a coercive field of $H_C = 300$ Oe and a saturation magnetization of $6.5\mu_B$ per formula unit i. e. close to the bulk value of $7\mu_B$ /f.u. Furthermore, the $M(T)$ curve in Fig.4.8 (b) follows a Brillouin-like shape with a Curie temperature $T_C = 70$ K, thus, almost perfectly matching the bulk value of 69 K. We conclude that EuO with bulk like magnetic properties can be obtained by room temperature deposition onto ITO virtual substrates.

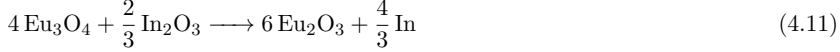
For sample type (iii), we observe a hysteresis loop with $H_C = 320$ Oe and a saturation magnetization of $4.6\mu_B$ per formula unit. We note that the measured magnetization of all samples was normalized by the nominal film thickness of 4 nm. The effective EuO thickness, however, is much thinner due to the presence of Eu^{3+} phases which results in an underestimation of the saturation magnetization of the Eu^{2+} (i. e. EuO) phase. The corresponding $M(T)$ curve shows a Curie temperature of $T_C = 60$ K. This reduced Curie temperature is expected for EuO in the ultra-thin film limit [19, 44].

Consistently, samples (i) and (ii) which contain more Eu^{3+} contaminants show magnetic hysteresis but with further reduced saturation magnetization. We find that T_C is reduced dramatically for these two samples due to a very low effective thickness of the EuO layer. The nominal layer thickness is already 4 nm, but - as pointed out above - the effective thickness of the EuO layer is lower because these two samples contain mostly Eu_2O_3 . Using Eqs. 1, we determined the thickness of the EuO layer in sample type (ii) to be 1.3 nm.

The chemical composition of the samples as reflected by the spectral weight of Eu^{2+} or Eu^{3+} cations is, thus, fully consistent with their macroscopic magnetic properties.

Thermodynamic Analysis and Discussion

Combining the results on the three sample types, we derive the following picture of EuO synthesis on ITO: Besides the oxygen gas which is supplied during the reactive MBE growth process, the ITO virtual substrate is an additional supplier of oxygen (Fig. 4.10(a)). The substrate is reduced by the presence of EuO to In metal while EuO over-oxidizes to Eu_3O_4 and Eu_2O_3 . The chemical reactions taking place at the EuO/ITO interface are



These reactions are thermodynamically favored as we derived from the Ellingham diagram[100] shown in Fig.4.9 a). Here, we compiled the change of the Gibbs free energy ($\Delta_r G^0$) as a function of temperature for any oxidation reaction of the metallic elements involved, which are



$\Delta_r G^0$ of reactions (2) and (3) can be easily estimated because

$$\Delta_r G^0(2) = \Delta_r G^0(5) - \Delta_r G^0(7) \quad (4.16)$$

$$\Delta_r G^0(3) = \Delta_r G^0(6) - \Delta_r G^0(7) \quad (4.17)$$

Stable conditions for EuO and ITO are marked by the hatched areas in Fig. 5 a). We find that these areas do not overlap and that, consequently $\Delta_r G^0(2)$ and $\Delta_r G^0(3)$ are negative (i. e. $< -300 \text{ kJ/mol O}_2$) and thus both reactions are favored as indicated by the arrows in Eqs. (2) and (3).

Therefore, the given thermodynamic conditions prefer the formation of over-oxidized phases at a growth temperature $T_S = 400^\circ\text{C}$ and $J_{\text{Eu}}/J_{\text{O}} = 1$ (sample type (i)). We note, that even with a flux ratio $J_{\text{Eu}}/J_{\text{O}} = 2$ the abundance of over-oxidized phases could not be reduced (see supporting information). Any excess Eu reacts with O from the substrate and, therefore, cannot re-evaporate. Consequently, for EuO synthesis on ITO substrates one cannot benefit from the distillation method.

Hence, oxygen diffusion from the ITO virtual substrate to the EuO film needed to be reduced and we proceeded in two ways: the insertion of a YSZ buffer layer (sample type

(ii)) and the lowering of the growth temperature (sample type (iii)).

EuO is thermodynamically stable in contact with the YSZ buffer as it can be derived from the Ellingham diagram in Fig. 4.9 b). In absence of thermodynamic data for this particular YSZ compound (composition $\text{Zr}_{0.87}\text{Y}_{0.13}\text{O}_{1.935}$), a reasonable approximation is examining the individual components (in particular Zr). We thus compiled the change of the Gibbs free energy ($\Delta_r G^0$) for oxidation reactions of Y and Zr:



Once more, stable conditions for EuO and YSZ are marked by the hatched areas in Fig. 4.9 b). In contrast to Fig. 4.9 a), these areas largely overlap signaling thermodynamic stability. HAXPES data of the Zr *3d* core level (see supporting information) shows only Zr^{4+} , which is the expected valence in YSZ, so that we can conclude that the buffer layer is homogeneous and, indeed, chemically stable.

Recalling the results on sample type (ii), the 2 nm thick YSZ buffer layer clearly improved the EuO stoichiometry. Thus, the buffer layer acts as a kinetic barrier that reduces oxygen diffusion. However, over-oxidized phases are still present at the EuO-YSZ interface. That means that the buffer layer is not a perfect diffusion barrier which is presumably due to the oxygen permeability of YSZ [101, 102] (Fig. 4.10(b)).

Lowering the growth temperature reduces oxygen diffusion more effectively. A homogeneous EuO film containing 60% stoichiometric EuO is obtained (sample type (iii)) but, in turn, the chemical composition of the ITO virtual substrate is substantially modified. After EuO synthesis, In metal is detected at the EuO/ITO interface (Fig. 4.10(c)). The observed reduction of ITO to In metal can solely be explained by the thermodynamic instability of ITO in contact with EuO as derived from Fig. 4.9 a).

As a last point we address the fact that the reduction of ITO to In metal occurs only for sample type (iii), but not for types (i) and (ii). In the latter cases, a surplus of oxygen is present above the interface, but no oxygen deficiency is observed in the ITO substrate. We conclude, that oxygen vacancies occur at the surface of the ITO virtual substrate, but diffuse by thermal activation and are thus diluted below a measurable concentration. In the case of sample type (iii), the ITO virtual substrate suffers a significant oxygen depletion at the interface. Due to the reduced oxygen mobility at room temperature, these vacancies are not replenished and metallic In is present at the interface.

Conclusions

In summary, our study successfully combined a fundamental thermodynamical analysis in terms of solid state chemistry with HAXPES as a modern spectroscopy tool. Applying the non-destructive HAXPES technique yields a deep understanding of the chemical processes at the interfaces of the prototypical all-oxide hybrid EuO/ITO.

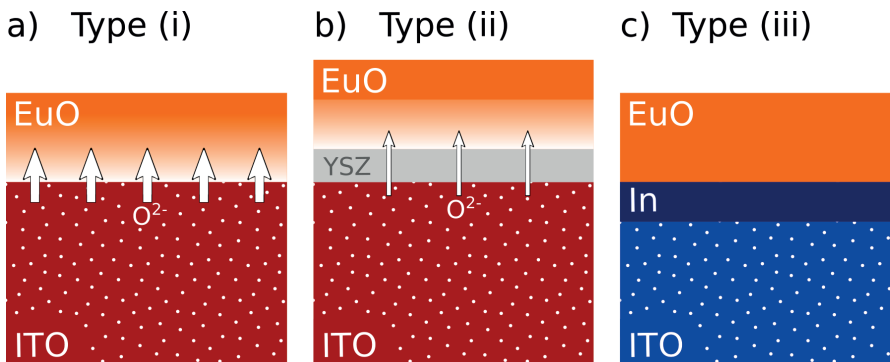


Figure 4.10.: Mechanisms of oxygen diffusion at the EuO/ITO-interface. **(a):** Type (i): O^{2-} from ITO diffuses to the EuO layer and acts as additional source of oxygen during growth. Oxygen is mobile at 400 °C so that oxygen vacancies at the ITO interface are replenished. **(b):** Type (ii): Diffusion of oxygen to the EuO layer is reduced by an YSZ buffer layer. **(c):** Type (iii): O^{2-} reacts with the EuO layer at the interface but vacancies are **not** replenished so that the ITO interface suffers oxygen depletion and metallic In is formed.

We have shown that ITO virtual substrates act as thermally activated additional source of oxygen during reactive MBE growth of ferromagnetic EuO. At elevated growth temperatures over-oxidized phases with inferior magnetic properties were formed. Accordingly, the EuO growth was optimized by lowering the growth temperature. If synthesized at room temperature, EuO films show significantly improved chemical quality with sizable magnetic properties.

Our thermodynamic analysis of oxygen reactions at the EuO-ITO-interface supports the presented HAXPES measurements. It is therefore promising to apply this approach to other oxide-oxide interfaces, in particular to calculate $\Delta_r G^0$ accordingly for all oxygen reactions of the metals M involved:



Suitable substrate and buffer layer materials are promising if they are thermodynamically stable in contact with the functional oxide over layer. Even though MBE growth is largely governed by kinetic factors, thermodynamic stability signals the absence of a driving force for interface reactions.

Moreover, the oxygen conductivity turns out to be a major criterion for carefully choosing materials and synthesis temperatures. Generally, our methodical approach may serve as guideline for optimizing the growth and the interface properties of all-oxide hetero-structures.

4.6. Oxygen free growth of EuO/SrTiO₃

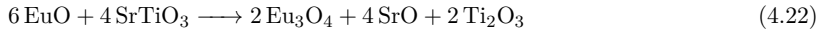
The adsorption-limited growth mode has become somewhat of a standard mode of thin film growth of EuO for inert substrates. Without any doubt, finding the appropriate parameters is a complex task as substrate temperature, oxygen partial pressure and Eu-flux need to be controlled simultaneously. Consequently alternative routes to synthesize EuO, are currently discussed in literature.

For example in one recent approach using a "topotactic" growth mode, the authors deposit Eu₂O₃ in a HV environment onto a substrate. The Eu₂O₃ is capped with a Ti metal top layer. The sample is heated to high temperatures, which leads to the oxidation of Ti to TiO₂, while reducing the Eu₂O₃ to stoichiometric EuO. This is accompanied by a crystal match with the underlying substrate. [15]

However, this procedure limits the choice of over layer material to Ti and the thickness of the over layer must be very closely controlled, if a complete oxidation is the goal of the experiments. As EuO is often suggested as a candidate for tunnel experiments, this TiO₂ over layer cannot be used, as it is a wide band gap insulator and would make tunneling experiments impossible.

We propose a new growth mode in which we utilize the oxygen provided by the substrate. Our approach is tailored for the transition metal dichalcogenide SrTiO₃, yet it can be extended to any oxide substrate with comparable oxygen mobility, as we show in Section 4.7. Previous reports of EuO growth on SrTiO₃ have only shown, that growth directly on EuO is not possible [6] and a fabrication of EuO on SrTiO₃ was always performed using a buffer e.g. SrO[4] or BaO [5].

Here, we consider again the thermodynamic properties of EuO and SrTiO₃ after Ellingham for the possible reactions of Eu on SrTiO₃



These reactions are thermodynamically favored for temperatures above $T_S = 300^\circ\text{C}$ as we derived from the Ellingham diagram [100] shown in Fig.4.11 (b). Here, we compile the change of the Gibbs free energy ($\Delta_r G^0$) as a function of temperature for any oxidation reaction of the metallic elements involved, which are



Figure 4.11 shows the behavior of Europium and its oxides in proximity to SrTiO₃ by the aforementioned reactions. We can deduce that SrTiO₃ is a suitable candidate for EuO growth on SrTiO₃, as the predicted stable oxide is EuO.

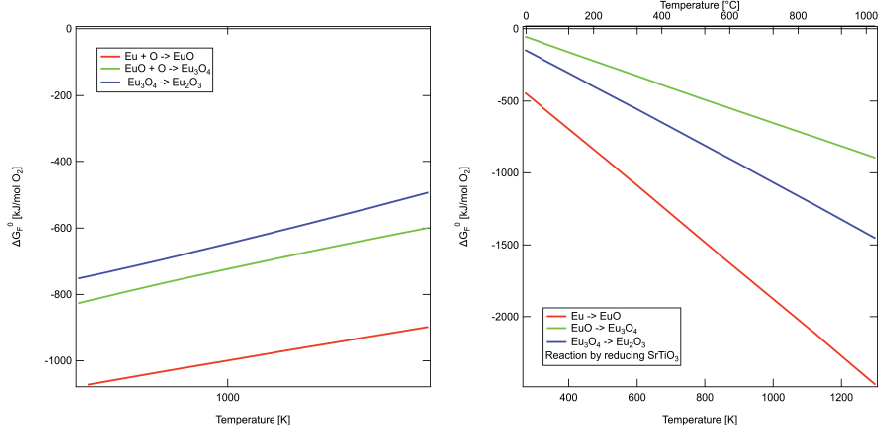


Figure 4.11.: Ellingham diagram of (a) stability regions of europium oxides in the adsorption limited case and (b) SrTiO₃ reduction forming Eu oxides.

However, the Ellingham analysis assumes an equilibrium state, which is hardly the case for reactive oxide MBE growth. For SrTiO₃, a multitude of non-equilibrium states are known, such as the formation of oxygen vacancies with activation energies of $E_A = 578 \text{ kJ/mol/O}_2$ [103].

In the following, a systematic study of the growth modes of EuO/SrTiO₃ is presented as a function of the growth time t and the temperature of the substrate T_S as obtained from the calibrated pyrometer at constant flux $j_{Eu} = 0.13 \frac{\text{\AA}}{\text{s}}$. Due to the fact that there is no gaseous oxygen added, there is no need for this additional calibration step and thereby the complexity of the synthesis is reduced significantly.

The growth is performed in a step-wise mode. Therefore, the growth time is given by

$$t = \sum_i t_{i,step} \quad (4.28)$$

with the deposition time of each step $t_{i,step}$. In between two steps, the sample is cooled down to room temperature and analyzed with LEED, RHEED and XPS. In this way, we obtain a growth profile of Eu/SrTiO₃ as a function of t and T_S .

Figure 4.12 (a) displays an XPS spectrum of the Eu $3d_{5/2}$ core-level using step-wise growth at $T = 500^\circ\text{C}$. We find at $t = 1 \text{ min}$ a spectrum with a mixture of Eu²⁺ and Eu³⁺ components. The relative weight of Eu₂O₃ and EuO amounts to 15% and 85%. Contributions of Eu metal are absent from the spectrum, which shows that the redox process with the substrate is active and the Eu metal is oxidized, indeed slightly over-oxidized. The spectral weight from Eu₂O₃ decreases over time and leads to a negligible amount of $k_{Eu_2O_3} = 0.01$ in the spectrum at $t = 20 \text{ min}$. We find, that the film growth leads in all cases to the formation of mostly EuO.

Figure 4.12 (c) depicts the same step-wise deposition of redox Eu at lower temperature

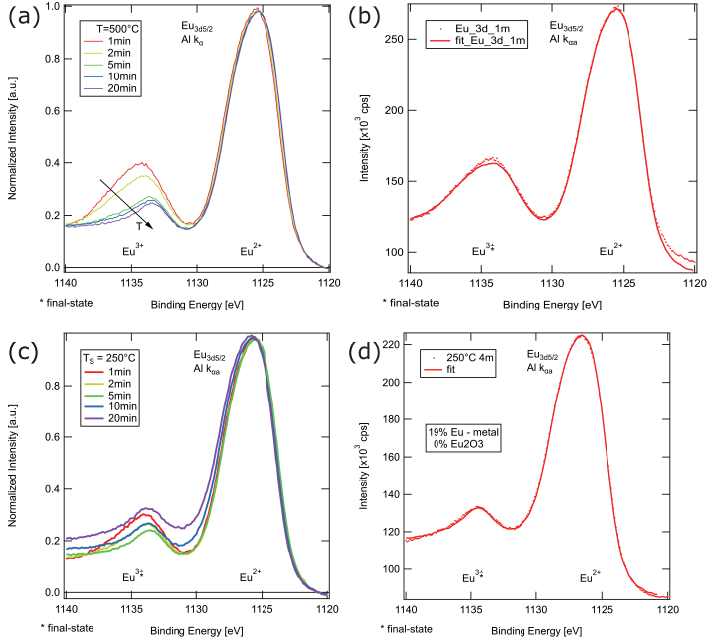


Figure 4.12.: (a) Time evolution of 500 °C growth, (b) fit to $t = 1$ min, showing a mixture of mostly EuO and some Eu_2O_3 and (c) fit to films grown at 250 °C at $t = 4$ min showing a metallization of the growing film.

of $T_S = 250$ °C. For $t < 5$ min, the spectrum is composed of EuO and Eu_2O_3 fractions. However, at $t > 5$ min the Eu $3d_{5/2}$ final state peak shifts upwards, indicating Eu metal inclusion in the film. This metal inclusion continues to increase over time. We conclude that at this temperature Eu metal does not re-evaporate from the surface.

Therefore, the redox growth of EuO films without additional oxygen is limited to temperatures $T_S > 250$ °C on SrTiO_3 .⁷

Having successfully applied the fit routine to both over-oxidized and metal-rich spectra we conclude, that a quantitative chemical determination is possible.

We prepare samples with deposition times of $t = 60$ min in the temperature range from $T_S = 20$ °C to 800 °C and apply the fit routine to all samples. The results are compiled in Figure 4.13, which shows in (a) the Eu metal contents and in (b) the content of Eu_2O_3 as a function of growth time and temperature. Figure 4.13 (c) shows a summary by plotting the Eu-metal content of the last time step and Eu_2O_3 of the first time step. We find, that the dependence of the two parameter on T_S is strongest at these time steps.

In Figure 4.13 (a) the Eu metal content is shown. For $T_S = 20$ °C, the metal content

⁷ Note that 1ML and 2ML growth of EuO is indeed possible and leads to the formation of a two-dimensional electron gas interface state as reported in Section 5.1.

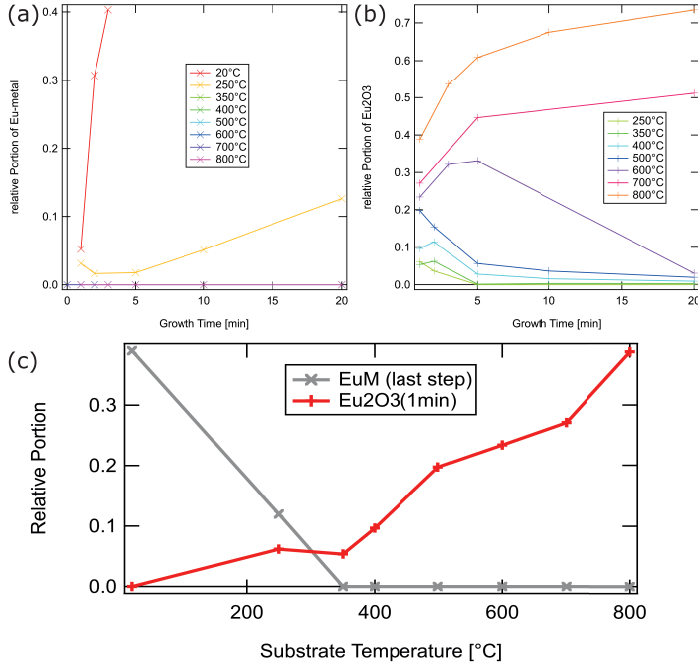


Figure 4.13.: (a) Fit results for the Eu^0 component. Growth at room temperature and $T_S = 250^\circ\text{C}$ lead to metal inclusions in the film. Higher T_S show no Eu in the XPS spectrum. (b) Fit results of the Eu_2O_3 component. All spectra $T_S \leq 600^\circ\text{C}$ show a small and decaying contribution from Eu_2O_3 . For $T_S \geq 700^\circ\text{C}$ the Eu_2O_3 content is increasing with growth time. (c) Compilation of the study by comparing the Eu_2O_3 content of the first minute with the content of Eu at the end of the deposition.

increases linearly with growth time. Clearly the Eu metal does not re-evaporate and the oxygen is immobile in the substrate. For $T_S = 250^\circ\text{C}$, the first 5 minutes of deposition indicate a small Eu content and for $t > 5$ min the metal component increases. For higher T_S no Eu metal is observed by XPS. Therefore, we conclude, that Eu re-evaporation is a dominant process for $T_S > 250^\circ\text{C}$.

In Figure 4.13 (b), the films grown prepared at $T_S = 250^\circ\text{C}$, 300°C , 400°C and 500°C show an exponential decay of the Eu_2O_3 fraction with t . This indicates, that only the interface is responsible for the Eu_2O_3 signal, as the Beer-Lambert law predicts an exponential decay of a buried layer peak with the over layer thickness.

For $T_S = 600^\circ\text{C}$, 700°C and 800°C , the Eu_2O_3 content increases with t . In the case of $T_S = 600^\circ\text{C}$ the Eu_2O_3 content decreases after $t = 5$ min again and at $t = 60$ min only EuO is observed. For $T_S = 700^\circ\text{C}$ and 800°C the content of Eu_2O_3 increases monotonically in the studied time regime. Therefore, $T_S = 600^\circ\text{C}$ redox EuO growth on

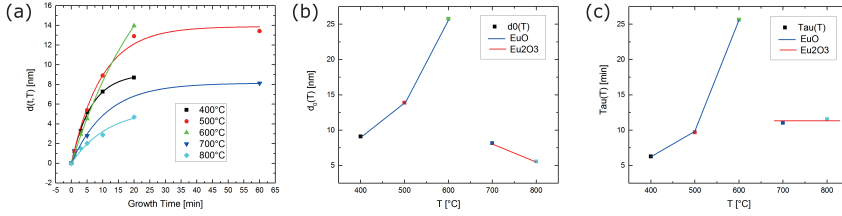


Figure 4.14.: (a) $d_{XPS}(t, T)$ indicating a Mott-Cabrera type growth and fit to the data (b) dependence of $d_0(T)$ indicating a different behavior at $T_S = 600^\circ\text{C}$ (c) dependence of $\tau(T)$ indicating the same crossover temperature behavior. Concluding we find, that the EuO growth scales with T_S indicating an increasing O availability, while Eu_2O_3 growth is declining. As the oxygen availability scales also with T_S it is expected, that at the crossover the sticking probability of Eu or its oxides crosses the border, where a re-evaporation is more likely, than sticking and reacting with O.

SrTiO_3 is only possible in the range $T_S = 300^\circ\text{C}$ to 600°C .

In Figure 4.13 (c) we present the summarized results of the study as a function of growth time. The above analysis is supported by the figure in such, that the discussed regimes can be identified. Additionally, the almost linear dependence of Eu_2O_3 content on T_S becomes clear, indicating an ever increasing supply of oxygen provided by SrTiO_3 .

The complex behavior of the growth of $\text{EuO}/\text{SrTiO}_3$ can be attributed to three main factors: kinetics of the oxygen reservoir from the substrate, kinetics of Eu on the surface of SrTiO_3 (and its concomitant re-evaporation) and the thermodynamics of the reaction.

In conclusion, we report a possible new route for the synthesis of $\text{EuO}/\text{SrTiO}_3$ by supplying no gaseous oxygen at all. We have identified a T_S window in which stoichiometric EuO can be grown on SrTiO_3 without calibrating the oxygen flux at all and thereby have found a simple approach for reproducible EuO synthesis.

Thickness dependence of EuO over layers on T_S

As the EuO film grows, the oxygen from the substrate has to diffuse through the growing film. Therefore, each subsequent layer of EuO acts as an additional diffusion barrier and limits the availability of O for the next Eu layer. Consequently the EuO thickness d_{XPS} will not be a linear function, but a saturation is expected.

In order to study the EuO thickness, we analyze the damping of the substrate core levels and apply the intensity model of a buried layer

$$I(d_{XPS}) = I_0 \exp\left(-\frac{d_{XPS}}{\lambda_{\text{IMFP}}}\right) \Leftrightarrow d_{XPS} = -\lambda_{\text{IMFP}} \ln\left(\frac{I}{I_0}\right). \quad (4.29)$$

Here, $I(d_{XPS})$ is the intensity of a core-level peak with an over layer of thickness d_{XPS} , $I_0 = I(d = 0)$ and λ_{IMFP} is the inelastic mean free path for the kinetic energy of the escaping electrons.

The Ti $2p$ core-level is chosen as no contributions of EuO spectral weight overlap the

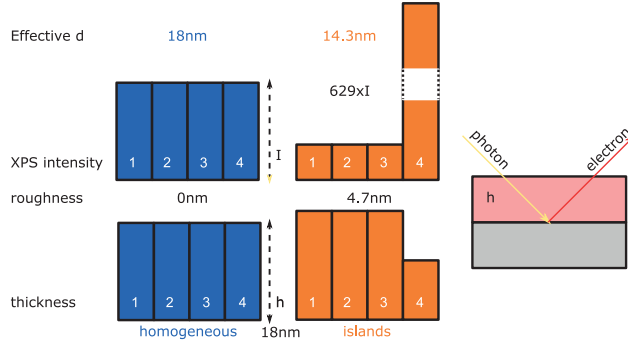


Figure 4.15.: Bottom: Comparison of a flat surface (blue) and a surface with island growth (orange). Both surfaces have the same mean thickness d_{mean} . Top: Schematic representation of the XPS intensity of a substrate peak as it is damped by the over layers and the calculated effective thicknesses d_{XPS} for the two films.

Ti $2p$ spectrum for the Al $K\alpha$ x-rays. In this regard, the Ti $2p$ spectra are fitted with the Unifit software using the XPS doublet fitting routine. The peak parameters are based on available literature values for FWHM and Lorentzian and Gaussian broadening supplied by the software. A Tougaard background with universal cross section and a linear polynomial is applied to subtract the background signal of inelastically scattered electrons.

In [Figure 4.14](#) the EuO thickness as a function of t and T_S is depicted. We find, that the growth rate declines exponentially with the over layer thickness and model the thickness as

$$d(t) = d_0 \cdot (1 - \exp(t/\tau)) \quad (4.30)$$

where d_0 , the final thickness, and τ , the time constant, are plotted as a function of T_S in [Figure 4.14](#). This growth type is indicative of a Mott-Cabrera type growth [104]. Comparing these growth profiles with the oxidation of Fe [105] (which is the inverted process, but is expected to adhere to the same law), we find that $d(t)$ resembles the same shape and therefore conclude, that the oxidation of Eu under reduction of SrTiO₃ is a process, which is limited by the ionic oxygen conductivity of the oxide substrate.

Both parameters d_0 and τ depend on the temperature and show a discontinuity at $T_S = 600^\circ\text{C}$. From the analysis of $d_0(T_S)$ we see, that higher substrate temperatures result in thicker EuO films. Hereby it is possible to define a film thickness by choosing the temperature and then supplying Eu metal until the growth has stopped. At $T_S > 700^\circ\text{C}$ the final thickness is discontinuous and reduced, this process is continued for $T_S = 800^\circ\text{C}$. This could indicate, that the re-evaporation of Eu metal becomes much faster than the chance of reacting with a oxygen atom. Another interpretation could be, that due to the dominant formation of Eu₂O₃ the film grows mostly as islands.

In [figure 4.15](#) we demonstrate, that the growth of a island type over layer on a

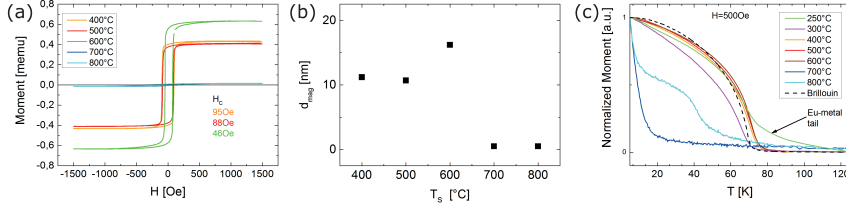


Figure 4.16.: (a) Compilation of the $M(H)$ data of EuO films grown for varying T_S . H_C decreases with increasing T_S to 46 Oe for the magnetically softest film measured at 5 K. (b) d_{mag} as a function of T_S indicating a significant thickness of EuO and an optimal growth temperature at $T_S = 500^\circ\text{C}$ measured at 5 K. (c) Normalized $M(T)$ curves as a function of T_S indicating metallization below $T_S = 250^\circ\text{C}$ and hardly any ferromagnetic response for $T_S \geq 700^\circ\text{C}$. The total thickness of the system is $d = d_{mag} + d_{not-mag}$.

substrate leads to significant deviation in the obtained d_{XPS} . Due to the exponential dependence of the substrate core-level damping on the over layer thickness, island growth leads to a significant deviation from the expected intensity. This is even the case, when the mean thickness d_{mean} is the same for a homogeneous layer and a layer with island growth. In the shown example, a roughness of $a_{RMS} = 4.7\text{nm}$ leads to a reduction from $d_{mean} = 18\text{nm}$ to $d_{XPS} = 14.3\text{nm}$.

We propose a Stranski-Krastanov growth mode for the Eu_2O_3 (as seen later in the RHEED analysis). Until $t = 10\text{min}$ we observe a significant decrease in the substrate core-level intensity (which indicates an increase of d_{XPS}). Then the island growth becomes dominant and leads to an imperfect coverage of the substrate. This leads to a constant intensity of the substrate core-level, as the uncovered substrate areas dominate the signal.

All in all we find, that in the temperature window from 300°C to 600°C a growth of EuO films on SrTiO_3 is possible utilizing the substrate supplied oxygen alone. This approach to synthesize stoichiometric EuO is a new route to synthesize high quality EuO thin films and allows to freely chose the over layer, while completely avoiding the necessity to tune the oxygen partial pressure.

Magnetism of oxygen free grown EuO films

In this section we are going to analyze the magnetic properties of Europium oxides grown by the previously described method. In section 2.1.2 we have shown, that EuO is a ferromagnet with a $T_C = 69\text{K}$ and $M_S = 7\mu_B/\text{f.u.}$

The magnetometer response of the sample is usually normalized by the thickness and surface area of the sample. Hereby one obtains the volumetric magnetic moment per formula unit. However, this approach only applies, if the film is purely made out of EuO. This is not a valid assumption, as the XPS analysis in the previous section has shown that some Eu_2O_3 cannot be excluded in the films.

Now the known properties of EuO films are used to obtain a magnetic EuO thickness

d_{mag} from the following equation

$$M_S(d_{mag}) \stackrel{!}{=} 7 \mu_B/\text{f.u.} \Leftrightarrow M(H) = \frac{M_{meas}}{d_{mag}} \quad (4.31)$$

where M_S is the saturation magnetization, $M(H)$ the magnetic moment as function of the applied field H and M_{meas} the measured magnetic moment in units of μ_B m.

Hysteresis loops of the samples are presented in figure 4.16 along side with the corresponding $d_{eff}(T_S)$. The hysteresis loops are open squares and show a ferromagnetic response for $T_S = 400^\circ\text{C}$, 500°C and 600°C . The magnetic moment and the coercive field $H_C \approx 90$ Oe of the first two temperatures is comparable. For $T_S = 600^\circ\text{C}$ the saturation moment is higher, while H_C is reduced to 46 Oe. For $T_S > 600^\circ\text{C}$ the magnetic moment is almost reduced to zero and we obtain the behavior of a paramagnetic Eu₂O₃ film, as expected from the XPS analysis.

Comparing the magnetic thickness d_{mag} with the thickness d_{XPS} we find, that there are deviations between the effective XPS thickness d_{xps} and d_{mag} . As explained above one aspect of this deviation can be attributed island growth. Additionally, it has to be taken into consideration, that the ferromagnetic signal is only caused by EuO. Therefore, the total thickness of EuO $d_{XPS, \text{EuO}}$ is the relevant and $d_{XPS} = d_{\text{Eu}_2\text{O}_3} + d_{\text{EuO}} + d_{\text{Eu}}$ has to be reduced consequently.

In Figure 4.16 (c) the normalized $M(T)$ curves for EuO films grown at varying T_S are presented. As expected from the XPS analysis, the curve at $T_S = 250^\circ\text{C}$ shows a pronounced magnetic tail, indicating the presence of Eu metal in the EuO film. The curves at $T_S = 300^\circ\text{C}$, 400°C , 500°C and 600°C show the expected Brillouin function dependence and therefore indicate a stoichiometric EuO growth. A small degree of metal inclusion cannot be excluded in this analysis, as the Curie temperature is increased to $T_C \approx 75$ K. At higher $T_S > 700^\circ\text{C}$ we find a steep decline of $M(T)$ in accordance with the expected behavior of paramagnetic Eu₂O₃.⁸

X-ray diffraction on EuO/SrTiO₃ heterostructures

We perform X-ray diffraction (XRD), X-ray reflection (XRR), reciprocal space mapping (RSM), RHEED and LEED on the samples in this study to obtain the structure, thickness and relative orientation of the prepared films. For *ex situ* studies the films are capped with 10 nm of MgO to protect the films against further oxidation.

In Figure 4.17 (a) a XRD survey of the prepared films is depicted. In line with the previous analysis, the expected peaks for the substrate and the film are present in the spectrum. In accordance with the crystal structure SrTiO₃ (00l) peaks are observable, while for EuO and Eu₂O₃ the fcc lattice restricts (hkl), so that they can only be all even or all odd leading to (00 2*n) peaks. At $T_S > 600^\circ\text{C}$ the films only show reflexes for Eu₂O₃, indicating that the EuO fractions in XPS are not growing epitaxially.

The width of the rocking curve σ is a measure for the amount of misorientation of grains grown in the film. We obtain σ at the EuO (002) from an ω scan at $2\theta_{\text{EuO}(002)}$. Figure 4.17 (b) shows the results of the rocking curves. We find, that $\sigma = 1.05^\circ$ is lowest

⁸ The peak at $T_S = 800^\circ\text{C}$ is due to an oxygen inclusion in the magnetometer caused by a leak in the chamber.

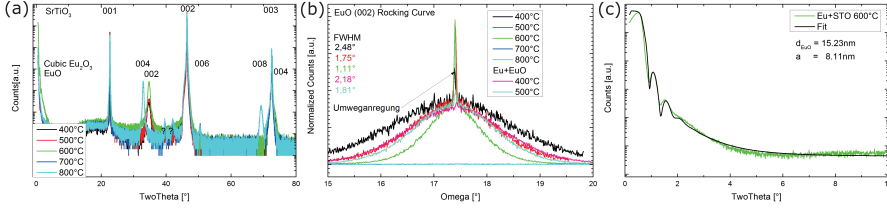


Figure 4.17.: (a) XRD Survey spectra of films grown at varying T_S showing the crystalline contributions to the film growth. (b) Rocking curve (RC) of the EuO(002) peak for the same set. A sharp spike is observed on top of the peak. This can be attributed to Umweganregungen as explained in the text at A.1. (c) XRR spectrum of a EuO film grown at $T_S = 600^\circ\text{C}$ exhibiting a film thickness of $d_{XRR} = 15.23\text{ nm}$.

at $T_S = 600^\circ\text{C}$, which is below reported values for EuO grown on oxides such as MgO [6]. At $T > 600^\circ\text{C}$ the measurement of the EuO (002) rocking curve shows an empty spectrum, as there is no crystalline EuO in the film.

The thickness of the films can also be evaluated by XRR. Shown in Figure 4.17 (c) is a XRR spectrum for the $T_S = 600^\circ\text{C}$ sample. A significant roughness of $a_{RMS} = 8.11\text{ nm}$ is found. This finding further underscores the assumed island growth mode as is also depicted in Figure 4.15.

Since EuO and SrTiO₃ are different with respect to their crystal structure and lattice parameter it is worth studying the relative orientation of EuO on SrTiO₃. The relative orientation can be obtained by rotating around ϕ while observing an XRD peak with in- and out-of-plane components. However, in this study we have made use of the reciprocal space mapping technique (RSM) instead. We obtain a diffractogram of the SrTiO₃ (113) and the EuO (204) peak. If both crystals were grown cube on cube, these peaks are at a 45° angle with each other in the xy-plane.

The result of the RSM is shown in Figure 4.18. We observed both aforementioned peaks very close to each other. This indicates, that the EuO grows along the (110) direction of SrTiO₃ while preserving the (001) direction (as the out of (002) peaks could be observed previously). The peak of EuO (204) is not symmetric. In accordance with Section 3.5, the spread in the peak is interpreted as mosaicity of the grown film.

The substrate reflex shows a double peak structure, which could be assumed to be a twinned crystal, however we show, that this double peak structure is caused by the polychromatic X-ray excitation of the measurement. We fit both of the peaks and compare the Bragg angles $2\theta_i$ to find

$$0.999689 = \frac{\lambda_1}{\lambda_2} \approx \frac{\sin(\theta_1)}{\sin(\theta_2)} = 0.999408 \quad (4.32)$$

where λ_i denotes the wavelength of Cu $K_{\alpha 1}$ and Cu $K_{\alpha 2}$ radiation. The above equation is obtained when the Bragg condition for the same XRD peak is applied to $\lambda_{1,2}$ and we solve for λ . Thereby the angular spread of both peaks is explained by the excitation with both Cu aforementioned wavelengths.

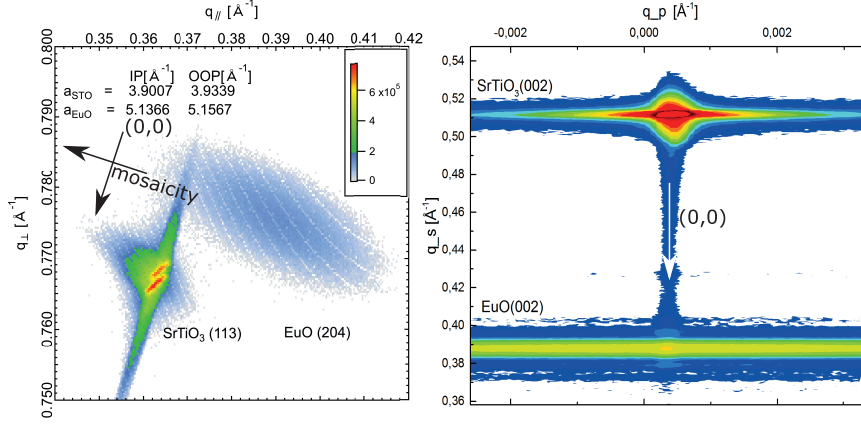


Figure 4.18.: (a) Reciprocal space map (RSM) of asymmetric EuO and SrTiO₃ peaks, revealing the lattice relationship of EuO(110)/SrTiO₃ (100) and EuO(001)/SrTiO₃ (001). (b) RSM of the two out of plane peaks.

The substrate peak shows broadening in the 2θ direction. Due to the different intensities of the substrate and film reflexes, this effect is overemphasized in the diffractogram. In fact the FWHM of the EuO σ_{EuO} peak is a factor of

$$\begin{pmatrix} \sigma_{EuO}(q_{\parallel}) \\ \sigma_{EuO}(q_{\perp}) \end{pmatrix} = \begin{pmatrix} 11.8 \cdot \sigma_{SrTiO_3}(q_{\parallel}) \\ 7.6 \cdot \sigma_{SrTiO_3}(q_{\perp}) \end{pmatrix} \quad (4.33)$$

larger than that of the substrate.

In conclusion, we have shown, that redox grown EuO grows with epitaxial integration on SrTiO₃ (001) with the orientation EuO(110)/SrTiO₃ (100).

Synthesis of "thick" EuO films

As the redox growth of EuO limits the film thickness $d < 15$ nm, we present a two step process for deposition of thicker stoichiometric EuO films.

The two step mode is a good solution to the expected interfacial over-oxidation due to the oxygen diffusion in SrTiO₃ at higher temperatures that had in the past lead to the deposition of EuO on SrTiO₃ only by using buffer layers. We propose to use $T_S = 500$ °C, as the crystal structure is improved at higher temperatures, while the oxygen diffusion is still moderate enough. The XPS analysis showed no significant over-oxidation of EuO after $t > 5$ min therefore the first step is chosen to evaporate Eu only for this amount of time. Hereafter the growth is continued while supplying oxygen at $p_0 = 1.6 \times 10^{-8}$ Torr, the pressure previously determined for the deposition of stoichiometric EuO.

We compare the results of this preparation by preparing a film of similar thickness and compare it with the oxygen free grown specimen in Figure 4.17 (b) denoted as Eu+EuO. We find that the growth with oxygen reduces σ . As $\sigma(600$ °C) is still lower we interpret

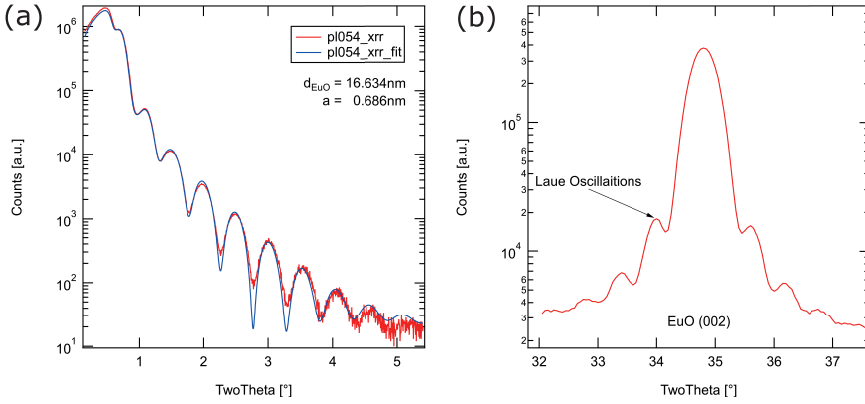


Figure 4.19.: Left: XRR scan of a composite grown sample at $T_S = 500^\circ\text{C}$. The composite growth method here allows a significant reduction of the film roughness while avoiding over oxidation at the interface. Right: XRD of EuO (002) showing Laue oscillations, which are an indicator for high quality crystalline films.

the influence of growth with added oxygen smaller, than growing at higher temperature.

Finally we show in [Figure 4.19](#) (a) the XRR scan and (b) XRD of the EuO (002) peak of a film grown in the two-step mode at $T_S = 500^\circ\text{C}$. We find a significantly improved surface roughness of $a = 0.6\text{nm}$ and $d = 16.6\text{nm}$. Finally the XRD analysis shows a noticeable improvement, as we observe Laue oscillations around the EuO (002). This feature is only observed for high quality crystals, i.e. low surface roughness.

In this way we have presented a way to stabilize EuO on SrTiO_3 by combining the novel approach of oxygen free-growth by a redox with the substrate with the regularly known adsorption limited growth to gain flexibility of arbitrary film thicknesses at low surface roughness.

LEED and RHEED of O-Free grown EuO films

To conclude the growth study we present RHEED and LEED analysis of the prepared films.

[Figure 4.20](#) (a) depicts the growth of EuO on SrTiO_3 along the SrTiO_3 (110) direction at $T_S = 600^\circ\text{C}$. The RHEED pattern of the substrate shows dots of the Laue circle and weak RHEED streaks indicating a substrate with small degree of misorientations. In addition we observe Kikuchi lines, which show a high degree of crystallinity.

During the EuO film growth, the RHEED streaks become more pronounced and then at $t = 10\text{min}$ and 20min RHEED spots are observed along the RHEED streaks. This indicates, that the EuO film grows in a Stranski-Krastanov growth mode, first wetting the substrate, and then continuing with island growth.

In order to evaluate the growth as a function of the growth temperature, a RHEED analysis has been performed on all specimen and is depicted in [Figure 4.20](#) (b). We find, that for $T_S = 250^\circ\text{C}$ the RHEED pattern comparable with that of Eu-metal rich films

[71]. For the temperatures $T_S = 300^\circ\text{C}$, 400°C , 500°C and 600°C comparable RHEED patterns of EuO are found as described in the previous paragraph. We find sharper RHEED spots for increasing temperature indicating less mosaicity for higher growth temperatures, in agreement with our XRD results.

The high temperature growth $T_S = 700^\circ\text{C}$ and 800°C shows a surface reconstruction of (2×2) on the growing film, indicating a completely different growth mode, which agrees with the magnetic, XRD and XPS analysis previously presented.⁹

Finally, LEED has been performed on the substrate and the grown film after $t = 20$ min for the $T_S = 600^\circ\text{C}$ film as shown in (c) and (d) of Figure 4.20. The substrate exhibits sharp LEED spots on a square lattice (orange) as expected from the SrTiO_3 lattice. The film exhibits spots in accordance with a 45° rotated EuO lattice (blue) which confirms the analysis from the RSM measurements on the SrTiO_3 (113) and EuO (204) peak. Additionally, even observation of a LEED pattern for the EuO film indicates that the film grows in with an epitaxial integration to the substrate and the surface of the grown film exhibits terraces larger than the coherence length of the LEED electron beam.

4.7. Application of oxygen free growth of EuO on other oxides

In this section we evaluate experimentally whether a certain selection of oxides exhibits a significantly large redox process with Eu metal. The growth study of EuO on ITO and SrTiO_3 demonstrated that Eu metal is reactive metal, which can react with an oxidic substrate by forming Eu oxides. We found, that ITO is due to its thermodynamic properties is not a suitable candidate for EuO growth. On SrTiO_3 however, a large temperature range has been identified in which elemental Eu metal reacts with SrTiO_3 to form thin layers of stoichiometric EuO with thicknesses up to $d \approx 15$ nm. We have then shown, that a combination of oxygen free growth and the distillation condition allows a successful preparation of thicker EuO films on SrTiO_3 . Now we use the ionic conductivity of oxygen in oxides to make a prediction for a suitable EuO growth on further oxide materials.

As a first step, we grow a SrO over layer on SrTiO_3 in order to enhance the surface mobility of adsorbed Eu [23] and use the low oxygen conductivity of SrO as an oxygen barrier. The study is further performed on substrates of yttria-stabilized zirconia (YSZ), LaSrAlTiO_3 (LSAT), LaAlO_3 (LAO) and MgO. These oxides span a wide variety of lattice constants, lattice structures and ionic oxygen conductivity.

SrO is grown using reactive MBE with elemental Sr (99.9% purity) and an oxygen partial pressure of $p_{ox} = 1 \times 10^{-7}$ Torr on TiO_2 terminated SrTiO_3 . The growth is performed at $T_S = 600^\circ\text{C}$. We deposit 1ML, 4ML and 10 nm of SrO on SrTiO_3 prior to depositing $t = 5$ min of Eu on the SrO capped SrTiO_3 .

We use the logarithm of intensity of the Eu $3d_{5/2}$ core-level as a measure of the

⁹ $T_S = 250^\circ\text{C}$ and 800°C are obtained along SrTiO_3 (100).

thickness because

$$I(d) = I_\infty \cdot \left(1 - \exp\left(-\frac{d}{\lambda_{\text{IMFP}}}\right)\right) \Leftrightarrow d = -\lambda_{\text{IMFP}} \ln\left(1 - \frac{I}{I_\infty}\right), \quad (4.34)$$

where $I(d)$ is the intensity of a layer with thickness d and I_∞ the intensity of an infinitely thick layer.

Due to the fact, that the intensity scales with the inelastic mean free path of the escaping electrons, the thickness determination is only accurate for $d < ID = 3\lambda_{\text{IMFP}} \approx 4.8$ nm. Therefore, the samples are prepared with a deposition time of $t = 5$ min, leading to a theoretical coverage $d = 3.9$ nm.¹⁰

Figure 4.21 (a) shows the spectrum of Eu $3d_{5/2}$ for the specified oxides. The spectra have been recorded under completely identical parameters. Curves have been corrected for charging and have been set to the same level of background from inelastically scattered electrons. The spectra all exhibit the signature of pure Eu^{2+} . Due to this all of the selected oxides are possible growth candidates for EuO. We find, that the EuO peak for SrTiO_3 is the most intense. Depositing 1ML and 4ML of SrO reduces the intensity significantly. This indicates already, that SrO acts as an effective oxygen barrier. Increasing the thickness to $d = 10$ nm, the SrO buffer layer reduces the oxygen flux even more and effectively the intensity is reduced to $I_{\text{SrTiO}_3}/2$.

In Figure 4.21 (b) the intensity of the Eu^{2+} is compared with single crystal data for oxygen ionic conductivity of the substrate[106, 107]. Due to this, it can be shown, that the oxygen ion conductivity can be used as a gauge to the thickness of the redox-grown over layer.

We conclude, that all oxides (MgO,YSZ,LAO,LSAT) and the SrO/SrTiO₃ heterostructures can be used as a template for the synthesis of EuO based hetero structures. This can be especially of interest for the realization of EuO/LAO heterostructures [108], where recently a two-dimensional electron gas has been predicted much like that of LAO/SrTiO₃ and as the next chapter will show, the two-dimensional electron gas from EuO/SrTiO₃ and EuO/BaTiO₃.

In this way, we present a route to identify suitable substrates by their ionic oxygen conductivity for redox growth of EuO over layers and thereby extend the redox growth method that was developed on SrTiO₃ to a larger range of oxides.

¹⁰ Values for $\lambda_{\text{IMFP}}(\text{EuO})$ calculated with SESSA 2.0 using Al K_α radiation.

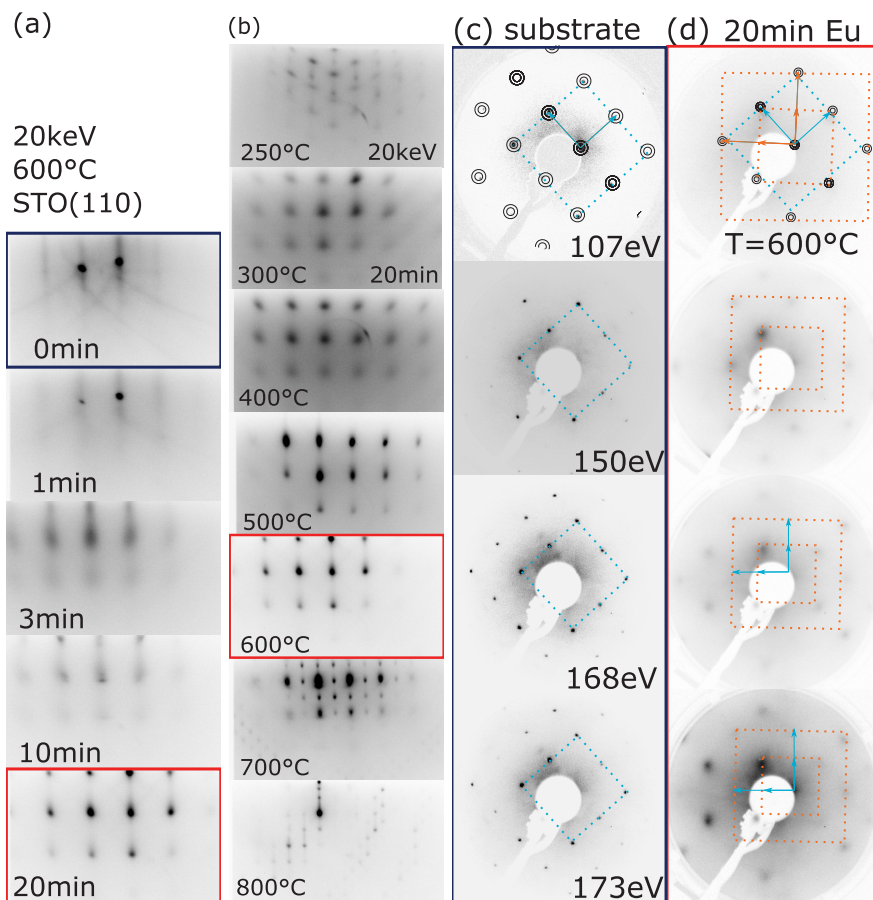


Figure 4.20.: (a) RHEED study of the surface at different time steps at $T_S = 600^\circ\text{C}$. (b) RHEED study varying the growth temperature at $t = 20$ min. LEED study of the substrate (c) at selected electron energies and (d) redox grown EuO film at 600°C for the same energies after $t = 20$ min.

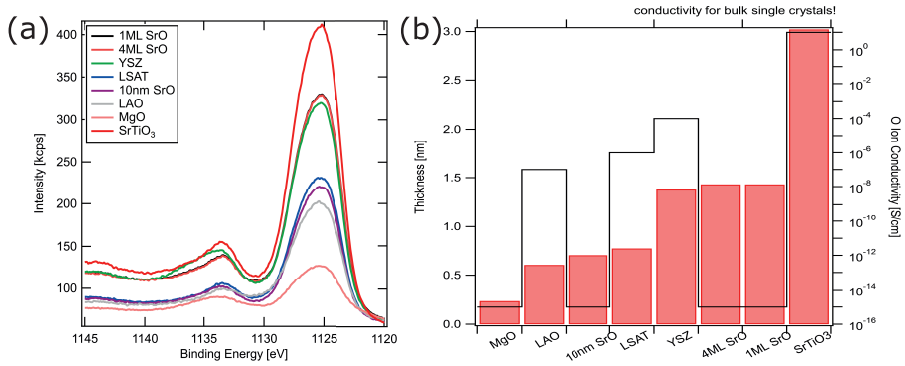


Figure 4.21.: (a) Eu $3d_{5/2}$ core-level spectrum for various oxides. (b) comparison of peak intensity with ionic conductivity of the substrates.

CHAPTER 5

Two-dimensional electron gas

In this chapter we study the interface effects of EuO with two transition metal dichalcogenides SrTiO₃ and BaTiO₃. In both cases we observe a novel state of conductivity at the interface, a two-dimensional electron gas. In the third section we study the EuO/Pt interface, and observe an enhanced T_C , which is in line with a prediction [109]. This can be understood as a first indication, that the second part of the prediction, i.e. the creation of a two-dimensional hole gas (2DHG) could be observed in future experiments as well.

Section 5.1 contains the results which were submitted to Physical Review Materials and were accepted on 28.09.2017 with the following reference: Lömker, P. et al. "Two-dimensional electron system at the magnetically tunable EuO/SrTiO₃ interface". Phys. Rev. Mat. (2017). The preparation of EuO/SrTiO₃ heterostructures and characterization at Jülich was performed by me, I was involved in the synchrotron experiments at CASSIOPEE, performed the data analysis and prepared the experimental and result sections of the document.

5.1. Two-dimensional electron system at the magnetically tunable EuO/SrTiO₃ interface

We create a two-dimensional electron system (2DEG) at the interface between EuO, a ferromagnetic insulator, and SrTiO₃, a transparent non-magnetic insulator considered the bedrock of oxide-based electronics. This is achieved by a controlled *in situ* redox reaction between pure metallic Eu deposited at room temperature on the surface of SrTiO₃ – an innovative bottom-up approach that can be easily generalized to other functional oxides and scaled to applications. Additionally, we find that the resulting EuO capping layer can be tuned from paramagnetic to ferromagnetic, depending on the layer

thickness. These results demonstrate that the simple, novel technique of creating 2DEGs in oxides by deposition of elementary reducing agents [T. C. Rödel *et al.*, Adv. Mater. **28**, 1976 (2016)] can be extended to simultaneously produce an *active*, e.g. magnetic, capping layer enabling the realization and control of additional functionalities in such oxide-based 2DEGs.

Introduction

Two-dimensional electron systems (2DEGs) in functional oxides have gained strong interest as a novel state of matter with fascinating and exotic interface physics. For instance, the 2DEG in LaAlO₃/SrTiO₃ (LAO/STO) interfaces can host metal-to-insulator transitions, superconductivity and magnetism –all of them tunable by gate electric fields [8, 110–117]. The prospect of creating and manipulating a macroscopic magnetic ground state in oxide-based 2DEGs is of enormous interest, as this would pave the route towards oxide spintronic applications with novel quantum phases beyond today’s semiconductor technology.

Recent studies aimed at supporting the existence of magnetic ordering at the LAO/STO interface, e.g. by the observation of tunnel magnetoresistance (TMR) [118] or the inverse Edelstein effect [119, 120]. The magnetic field dependence of TMR was attributed to a Rashba-type spin-orbit coupling, potentially allowing the manipulation of spin polarization in a 2DEG, whereas its spin-momentum locking may enable a high efficiency of the conversion of an injected spin current into a charge current. In fact, in the case of the LAO/STO interface, it was recently demonstrated that additional epitaxial ferroic oxide layers can be used to tune the spin polarization of the 2DEG by an electric field [121] or to control its conduction in a non-volatile manner by ferroelectric switching [122]. So far, the design of functional 2DEG required a single layer growth control of epitaxial LAO onto SrTiO₃. The emergence of interfacial quantum states, such as magnetism, superconductivity or spin-orbit coupling, only sets in at a critical LAO thicknesses of four unit cells and in certain regions of the 2DEG phase diagram [118]. This conundrum was circumvented by the finding that 2DEGs could be fabricated at the bare surface of several oxides, through the creation of oxygen vacancies at their surface [123–129]. These surface 2DEGs can also show magnetic domains [130], thus constituting an appealing alternative for the use and control of electric and magnetic properties of confined states in oxides.

Here, we show that insulating and ferromagnetic EuO can be grown on SrTiO₃ while simultaneously creating a 2DEG at the interface. As schematized in Fig. 5.1, the fabrication of the 2DEG is simply accomplished by the deposition of pure metallic Eu at room temperature in ultrahigh vacuum. We find that the resulting EuO capping layer can be tuned from paramagnetic to ferromagnetic, depending on the Eu metal coverage ($d_{Eu} = 1$ ML and 2 ML, respectively), and show, using angle-resolved photoemission spectroscopy (ARPES), that the integrity of the 2DEG is preserved in both cases, thus providing an ideal knob for tuning the spin-transport properties of the 2DEG.

This bottom-up approach to create a 2DEG by an interfacial redox process relies on recent results demonstrating that the evaporation of an amorphous ultra-thin layer

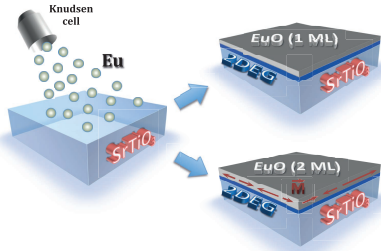


Figure 5.1: Schematics of the experiment. Pure Eu metal (gray balls), evaporated from a Knudsen cell, reacts with the SrTiO₃ surface, forming stoichiometric insulating EuO (gray). The redox reaction locally reduces the SrTiO₃ around its surface, creating a 2DEG (blue). The capping layer can be tuned from paramagnetic, for 1 ML of EuO, to ferromagnetic, for 2 ML of EuO – where magnetic domains with in-plane magnetization \mathbf{M} are represented by the red arrows.

of Al metal on top of an oxide surface generates a homogeneous 2DEG [131]. As the redox reaction between oxides and elementary metals with a large heat of formation of the corresponding metal oxide is a general phenomenon [132], 2DEGs can be created in various oxides, e.g. SrTiO₃, TiO₂, and BaTiO₃ [131]. In the present study, we advance this exciting possibility towards simultaneously creating a 2DEG and forming a *functional* metal oxide over layer –i.e. in a macroscopic ferromagnetic ground state– by choosing a suitable elementary metal (Eu). Our experiments demonstrate how to elegantly link the simplicity and universality of an interfacial redox reaction to obtain increased functionalities by engineering *just one* active oxide over layer that can enhance, modify and allow controlling the properties of the subjacent so-created confined electron system.

Methods

The preparation of ultra-thin EuO films by oxide molecular beam epitaxy (MBE) poses several experimental challenges [14, 44, 78, 82, 133–138]. The oxygen partial pressure, the substrate temperature, and the rate of impinging Eu-metal atoms must be carefully controlled. However, only the stoichiometric compound yields the desired simultaneous occurrence of magnetic and semiconducting behaviors. In this paper a novel method to synthesize ultra-thin EuO is demonstrated and put into practice, *i.e.* a controlled interfacial redox reaction with oxygen provided by the substrate material *only*.

The undoped TiO₂-terminated SrTiO₃ samples are prepared using a well established technique [40]. Atomic force microscopy images show a flat surface with steps of unit cell height and a roughness within one terrace of typically 150 pm and a *c*-direction miscut angle < 0.1°. The samples are then annealed in vacuum to 500 °C for 0.5 h in a MBE chamber at a base pressure of 1.3×10^{-10} mbar prior to Eu evaporation and photoemission experiments. The cleanliness and crystallinity of the so-obtained surfaces are checked by *in situ* X-ray photoemission spectroscopy (XPS). Pure Eu metal is then evaporated at 480 °C at a rate of $0.3 \frac{\text{\AA}}{\text{min}}$ using a low temperature Knudsen cell, while the SrTiO₃ substrate is kept at room temperature. The deposition rate of Eu metal is monitored by a calibrated quartz microbalance.

The redox-created oxidation state of the Eu on the SrTiO₃ surface is analyzed using XPS with Al K _{α} radiation from a SPECS X-Ray anode and a PHOIBOS-100 hemispher-

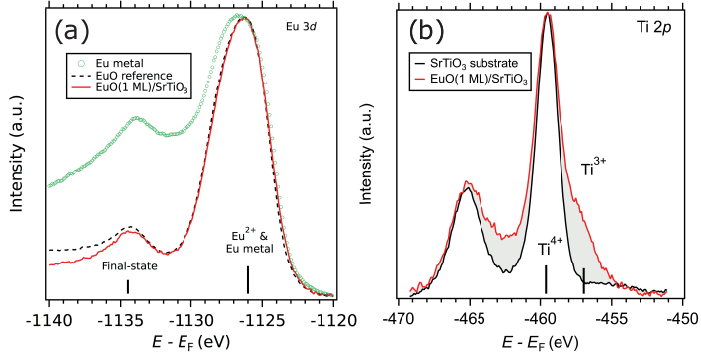


Figure 5.2.: XPS data of (a) the Eu $3d_{5/2}$ peak and (b) the Ti $2p$ core level. Both (a) and (b) illustrate the interfacial redox process after evaporation of pure Eu metal on the surface of SrTiO_3 : oxygen provided from the substrate forms 1ML of stoichiometric EuO , while the Ti of the substrate is reduced to Ti^{3+} .

ical energy analyzer at FZ Jülich. The Eu $3d$ and Ti $2p$ core-levels are analyzed to quantify the oxidation state of the deposited Eu-metal and to observe the redox process with the substrate surface. Before the *ex situ* magnetization measurements, realized with a Quantum Design MPMS SQUID magnetometer, the $\text{EuO}/\text{SrTiO}_3$ samples are further capped with 15 nm of e-beam evaporated MgO to avoid additional oxidation. A hysteresis loop of $H = \pm 1500$ Oe at $T = 5$ K is performed, while temperature dependence is recorded with an aligning field of $H = 500$ Oe for $T = 5$ K to 150 K. All magnetization data was measured in-plane.

The ARPES measurements are conducted at the CASSIOPEÉ beamline of synchrotron SOLEIL. The beamline is equipped with an MBE chamber allowing the *in situ* preparation of the SrTiO_3 surfaces and evaporation of the pure Eu-metal using the same above-specified conditions. We furthermore checked that a surface cleaning using a much faster annealing (about one minute) creates a negligible amount of bulk oxygen vacancies. Eu evaporated hereafter then results in an identical 2DEG, in line with previous reports showing that the electronic structure of the 2DEG at the surface of SrTiO_3 is independent of the material's bulk doping [131]. We used linearly polarized photons at energies of 47 eV and 90 eV, which provide the best cross-section for ARPES spectra on SrTiO_3 [123, 131], and a hemispherical electron analyzer with vertical slits. The angular and energy resolutions were 0.1° and 8 meV. The mean diameter of the incident photon beam was smaller than 100 μm . The samples were measured at $T = 8$ K. The results were reproduced on two samples. All through this paper, we note (hkl) the directions in reciprocal space. The indices h , k , and l correspond to the reciprocal lattice vectors of the cubic unit cell of SrTiO_3 .

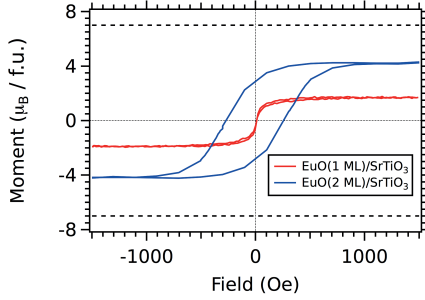


Figure 5.3: In-plane magnetization curves measured at $T = 5$ K, obtained with a Quantum Design MPMS SQUID magnetometer, contrasting the paramagnetic behavior of 1 ML EuO and the low-dimensional ferromagnetic behavior of 2 ML EuO formed after evaporating pure Eu metal on TiO₂ terminated SrTiO₃. The horizontal dashed lines show the expected saturation magnetization at $T = 0$ K for EuO [19, 45].

Results

To show that ultra-thin stoichiometric EuO can be grown without supplying additional oxygen, the films are analyzed using XPS. Fig. 5.2(a) shows the Eu $3d_{5/2}$ core-level. The chemistry of the film can be determined by comparison to reference spectra of Eu-metal, Eu²⁺, and Eu³⁺. The dashed line represents stoichiometric EuO. In accordance with previous studies of the Eu $3d$ core level, the Eu²⁺ valence is located at an energy of -1125 eV [26, 133, 136]. The peak is accompanied by a well known satellite at higher binding energy, which is part of the multiplet of the $3d^9 4f^7$ final state [26]. The red line shows the spectrum of a SrTiO₃ sample with 4 \AA of Eu-metal deposited on top of it. The amount of Eu metal corresponds to a thickness of ≈ 1 ML of EuO. We find that the XPS spectra of our Eu-capped SrTiO₃ samples is indistinguishable from stoichiometric EuO reference data. Features related to Eu-metal or Eu³⁺ are absent. Analogous results are found (not shown) in case of a deposited Eu-metal layer of 8 \AA . This demonstrates that, in the ultrahigh vacuum conditions used here, the Eu metal is oxidized into EuO at the surface of SrTiO₃.

The concomitant substrate reduction is evidenced by the analysis of the Ti $2p$ core level, shown in Fig. 5.2(b). For stoichiometric SrTiO₃ a pure Ti⁴⁺ valence is observed. Upon deposition of nominally 1 ML of EuO, the XPS spectrum shows an additional component at the binding energy of Ti³⁺, indicating that the SrTiO₃ is indeed reduced.

The unique properties of the obtained capping EuO layer, and their tuning with layer thickness, are presented in Fig. 5.3. The measured (not shown) ferromagnetic transition temperature of the 2 ML EuO film was $T \approx 60$ K. At $T = 5$ K, the magnetization versus field $M(H)$ curve of 1 ML of EuO (red curve) shows a paramagnetic behavior. In this case, the effective coordination number of Eu atoms is lower compared to the coordination number in bulk EuO, and thus exchange interactions are weakened [45]. However, at the same temperature, the 2 ML EuO over layer is ferromagnetic (blue curve) with a saturation magnetization of $M_S = 4\mu_B/\text{f.u.}$. The measured saturated magnetic moment for 2 ML of EuO capping is close to the corresponding theoretical values for EuO at $T = 0$ K, represented by the horizontal dashed lines [19, 45, 82, 133]. Now the underlying 2DEG (see next) is interfaced with a magnetic material, which may ultimately enable a control of the spin degrees of freedom in this system.

The formation of oxygen vacancies near the SrTiO₃ surface results in a local electron

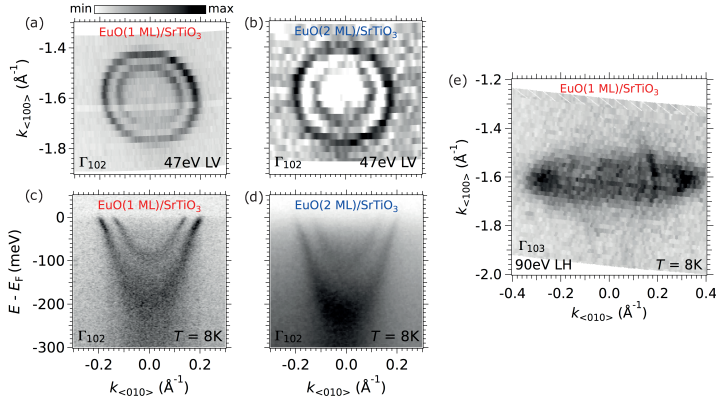


Figure 5.4. ARPES data of the EuO/SrTiO₃ interface. (a, b) Fermi-surfaces taken around the Γ_{102} point of SrTiO₃ for nominally 1 ML (raw data) and 2 ML (negative values of second derivatives) EuO coverage, respectively, using 47 eV photons with linear vertical (LV) light polarization. This combination of photon energy and polarization enhances the photoemission intensity of the $3d_{xy}$ circular Fermi surfaces. (c, d) Corresponding dispersion of the two Ti $3d_{xy}$ light subbands. (e) Fermi-surfaces taken around the Γ_{103} point of SrTiO₃ for 1 ML EuO coverage using 90 eV photons with linear horizontal (LH) light polarization. This combination of photon energy and polarization enhances one of the two orthogonal $3d_{xz/yz}$ ellipsoidal Fermi surfaces. As with our previous results on Al-capped SrTiO₃ [131], we crosschecked that for both 1 ML and 2 ML EuO the 2DEG forms instantaneously after the Eu deposition, and its carrier density is independent of the dose of UV light used to measure the ARPES data. In other words, the 2DEG is entirely due to the oxidation of the capping layer.

doping of the substrate and the creation of a 2DEG. This is induced by the redox reaction with the Eu evaporated on top of it. The results are in analogy with the 2DEGs formed by oxygen vacancies at the UV-irradiated SrTiO₃ surface, Al-capped interface of SrTiO₃ or other oxides [123–126, 128, 131]. This is directly demonstrated by the ARPES data shown in Fig. 5.4. Figs. 5.4(a, b) show the circular Fermi surfaces around Γ_{102} of the two $3d_{xy}$ subbands at the interfaces between 1 ML and 2 ML EuO films on SrTiO₃, respectively. Figs. 5.4(c, d) present the corresponding energy-momentum ARPES intensity maps along the $k_{<010>}$ direction at $k_{<100>} = 2\pi/a$ ($a = 3.905 \text{ \AA}$ is the lattice parameter of SrTiO₃). These correspond to the two Ti $3d_{xy}$ light subbands previously reported for the 2DEG in SrTiO₃ [123, 124, 139]. For the 2DEG at the EuO(1 ML)/SrTiO₃ interface, the band bottoms ($E_0 \approx -200 \text{ meV}$ and -90 meV for the outer and inner subbands, respectively), Fermi momenta ($k_F \approx 0.19 \text{ \AA}^{-1}$ and 0.12 \AA^{-1}), effective masses ($m^*/m_e = 0.7 \pm 0.05$ for both subbands, estimated from a parabolic approximation to the band dispersions, where m_e is the bare electron mass), and the observation of a kink at $E \approx -30 \text{ meV}$ below E_F , ascribed to a band renormalization due to electron-phonon interaction, are all in agreement with previous reports [123, 124,

140, 141]. As shown in Fig. 5.4(e), the ellipsoidal Fermi surfaces, associated with the Ti $3d_{xz/yz}$ heavy subbands, are also observed using horizontal light polarization. From the total area A_F enclosed by *all* the Fermi surfaces, the density of carriers of the 2DEG at the EuO/SrTiO₃ interfaces is $n_{2D} = A_F/(2\pi^2) \approx 2.0 \times 10^{14} \text{ cm}^{-2}$, which is comparable to the density of states of the 2DEG at the bare SrTiO₃ surface [123, 131]. The thickness of the 2DEG can be directly inferred from the number of subbands, their band bottoms and energy separations [123]. Thus, as the electronic structure of the 2DEG at the EuO(1 ML)/SrTiO₃ interface is essentially the same as the one observed at the bare surface of SrTiO₃ [123], or at the Al-capped surface of SrTiO₃ [131], we conclude that its thickness is also the same, namely about 4 – 5 unit cells. ARPES measurements are performed under zero external magnetic field, to guarantee conservation of the photo-emitted electron momentum. Thus, while magnetizing the capping EuO film is not feasible for these measurements, it is nevertheless instructive to compare the ARPES data between the 1 ML and 2 ML EuO films, Figs. 5.4(a, c) and (b, d), respectively. Note that, while the Fermi momenta of the 2DEGs in both systems are essentially identical, one observes a small but distinct difference in their bandwidths and band splittings. Specifically, in the case of the 2 ML EuO film, the bottoms of the Ti $3d_{xy}$ light subbands are at about -230 meV and -100 meV , with a concomitant band splitting ($\approx 130 \text{ meV}$) slightly larger than the one in the 1 ML EuO film ($\approx 100 \text{ meV}$). Additionally, both the Fermi edge at $E = 0$ and the kink at $E \approx -30 \text{ meV}$ appear much less pronounced in the 2DEG at the EuO(2 ML)/SrTiO₃ interface. The possible link between such differences in electronic structure, and the ferromagnetism (with or without domains) in the 2 ML EuO film, should be further explored in future works.

On the other hand, an important conclusion at this point is that the onset of ferromagnetism in the zero-field-cooled 2 ML EuO films, with the concomitant formation of randomly oriented ferromagnetic domains (as schematized in Fig. 5.1), still preserves the integrity of the underlying 2DEG. Together with the magnetization data from Fig. 5.3, our results open the very exciting perspective of enabling the continuous tuning, under external applied field, of the spin transport properties in oxide-based 2DEG.

Conclusions

In summary, we demonstrated that the deposition in vacuum, at room temperature, of Eu-metal on SrTiO₃ results in the simultaneous creation of a 2DEG in the oxide substrate and a capping EuO layer that can be tuned from paramagnetic (1 ML thickness) to ferromagnetic (2 ML). These results open new perspectives for investigating the interaction of the magnetic and electronic properties of the 2DEG in SrTiO₃. More generally, these results lay a new ground for the simple and versatile design of all-oxide devices in which the functionalities of the constituting elements, and their mutual coupling, can be obtained from controlled physicochemical reactions and vacancy engineering at their interfaces.

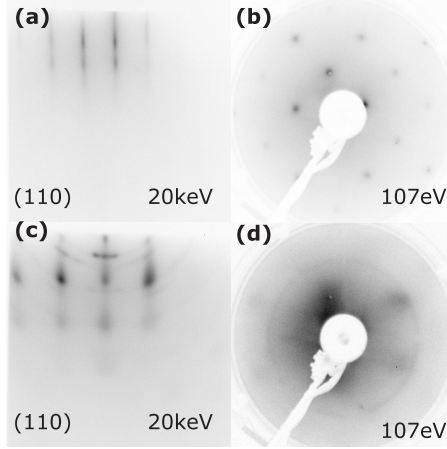


Figure 5.5.: (a) RHEED of BaTiO₃ virtual substrate and of (c) EuO/BaTiO₃. We find that the substrate exhibits RHEED streaks, indicating a small degree of misorientation, while EuO exhibits a transmission pattern which is indicative for an island growth mode. (b) LEED of the BaTiO₃ virtual substrate and of (d) EuO/BaTiO₃. The substrate LEED reflexes exhibit a square pattern, as expected for the lattice of BaTiO₃, while for EuO/BaTiO₃ the pattern is blurred.

5.2. Towards multiferroic two-dimensional electron gases: EuO/BaTiO₃

The results of a magnetically tunable 2DEG at the EuO/SrTiO₃ interface (see [Section 5.1](#)) may be explored in future transport realizing the transport properties of a magnetically gated 2DEG. We propose to extend this idea to a 2DEG with ferromagnetic and ferroelectric properties, i.e. a potentially multiferroic hybrid.

A previous study has shown, that the Al/BaTiO₃ interface can produce a ferroelectrically gated 2DEG. It was concluded that a route towards ferroelectric resistance switching could be paved in this way [131]. We transfer this knowledge and replace Al with Eu forming again EuO by a controlled interface reduction of the BaTiO₃ substrate. Thereby a ferromagnetically gated 2DEG at the interface with a ferroelectric material maybe created.

Indeed, the EuO/BaTiO₃ interface has already been studied with a different goal [142]. Here, the authors studied the magnetic behavior of thick EuO films, grown at high temperature using the adsorption limited growth mode, as a function of the direction of the ferroelectric polarization. The ferroelectric polarization introduces surface charges at the EuO/BaTiO₃ interface, whereby an electron doping is achieved. This effect enhances the next-nearest neighbor interaction J_1 of EuO and thereby allows a control of the magnetic properties by switching the ferroelectric polarization [142].

In this regard, we propose to study the interface by a new method: A Eu/BaTiO₃ interface focusing on the interfacial redox reaction and the concomitant creation of a 2DEG. The possibility to combine ferroelectricity, ferromagnetism and an interfacial 2DEG is an interesting prospect as this would pave the way towards a multiferroic device.

Preparation of BaTiO₃ virtual substrates

BaTiO₃ virtual substrates are prepared by depositing 32 nm of BaTiO₃ on TiO₂ terminated SrTiO₃ (001) substrates. BaTiO₃ is evaporated by PLD, using a similar chamber as for the ITO preparation (see Section 4.5), the preparation is done by Willi Zander and Jürgen Schubert (PGL, Forschungszentrum Jülich), whose support we thankfully acknowledge. The BaTiO₃/SrTiO₃ system is well suited for epitaxial growth, as the room temperature lattice constant of BaTiO₃ $a_{BaTiO_3} = 4.01 \text{ \AA}$ is similar to that of SrTiO₃ $a_{SrTiO_3} = 3.905 \text{ \AA}$. The deposition is performed at $T_S = 750 \text{ }^\circ\text{C}$ with an oxygen back pressure produced by supplying a constant flux of $j_{O_2} = 30 \frac{\text{mL}}{\text{min}}$. The laser is operated at $f = 10 \text{ Hz}$ for $t = 20 \text{ s}$ resulting in $d = 32 \text{ nm}$ thick films [92].

The growth process is validated with XRD, where a rocking curve width of $\sigma < 0.3^\circ$ is obtained, confirming the highly oriented crystalline integration of BaTiO₃/SrTiO₃.

We study the structure of the BaTiO₃ virtual substrate *in situ* with RHEED and LEED in Figure 5.5 (a) and (b). The RHEED pattern indicates a small degree of misorientations in the film by the presence of RHEED streaks. LEED shows a square pattern that is in line with the symmetry of the substrate without any reconstructions. Adding a 5 nm layer of EuO ($a_{EuO} = 5.14 \text{ \AA}$) on this BaTiO₃ virtual substrate a transmission pattern in RHEED (c) is observed, which indicates island growth. The LEED pattern in (d) shows blurred reflections indicating a rather disordered EuO film. We argue, that the unordered state of the EuO film is due to a large tensile strain between EuO and BaTiO₃. The crystal direction of BaTiO₃ along (110) provides the smallest mismatch with the EuO lattice of $\approx 10\%$.

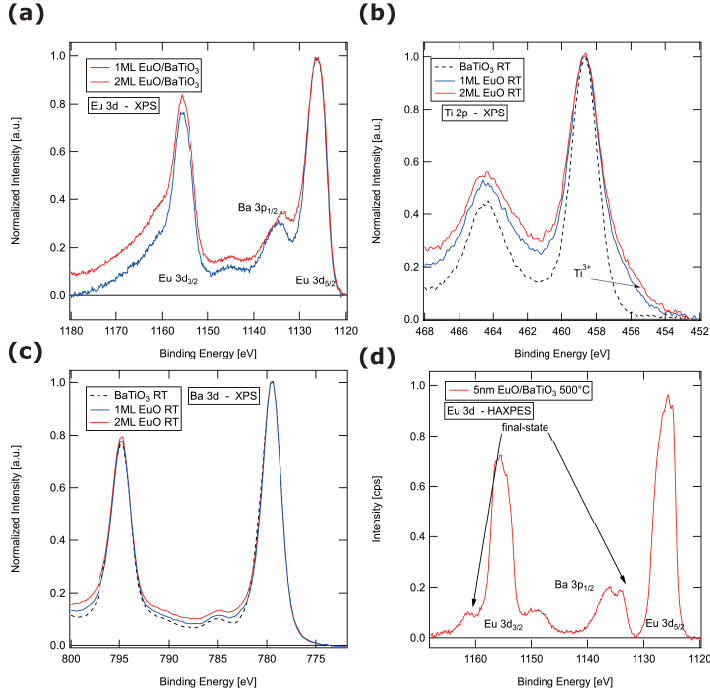


Figure 5.6.: In (a) (b) and (c) we show the Eu 3*d*, Ti 2*p* and Ba 3*d* core-levels of a BaTiO₃ virtual substrate and for 1ML and 2ML EuO/BaTiO₃ samples grown at room temperature. We obtain the Eu 3*d* core-level spectrum for a 5nm sample in (d) using HAXPES to obtain bulk-sensitivity. The spectrum shows the characteristic shape of EuO, confirming a successful oxygen free preparation of EuO/BaTiO₃.

Chemical properties of the EuO/BaTiO₃ interface

In Figure 5.6 we compare photoemission data of four different sample configurations: the bare BaTiO₃ virtual substrate, 1ML and 2ML thick EuO over layers grown at RT and a sample grown at $T_S = 500$ °C, for which we again use the substrate supplied oxygen to oxidize the Eu metal.

In (a) we show the XPS data of the Eu 3*d* core-level. All of the presented spectra are normalized to unity on the lowest binding energy peak. First, it is observed, that the Ba 3*p*_{1/2} core-level peak lies directly at the binding energy of the trivalent Eu atom's 3*d*_{5/2} core-level. Due to this fact we also show the Eu 3*d*_{3/2} core-level to enable a comparison, as only features present in both core-levels can be attributed to the chemical composition of EuO. We find no indication of trivalent Eu peak at the Eu 3*d*_{3/2}.

A quantitative fit would allow to determine the chemical composition of the EuO films. However, due to the different inelastic background and the presence of overlaying

core-levels the method developed in Section 4.3 cannot be applied.

For $d_{\text{EuO}} = 1\text{ML}$ no indication of Eu metal is found in the spectrum. This is different for the 2ML case, where a clear peak asymmetry is observed, as would be expected for metal rich EuO_{1-x} . This shows, that the redox reaction of Eu on BaTiO₃ is limited to a thickness of approximately 1ML at room temperature.

The crystal structure of BaTiO₃ is very similar to SrTiO₃— along the (001) direction a layered structure of TiO₂ and BaO planes is expected. In Figure 5.6 (b) the XPS Ti $2p$ spectrum for the BaTiO₃ virtual substrate shows a TiO₂-like spectrum. Upon deposition of 1ML of EuO, spectral weight at $E_B = 458\text{ eV}$ is introduced, indicating the reduction of the surface to Ti₂O₃, as was the case for SrTiO₃ [143]. The spectral weight of this feature increases upon depositing a second ML of EuO. However, the difference is quite small, indicating that the interfacial redox process is limited to a EuO thickness between 1ML and 2ML.

In Figure 5.6 (c), the Ba $3d$ XPS spectrum is depicted. The spectra for substrate and EuO covered samples are very similar indicating no change in the valency of the BaO layers in the BaTiO₃ virtual substrate. We attribute the enhanced spectral intensity between the peaks to the variation in the inelastic background signal from lower E_B peaks or Eu Auger excitations.

Finally, a sample is prepared at high temperatures to evaluate the applicability of the redox growth approach developed in Section 4.7. The chemical composition of a $d_{\text{EuO}} 5\text{ nm}$ ($t = 10\text{ min}$) sample grown at $T_S = 500\text{ }^\circ\text{C}$ is analyzed with HAXPES to access the bulk properties of this thicker film. For this *ex situ* experiment we cap the sample with 12 nm of MgO and the experiment is performed at P09/PETRA III with $h\nu = 6000\text{ eV}$. The spectrum has been modified by the subtraction of a linear background. Again the Ba $2p_{1/2}$ peak is observed directly in the region of trivalent Eu $3d_{5/2}$. The absence of trivalent Eu is observed and thereby we can show that stoichiometric EuO grows on BaTiO₃ at $T_S = 500\text{ }^\circ\text{C}$. The spectral weight at 1134 eV and 1162 eV is associated with the final-state multiplet satellite as reported in the literature [26].

We find that 1ML of Eu reacts with the surface and creates EuO while reducing TiO₂ to Ti₂O₃ - by contrast the Ba spectra are virtually unchanged, indicating that it does not react with Eu metal. We find that RT deposition leads to the same redox process as was found for the Eu/SrTiO₃ interface. Adding a second mono-layer we detect some metallic Eu in the spectrum. The Ti³⁺ intensity increases only little between 1 ML and 2 ML. Additionally feasibility of oxygen free growth of EuO/BaTiO₃ is studied using the redox growth mode also at $T_S = 500\text{ }^\circ\text{C}$.

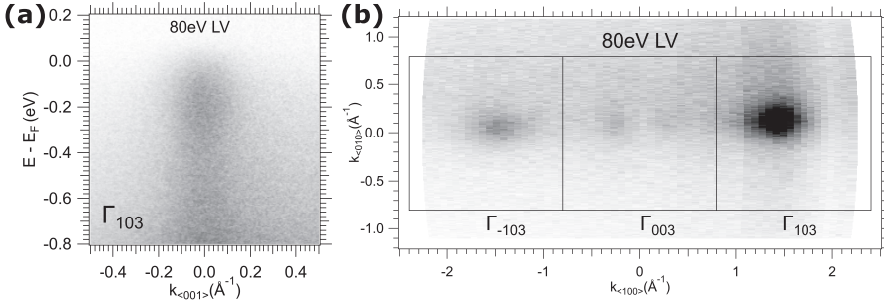


Figure 5.7.: (a) $E(k)$ map for a 1ML EuO/BaTiO₃ sample. In the center a strong peak of spectral weight is observed in accordance with previous reports in the literature [131]. (b) In plane Fermi-surface map of the third Brillouin-zone showing the heavy t_{2g} -like Ti $3d^1$ states at the Fermi energy. This behavior is associated with electron pockets forming in the material at E_F . The black squares represent the zone edges of the Brillouin zones.

Electrical structure of 1ML EuO/BaTiO₃

In order to evaluate the electronic structure of the EuO/BaTiO₃ interface, we perform again ARPES measurements ($E_\gamma = 80\text{eV}$) using linear vertical polarized photons at CASSIOPEE, Synchrotron Soleil. For this experiment BaTiO₃ virtual substrates are prepared in France as reported in [131]. The substrates are annealed at 500 °C for 2 h after a cooling down to room temperature Eu is deposited. Using a quartz micro balance to measure the evaporation rate, we deposit 1ML of Eu at a rate of $0.005 \frac{\text{Å}}{\text{s}}$ using 99.9% pure Eu metal. Afterwards the EuO/BaTiO₃ heterostructure is directly transferred to the ARPES chamber.

In Figure 5.7, we present results of the ARPES measurements on 1ML EuO/BaTiO₃ obtained at $T = 8\text{K}$. In (a) $E(k)$ map at Γ_{103} is shown. Immediately after irradiation we observe a stable spectrum with a strong intensity at the central region at $E \leq E_F$. As synchrotron radiation is known to reduce the surface of transition metal dichalcogenides over time, the immediate observation of this feature leads to the conclusion, that our observation is caused by the growth of the EuO overlayer and not by the beam damage [123]. The observed feature has already been analyzed in literature and is associated with the heavy t_{2g} states of Ti $3d^1$ [139]. Due to the presence of spectral weight at the Fermi-level it is shown, that itinerant carriers have been released at the interface. This feature is associated with the heavy band of d_{xz}/yz like feature as observed at the SrTiO₃ interface.¹

We obtain the Fermi-surface map of the first three Brillouin zones of $l = 3$ integrated over $\Delta E = 20\text{meV}$ using 80 eV linear vertical polarized photons. The carrier concentration of the itinerant carriers can be estimated by the area of all the Fermi surfaces by

¹ As we do not observe a dispersing feature, ARPES experiments in the future should be performed in the future using LH light at the same Brillouin zone to complete the study.

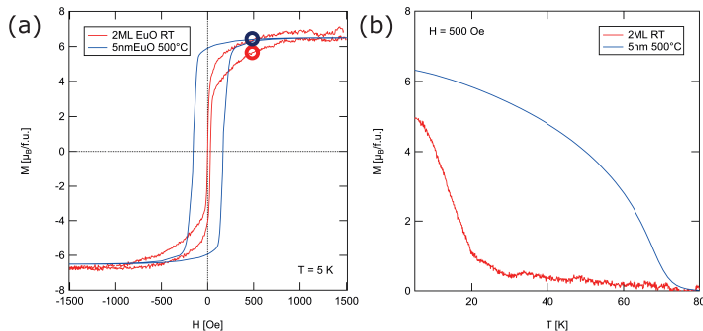


Figure 5.8.: (a) $M(H)$ curve of a 2ML ($T_S = \text{RT}$) and 5 nm ($T_S = 500^\circ\text{C}$) thick EuO layer on BaTiO₃. Both preparations lead to a ferromagnetic response with sizable magnetic moments of $M_S > 6 \mu_B/\text{f.u.}$ (b) $M(T)$ curve of the same samples. The ordering temperature is significantly reduced for the 2ML sample due to finite size effects and island growth [144]. The thick film displays a bulk-like $M_S = 6.3 \mu_B/\text{f.u.}$ as well as a bulk-like $T_C = 70 \text{ K}$

$$n_{2D} = \frac{A_F}{2\pi^2} = \frac{\pi \cdot \left(0.15 \frac{1}{\text{\AA}}\right)^2}{2\pi^2} \approx 3.5 \times 10^{13} \frac{1}{\text{cm}^2}. \quad (5.1)$$

As we measure only the Fermi surface with LV polarization, this calculation is only an estimation and the total number of electrons is larger than n_{2D} . Yet, with this evidence of a redox created 2DEG is provided at the EuO/BaTiO₃ interface.

Magnetic properties of EuO/BaTiO₃ heterostructures

The magnetic properties of ultra thin EuO/BaTiO₃ heterostructures (see Figure 5.8) are analyzed using the magnetometers described in Section 3.5. We present data for a 2ML EuO/BaTiO₃ grown at RT and a 5 nm thick sample grown at $T_S = 500^\circ\text{C}$ in Figure 5.8 (a). The low temperature sample exhibits a ferromagnetic (see Figure 5.8(a)) response with a magnetic moment of $M_S \approx 6 \mu_B/\text{f.u.}$. The small coercivity of this sample shows, that most likely monodomain islands of EuO have formed. These islands interact superparamagnetically with each other and we identify this as the cause for the small coercivity. As expected for ultra-thin films, we observe in Figure 5.8 (b) a severely reduced ordering temperature of $T_O = 20 \text{ K}$. Moreover, the $M(T)$ curve shows a different shape from the expected Brillouin function. Again this behavior is attributed to the presence superparamagnetic EuO islands and final size effects [19].²

The $d = 5 \text{ nm}$ sample exhibits the behavior expected for a closed ferromagnetic EuO film. An almost bulk like saturation magnetization of $M_S = 6.3 \mu_B/\text{f.u.}$ and a Curie

² Due to choosing $H = 500 \text{ Oe}$ for the aligning field in the $M(T)$ curve, the magnetic moment in the 2ML case is reduced to $5 \mu_B/\text{f.u.}$.

Temperature of $T_C = 70$ K are observed.³

To conclude a magnetic over layer is produced for room temperature deposition of $d_{\text{EuO}} = 2\text{ML}$ on BaTiO_3 virtual substrates, simultaneously a 2DEG is created at the ferromagnet/ferroelectric interface. This enables the preparation of a ferromagnetically and ferroelectrically gated 2DEGs in an all oxide heterostructure..

Furthermore it is shown at $T_S = 500^\circ\text{C}$, that the oxygen-free preparation of EuO on BaTiO_3 is possible at conditions similar to those found in [Section 4.6](#) demonstrating again the universality of the proposed growth method.

³ Thickness of the film is estimated from Eu flux as described in [Section 4.1](#) and is expected to be lower, due to a non-unity sticking coefficient of Eu/ SrTiO_3 .

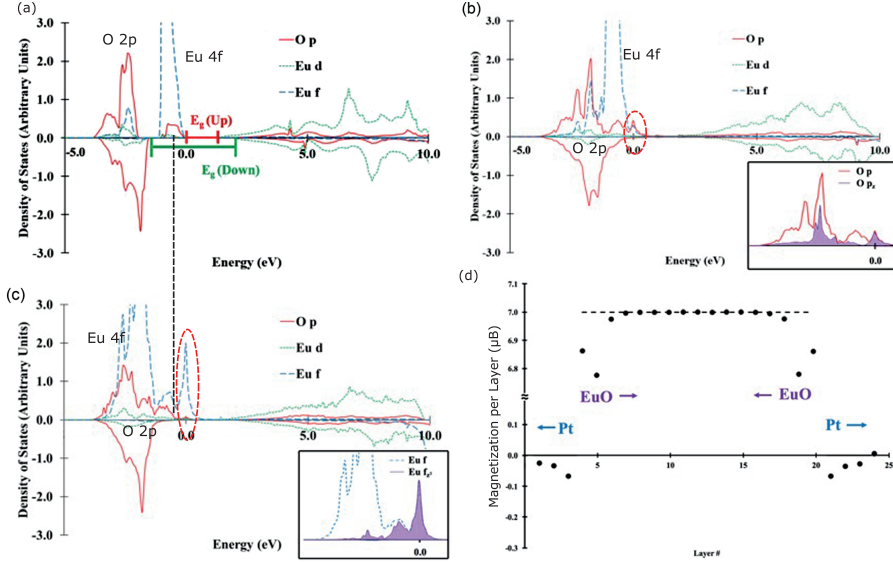


Figure 5.9.: Spin dependent projected density of states for the valence band of bulk EuO (a), and the first (b) and second (c) EuO layer at the EuO/Pt interface. In (b) and (c) enhanced hybridization of Eu 4*f* and O 2*p* bands is observed. Also a significant density of states is observed at E_F contrary to the expected insulating behavior of bulk EuO. (d) Magnetization as a function of the layer, showing a reduced magnetization of EuO at the interface while a small magnetic moment is induced into Pt. Shown in red is the density of states for Eu 4*f* at E_F and the black line denotes the peak location of bulk Eu 4*f*. Taken from [109].

5.3. First indication of a two-dimensional hole gas at the Pt/EuO interface

In the following a study of the interface between a ferromagnetic insulator and Pt is presented. This interface is of interest due to a variety of effects, like spin pumping or spin-hall magnetoresistance experiments.

Earlier studies of $\text{EuO}_{1-x}/\text{Pt}$ have found a reduced magnetic moment at the interface for EuO [73]. This finding motivated a DFT modeling of the interface [109]. As shown by Figure 5.9 (d), the theoretical study predicts that the magnetic moment of EuO is slightly reduced at the Pt interface. This reduced moment is accompanied by an induced moment into the interfacial Pt. Another prediction of this publication is the occurrence of a two-dimensional hole gas (2DHG) in EuO at this interface, as is shown in Figure 5.9 (a-c). The authors argue that this behavior is caused by the charge transfer between Pt and EuO. At the same time, the hybridization between Eu 4*f* states and O 2*p* states is

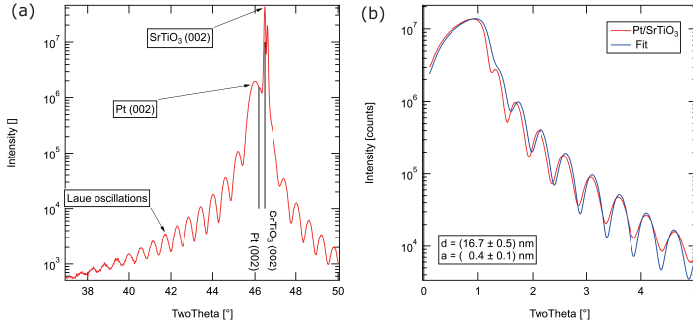


Figure 5.10.: (a) XRD of Pt/SrTiO₃ virtual substrate. Both the SrTiO₃ and Pt (002) reflexes are observed. (b) XRR of a Pt/SrTiO₃ virtual substrate. The roughness of $a = 0.4$ nm indicates a layer by layer growth mode.

enhanced as shown in Figure 5.9(a-c). Since this hybridization increases the overlap of the wave functions, an increased exchange interaction $J_{interface} > J_{bulk}$ is expected. As shown in Subsection 2.1.2, an increased $J_{interface}$ is expected to cause a higher T_C for the interfacial regions of EuO, compared to the bulk.⁴

This perspective motivates our study of the EuO/Pt interface, in particular the growth of EuO on Pt and the interface magneto-electronic structure, which is studied using MCD-HAXPES and magnetometry.

Preparation of Pt virtual substrates

First Pt virtual substrates are prepared by depositing Pt metal onto TiO₂-terminated SrTiO₃ by magnetron sputtering. This is performed *ex situ* at the Helmholtz Nano Facility at FZ Jülich. The substrate is annealed in vacuum for $t = 30$ min at $T_S = 900$ °C in UHV with a base pressure of $p_{base} = 2 \times 10^{-10}$ mbar. We deposit Pt (purity 99.99%) at a rate of $0.4 \frac{\text{Å}}{\text{s}}$ for a total thickness of $d = 20$ nm using a reported synthesis at $T_S = 700$ °C [145]. The deposition is performed in a background pressure with Ar gas of $p = 1 \times 10^{-2}$ mbar.

The heteroepitaxial growth of Pt on SrTiO₃ is possible, as the lattice parameter of both the substrate $a_{\text{SrTiO}_3} = 3.905$ Å and film $a_{\text{Pt}} = 3.923$ Å are close to each other, with only 0.45% compressive strain.

The free energy γ of the substrate, interface and film determine the growth mode. A layer by layer growth is expected when

$$\gamma_{\text{substrate}} > \gamma_{\text{interface}} + \gamma_{\text{film}}. \quad (5.2)$$

For the case of EuO/Pt, the inequality is almost an equality $2.42 \text{ J/m}^2 \approx 2.49 \text{ J/m}^2$

⁴ The reduced T_C found in [73] was observed for EuO_{1-x}, which has an enhanced $T_C = 125$ K in the bulk. Therefore, an increase of $T_{C,\text{EuO}} < 125$ K would be observed as a reduced T_C for bulk EuO_{1-x}.

Component	γ [J/m^2]
EuO	0.49
TiO ₂ terminated SrTiO ₃	1.30-2.06
Pt	2.42
EuO/Pt	2.00

Table 5.1.: Surface and interface free energies γ for the relevant components of EuO deposition on BaTiO₃ virtual substrates from TiO₂-terminated SrTiO₃.

for the substrate, interface and film contributions taken from the reported values for SrTiO₃, EuO, Pt and the EuO/Pt interface (shown in Table 5.1). From this it can be expected that the growth of a closed film is just possible for EuO/Pt, while the opposite is very unlikely [109].

For the case of Pt/SrTiO₃ the free energies indicate that Pt does not wet SrTiO₃ as $\gamma_{SrTiO_3} < \gamma_{Pt}$, even without adding the free energy of the Pt/SrTiO₃ interface. However, successful preparations of closed films of Pt(001)/SrTiO₃ (001) have been reported in the literature [146].

The structure of the prepared Pt/SrTiO₃ films is analyzed using XRD and XRR as depicted in Figure 5.10. Displayed in part (a) of the figure are the Pt and SrTiO₃ (002) XRD peaks and the SrTiO₃ substrate reflex is used to obtain a calibration for the absolute $2\theta = 46.523^\circ$ [13]. An out of plane lattice parameter for Pt $a_{oop} = 3.943\text{\AA}$ is obtained. This is slightly larger than the expectation of $a_{Pt} = 3.927\text{\AA}$. The in-plane component can be calculated via the Poisson ratio of Pt to $a_{ip} = 3.87\text{\AA}$. We find that Pt films of this thickness (see XRR below) grow compressively strained with 1.2% with respect to the SrTiO₃ lattice. The error of the measurement is estimated by the relative width of the Pt peak and amounts to $\sigma_{2\theta}/(2\theta) = 0.8\%$.

The oscillations in the XRD spectrum are Laue oscillations indicating a low roughness in the film. The spacing of the the Laue oscillations can be used to obtain a thickness estimate [59], which yields $d_{Laue} = 16.4\text{ nm}$. This is confirmed by a XRR scan depicted in Figure 5.10 (b). A good fit to the spectrum is obtained using a Pt thickness of $d = 16.7\text{ nm}$, in agreement with d_{Laue} , and a low roughness of $a = 0.4\text{ nm}$ for the Pt surface. The roughness along the Pt/SrTiO₃ interface is $a_{int} = 0.1\text{ nm}$. This shows, that the heteroepitaxial relationship of Pt(001)/SrTiO₃ (001) is achieved and flat films are obtained by our virtual substrate preparation.

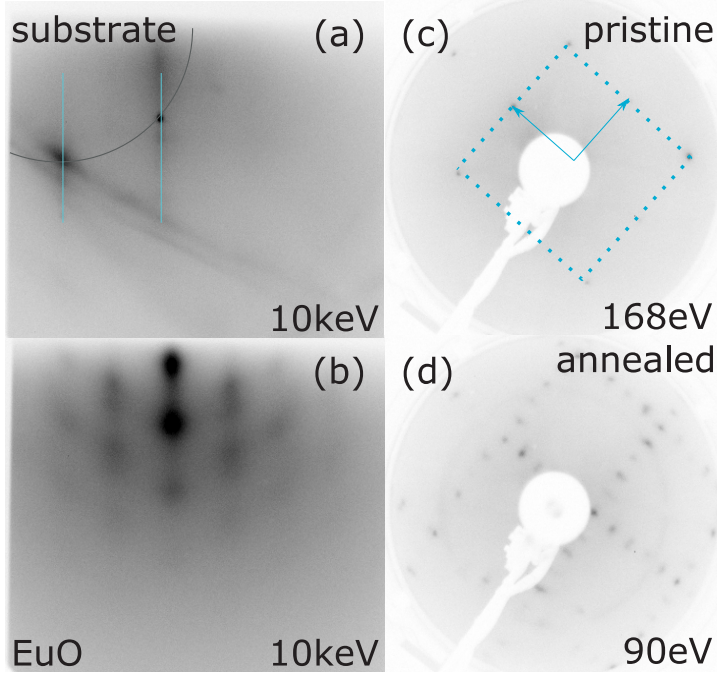


Figure 5.11.: (a) RHEED of an annealed Pt/SrTiO₃ virtual substrate at $E_{kin} = 10$ keV. The Laue circle and RHEED streaks are indicated in the image. (b) RHEED of a 5 nm EuO/Pt film, indicating crystalline and island growth. (c) LEED of the as introduced Pt/SrTiO₃ surface. (d) LEED of the same substrate after annealing, exhibiting a pattern resembling the surface reconstruction of bulk Pt crystals [52].

Figure 5.11 (a) shows a RHEED image of the Pt virtual substrate along the (110) direction ($E_{kin} = 10$ keV). This RHEED pattern was obtained directly after the film was introduced into the MBE system. RHEED spots on the Laue circle and RHEED streaks are observed simultaneously indicating a crystalline integration of Pt/SrTiO₃ with a layer-by-layer growth mode.

After preparation in the sputter chamber, the film is exposed to air and we measure the "as introduced" Pt/SrTiO₃ film with LEED in Figure 5.11 (b). We observe a square lattice without any reconstruction on the surface. After annealing for $t = 1$ h at $T_S = 600$ °C is performed, a surface reconstruction is observed. The (1x1) square reconstructed into the superposition of a (5x1) and (1x5) pattern, which is indicated by the 4 additional LEED spots connecting the (1x1) square.

By comparison with the literature, we identify this surface state as the surface reconstruction observed for bulk single crystalline Pt, which has recently been studied using SPA-LEED [52]. The study concludes that a hexagonal centered $c(26 \times 118)$ structure

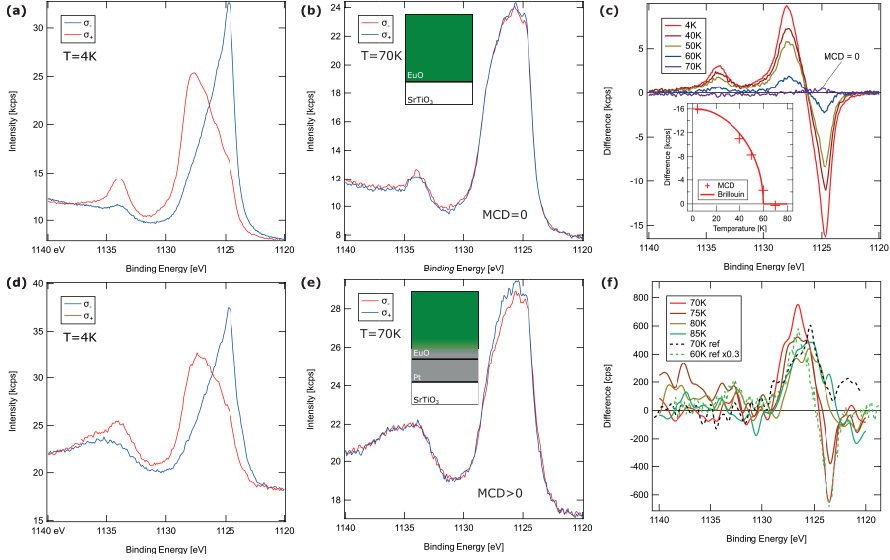


Figure 5.12.: (a) and (d) show the Eu $3d_{5/2}$ spectra as a function of the polarization σ^{\pm} for sample *a*) and *b*) respectively at $T_{diode} = 4$ K. Both spectra show a strong magnetic contrast. In (d) there is a broad peak at $E_B \approx 1135$ eV indicating a small degree of over oxidized Eu_2O_3 , which we understand simultaneously as the absence of metallic EuO_{1-x} ! (b) and (e) show the same spectrum for the case of $T_{diode} = 70$ K. In sample *a*) MCD is absent, while a clear MCD signal is observed for sample *b*). (c) and (f) both show the resulting MCD spectra. Inset in (c): temperature dependence of the MCD intensity and a Brillouin fit with $T_C = 60$ K. In (f) a MCD signal is measured up to $T_{diode} = 80$ K far above the magnetic transition of sample *a*).

is observed for the reconstructed bulk Pt surface. This agrees with the observed pattern to the degree of accuracy due to the two different methods. We conclude, that the reconstruction of a bulk-like Pt film is observed for our Pt virtual substrates which can enable high quality EuO growth.⁵

EuO/Pt interface: Enhanced magnetic interaction

In order to investigate the magnetic coupling between Pt and EuO, we prepare two samples: Sample *a*) is a redox grown EuO sample at $T_S = 500^\circ\text{C}$ for $t = 20$ min on SrTiO_3 with an approximate thickness of $d = 15$ nm (see Section 4.6). Sample *b*) is

⁵ The observation of the bulk Pt surface reconstruction actually is a quality criterion of the Pt virtual substrate preparation. The apparent contradiction to the XRD findings of a strained film is alleviated by the fact, that XRD was performed before the in vacuo annealing step and XRD is sensitive to the complete film of $d = 16.7$ nm, while LEED observes only the surface.

a EuO/Pt heterostructure grown at the same temperature with an oxygen pressure p_{O_2} . The temperature is measured using a pyrometer with $\epsilon = 0.10$ in accordance with reported emissivity factors for Pt (from the pyrometer manual).

For the EuO/Pt growth, an adsorption limited growth mode is utilized, reducing the oxygen partial pressure below the stoichiometric value to $p_{\text{O}_2} = 1.2 \times 10^{-8}$ Torr ($R = 0.75$). The EuO film is studied with RHEED as depicted in [Figure 5.11](#) (b). We observe RHEED streaks together with a transmission pattern indicating an island type growth mode of EuO/Pt. This behavior is interpreted by the strain of the Pt film, which is on the order of the strain induced by SrTiO₃, for which we found the same behavior (see [Section 4.6](#)). Both samples are capped with 12 nm of MgO prior to exposure to air.

HAX-MCD experiments are performed at P09, PETRA III as described in [Subsection 3.6.1](#). The goal of the experiment is to measure the element selective magnetic properties of both samples as a function of temperature. At the cryostat the temperature diode is mounted on the cold-finger, which leads to a significant deviation between the measured and real temperature at the sample location. In order to improve the precision we use the well known behavior of $M(T)$ for sample *a*) as a temperature reference.

XMCD spectra of the Eu $3d_{5/2}$ core-level are obtained at $T_{\text{diode}} = 4$ K, 50 K, 60 K and 70 K. The absence of an XMCD signal is defined as $T_{\text{real}} > 69$ K. The XMCD signal is defined as the difference between spectra obtained using left and right circularly polarized light as:

$$\text{XMCD} = \sigma^+ - \sigma^- \quad (5.3)$$

where σ^\pm is the spectrum of the light polarized at small and large diffraction angle of the transmission crystal polarizator. This choice leads to the appropriate sign convention in the MCD spectra. The spectra are first corrected for the varying transmission of the polarizator, and then the difference spectrum is calculated. The conventional method of displaying the asymmetry is deliberately not applied, as the background correction can introduce small unwanted features in the spectra. This would be unproblematic for the strong asymmetry of the Eu $3d_{5/2}$ peaks at $T = 4$ K. However, this measurement is aimed at detecting the small moments expected at $T \approx T_C$, where small intensity changes are in the range of the measured signal.

In [Figure 5.12](#) (a) and (d) we compare spectra of sample *a*) and *b*) at $T_{\text{diode}} = 4$ K and in (b) and (c) for $T_{\text{diode}} = 70$ K. At low temperature, spectra with similar shape are observed for both samples, i.e. MCD is observed in both samples. At elevated temperature sample *a*) shows the absence of MCD, while sample *b*) still shows a MCD. [Figure 5.12](#) (c) depicts the XMCD signal from sample *a*) as a function of T . The inset of the same figure shows a Brillouin function fit to the maximum of the XMCD intensity. We obtain a good fit with $T_{C,\text{meas}} = 60$ K indicating, that the deviation is $\Delta T = T_{C,\text{bulk}} - T_{C,\text{meas}} = 9$ K at this temperature.

We present the XMCD for sample *b*) in (f) of the same figure. Dashed lines indicate comparison curves from sample *a*) to enable an identification of MCD. We observe significant MCD for $T = 70$ K, 75 K and 80 K, 20 K above the expected value of T_C for bulk EuO. Thereby we find, that the Pt induces a higher transition temperature in the EuO film, in line with the prediction in the literature [[109](#)].

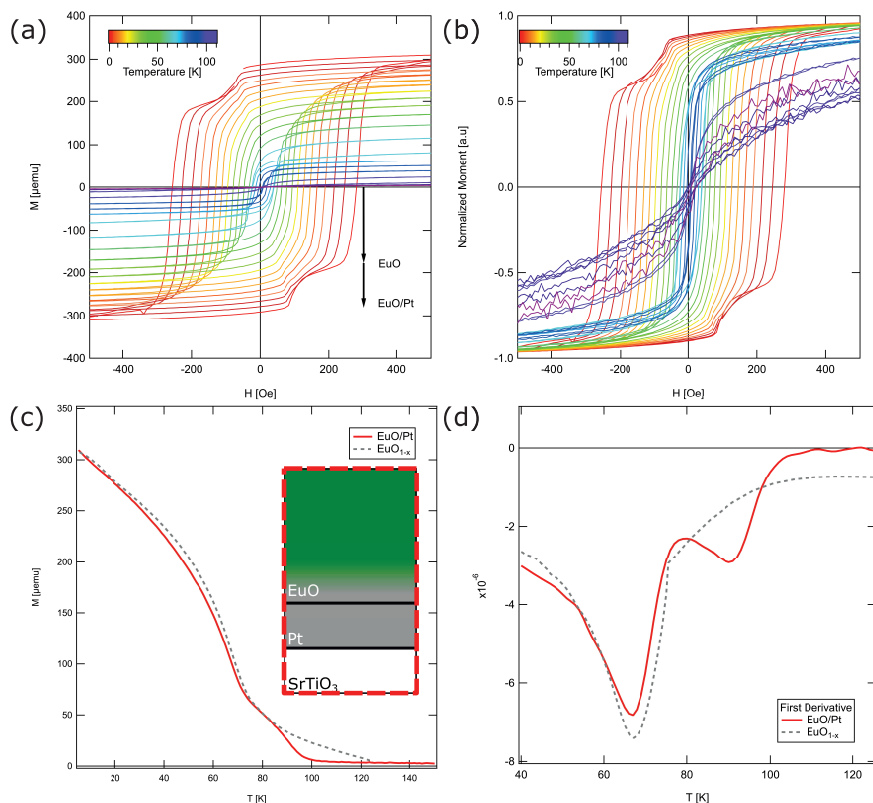


Figure 5.13.: (a) $M(H)$ curve for a 5 nm EuO/Pt sample as a function of temperature. A two-coercivity system is observed. (b) Normalized $M(H)$ curve of the same sample. The EuO/Pt magnetic feature disappears at a temperature of $T_B \approx 30$ K. (c) $M(T)$ curve of a stoichiometric EuO/Pt interface and a metal-rich film of EuO_{1-x}. We observe two transitions $T_{C,1} = 67$ K and $T_{C,2} = 90$ K for EuO/Pt and only a gradual decrease for EuO_{1-x}. (d) First derivative of the $M(T)$ curves illustrating the difference between EuO_{1-x} and Pt/EuO. The first shows only one peak at T_C while the latter shows the expected two peaks.

In order to cross-check the temperature calibration from the MCD-HAXPES measurements and to advance the analysis, sample *b*) is measured with VSM. We perform a $M(H)$ measurement in 5 K steps in the range 5 K to 110 K. The results of this $M(H, T)$ measurement are shown in [Figure 5.13](#). We observe a system with two magnetic phases where the coercive field is $H_C = 90$ Oe and 280 Oe for $T = 5$ K. This feature is not observed for $T > 30$ K. In view of the island type growth mode of the EuO/Pt interface we interpret this behavior as a superposition of the magnetic signal of superparamagnetic particles at the EuO/Pt interface and a ferromagnetic (EuO bulk) phase. The blocking temperature of the superparamagnet is $T_B = 30$ K (as the blocking temperature is a function of t the measurement time, we specify: $T_B(10\text{ s})$).

The temperature behavior of film is depicted in [Figure 5.13](#) (c). The $M(T)$ of EuO/Pt can be described as a superposition of a two ferromagnetic phase system with different T_C . In order to exclude the possibility of Eu metal⁶ we compare the EuO/Pt film with a EuO_{1-x} sample. The EuO_{1-x} sample shows only one transition at T_C and a slowly decaying magnetic tail at $T > T_C$. We calculate the temperature derivative of $\frac{\partial M}{\partial T}$ as shown in [Figure 5.13](#) (d). We observe two peaks for the EuO/Pt interface at $T = 67$ K and 90 K, which can be identified as the magnetic transition temperature [147]. In the case of metallic EuO only one peak is detected at the bulk T_C . Therefore, we conclude, that an under stoichiometric EuO_{1-x} film exhibits a different magnetic behavior than the prepared sample *b*) and that the enhanced T_C can not be due to the EuO film alone. This underscores our assumption that the EuO/Pt leads to an interfacial enhancement of J and causes the observed enhanced T_C .

In conclusion, a successful integration of Pt on SrTiO₃ was demonstrated. These virtual substrates are used for EuO deposition, where two independent techniques show the enhanced magnetic ordering temperature for the EuO/Pt interface. The so prepared system behaves like a magnetic two coercivity system consisting of a superparamagnetic interfacial EuO/Pt layer coupled to the ferromagnetic bulk EuO. This supports the predictions for the EuO/Pt in the literature and motivates the study of EuO/Pt interfaces with regard to the proposed interfacial 2DHG [109].

⁶ Which already was absent in our HAXPES measurements in [Figure 5.12](#) (e).

CHAPTER 6

Room temperature magnetism of EuO

The ferromagnetic properties of EuO are strong, as the magnetization is $M_S = 7 \mu_B/\text{f.u.}$, however they are limited to low temperatures ($T_C = 69 \text{ K}$), as was shown in [Section 4.6](#). From a technological point of view, this is even below the temperature of liquid nitrogen. This shifts the area of interest to fundamental studies, e.g. for use of EuO with regard to spin filter functionality (see [Subsection 2.1.3](#)). Therefore, approaches enhancing the T_C are currently under investigation.

6.1. Co/EuO interfacial magnetism

In our approach to enhance the ordering temperature of EuO we look into interface effects with a room temperature $3d$ ferromagnet.

Literature review for T_C enhancement of EuO

Several routes with the aim of increasing T_C have been attempted: One prominent approach is the doping of EuO with Eu metal or Gd metal. The result is an increased $T_C \approx 125 \text{ K}$, while introducing conductivity to the EuO layer at the same time. Thereby the tunnel-barrier functionality is disabled [\[58\]](#). A second approach is choosing substrates with compressive strain on the EuO film. Here, it is expected, that the shorter distances between nearest and next-nearest neighbors increase the wave function overlap and enhance the exchange coupling strengths J_1 and J_2 (introduced in [Subsection 2.1.2](#)). An enhanced exchange coupling would lead to a higher T_C . However, to date no experiment has succeeded to introduce ferromagnetism up to room temperature in stoichiometric EuO films.

The preparation of EuS/Co multi-layers has been published recently in the literature [\[148\]](#). EuS is also a ferromagnetic insulator, like EuO, however, it has a lower T_C of 16 K . It often replaces EuO since it is stable in atmosphere and the preparation is

less demanding. In Ref [148], the authors observe by HAX-MCD the Eu L edge and report ferromagnetic properties up to room temperature. By comparison, EuS reveals a smaller conduction band split $2\Delta E_{ex} = 0.2$ eV, whereas for EuO $2\Delta E_{ex} = 0.6$ eV. The exchange splitting is the origin of the spin filter effect and therefore is an important parameter of a spin filter junction. Due to the experimental challenge in synthesis of EuO this experiment, as presented in [148], has not been performed with EuO even though improved spin filtering can be expected.

For a successful application of a material as a spin filter tunneling barrier, the spin polarization P should be as high as possible – ideally 100%. EuO films as thin as 15 Å are predicted to exhibit $P = 98\%$ [11]. Due to this fact the ferromagnetic properties of EuO need not be present in bulk EuO. Instead, interfacial phenomena like the magnetic proximity effect could be a candidate to induce a magnetic moments into EuO thin films at room temperature.

Another study has used Fe/EuO films and studied the magnetic properties of these granular films [149]. They provide indirect evidence for an interfacial coupling between Fe and EuO by a non saturating magnetization at $T = 5$ K, while the saturation at $T = 300$ K is reached for $H < 2$ kOe. However, no direct evidence is provided that there is an exchange interaction between EuO and Fe.

In this regard, the magnetic interfacial interaction of the $3d$ ferromagnet Co is studied as a function of the EuO thickness in a Co/EuO heterostructure. The element specific magnetic properties of this prototypical metal/ferromagnetic insulator system is evaluated using X-ray absorption spectroscopy magnetic circular dichroism (XMCD) at I10 at diamond light source.

We transfer the growth parameters as shown in Section 4.6 to prepare Co/EuO interfaces and perform XMCD at the Co/EuO interface to study the element selective magnetic properties of the $3d/4f$ interface.

6.1.1. Sum rules and exchange interaction length

In this section we explain how the sum rules are used to quantify the XMCD spectra. These rules are applied commonly to $3d$ ferromagnets such as Fe, Ni and Co to analyze their $L_{3,2}$ edge dichroism. However, they can be applied for $4f$ ferromagnets as well and have been tested on rare earth materials [150] and for the $M_{5,4}$ edge of europium oxide [151]. Applied to the $M_{5,4}$ transition the equations for the orbital moment m_{Orb} and spin moment m_{Spin} are [152, 153]

$$m_{Orb} = -2\frac{q}{r}N_h \quad (6.1)$$

$$m_{Spin} = \frac{5p - 3q}{r}N_H(1 + \langle T_Z \rangle)^{-1} \quad (6.2)$$

$$p = \int_{M_5} (\sigma^+ - \sigma^-) d\omega \quad q = \int_{M_{5,4}} (\sigma^+ - \sigma^-) d\omega \quad (6.3)$$

$$r = \int_{M_{54}} I_{XAS} d\omega \quad (6.4)$$

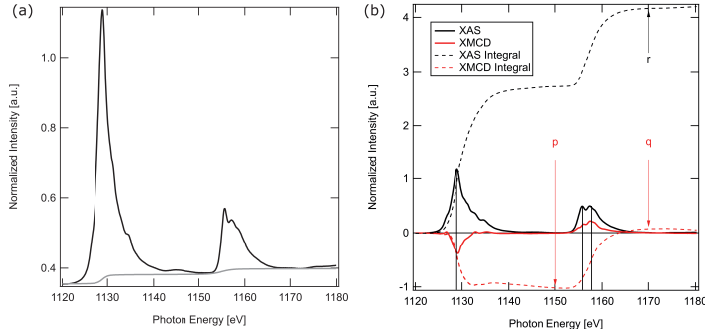


Figure 6.1: (a) XAS spectrum of a EuO reference sample recorded at $T = 10$ K with background fit to remove additional states above the $M_{5,4}$ edge. This spectrum is free from Eu_2O_3 and Eu states [151]. (b) Sum rule analysis of the same spectrum after background correction. Shown are the XAS and XMCD spectrum and the integral values for p , q and r .

where N_H denotes the number of holes per formula unit. Due to EuO's electron configuration of Eu $4f^7$, the number of holes per formula unit is $N_H = 7$. m_{Orb} and m_{Spin} are obtained in units of $\mu_B/\text{f.u.}$. p and q are integrals over the XMCD spectrum for the M_5 and the $M_{5,4}$ region, respectively, as shown in Figure 6.1 (b). The XMCD spectrum is defined as the difference between absorption spectra recorded with left and right circularly polarized light σ^\pm . The convention is to define the sign such that negative XMCD values are measured on the Co L_3 edge, see Subsection 2.3.5. The integral over the XAS spectrum, r is defined as

$$\int_{M_{5,4}} I_{XAS} d\omega = \frac{3}{2} \int_{M_{5,4}} (\sigma^+ + \sigma^-) d\omega. \quad (6.5)$$

m_{Spin} contains components spectral weight of transitions caused by the magnetic dipole operator $\langle T_z \rangle$. However, as EuO has a half filled $4f^7$ shell, the angular quantum number $l = 0$, which implies $\langle T_z \rangle = 0$ [150].

In order to evaluate Equation 6.4, the area under an unpolarized XAS spectrum is needed, as shown in the reference spectrum in Figure 6.1 (a). This integral is proportional to the $4f$ valence states per formula unit of the investigated EuO film. For photon energies larger than the M_5 and M_4 edges, transitions into higher final states are allowed. These contribute to the XAS spectrum as a continuum and cause the characteristic "jump" in the spectra. Consequently, these jumps have to be removed from the spectrum, in order to obtain the correct value for r . This is achieved by subtracting two broadened step edges from the spectrum as a background treatment at the peak location of the M_5 and M_4 edges, respectively. The height of these steps is set according to the branching ratio (see Section 2.3) of the M edge to be $3/5$ ($2/5$) for the M_5 (M_4) edge.

We perform this background subtraction using the Unifit 2016 software. The shape

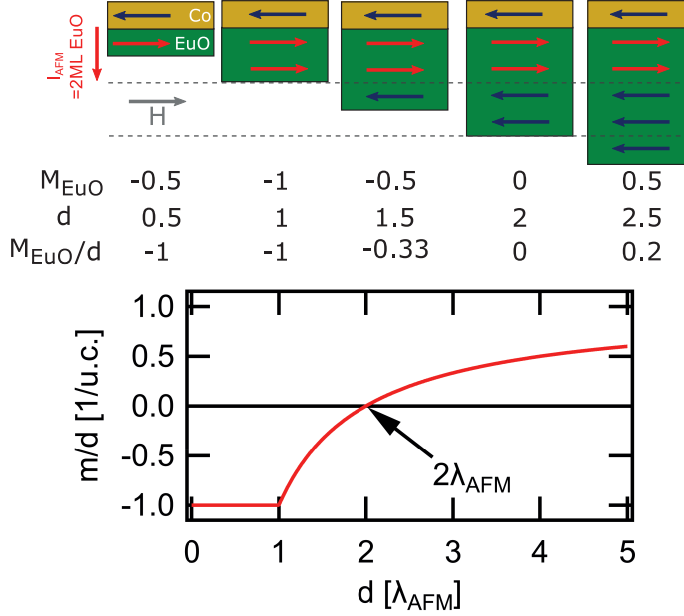


Figure 6.2.: Sketch of a model for the exchange coupling length at the interface of Co/EuO. The bottom shows the scaling behavior of the reduced coordinates m/d , which represents the average magnetic moment m of the stack per unit cell. This property is also available by applying the sum rules as described in the text. The magnetic compensation of ferromagnetically and antiferromagnetically coupled EuO, $m/d = 0$, is located at $d = 2\lambda_{AFM}$.

of the background function is a superposition of the error- and the arctangent function broadened by 2 eV. This peak shape is an appropriate treatment as the error function is the integral of a Gaussian peak shape and the arctangent function is the integral of a Lorentzian peak shape. Due to the continuum excitation into higher final states, the background takes the shape of the integrals of convoluted Gaussian and Lorentzian peak shapes.

Figure 6.1 (a) shows the resulting spectrum with the background correction, while in (b) the integral values p , q and r indicated.

In the following the XMCD spectra of Co/EuO heterostructures on TiO₂-terminated SrTiO₃ are studied with the sum rules while varying the EuO film thicknesses.

Model for the interface exchange length

We determine three parameters describing the coupling between EuO and Co: the ferromagnetic properties of the EuO over layer, the antiferromagnetic coupling length λ_{AFM} and a gauge for the energy of the exchange interaction $E_{ex}^{\text{EuO-Co}}$.

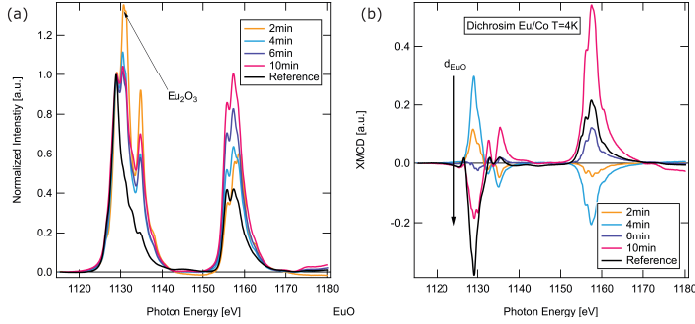


Figure 6.3.: (a) XAS spectrum of the Eu $M_{5,4}$ edge for varying EuO thickness. Comparing to the black reference EuO, we find, that all Co/EuO heterostructures exhibit a certain fraction of Eu_2O_3 . (b) XMCD spectra of the same structures for deposition times $t = 2$ min-10 min. First the EuO is antiferromagnetically coupled to the Co film - as seen by comparison with the black reference XMCD for EuO. For thicker films, the XMCD intensity increases and a ferromagnetic behavior is observed for $t > 6$ min. A sign change at $t = 6$ min is observed.

In order to determine the coupling length λ_{AFM} we develop a linear model for the average magnetization of the film as a function of the EuO over layer thickness d_{EuO} . The model is schematically shown in Figure 6.2. We model the interaction length of the antiferromagnetic interaction with an "all-or-nothing" law, as we expect the interaction to be present only in proximity to the Co interface. For $d_{\text{EuO}} < \lambda_{AFM}$, all EuO layers exhibit a reversed magnetic moment $-m_{\text{EuO},i}$, for the unit cell i . For $d_{\text{EuO}} > \lambda_{AFM}$ the ferromagnetic bulk behavior of EuO is assumed and $m_{\text{EuO},i}$ points in the direction of the external field. This results in the following magnetization model

$$M_{\text{EuO}}(d_{\text{EuO}}) = \sum_i m_{\text{EuO},i}, \quad m_{\text{EuO},i} = \begin{cases} -m_{\text{EuO}} & d_{\text{EuO}} < \lambda_{AFM} \\ m_{\text{EuO}} & d_{\text{EuO}} > \lambda_{AFM} \end{cases} \quad (6.6)$$

As we obtain the average magnetic moment per formula unit of the whole film from the sum rules, this equation is transferred into reduced coordinates m/d , where m is the reduced magnetization and d the reduced thickness. The behavior is displayed in the bottom part of Figure 6.2. The reduced coordinates are chosen such that $M = 1$ represents the bulk magnetic moment per unit cell of EuO. From this model we obtain a sign change of m at $2\lambda_{AFM}$.

6.1.2. XAS-MCD results

In this section, we evaluate the element selective magnetic properties measured by XAS at BLADE beamline, Diamond Light Source. First, we describe the prepared heterostructures, then the experiment is described. We finally describe XMCD measurements at

t [min]	2	4	6	10
d_{EuO} [nm]	2.6	4.7	6.4	8.9

Table 6.1.: EuO thickness as a function of deposition time t at $T_S = 500^\circ\text{C}$

fixed aligning field of $H = 500$ Oe and hysteresis data for $H = \pm 14$ T, the measurement temperature is $T = 4$ K if not noted otherwise.

We record the Eu $M_{5,4}$ and for Co the $L_{3,2}$ edges by X-ray fluorescence XAS with left and right circularly polarized light.

Shown in [Figure 6.3](#) are (a) the XAS spectra and (b) the XMCD spectra for a varying d_{EuO} . The XAS spectra reveal a significant over-oxidation of the EuO films for the Co/EuO heterostructures, while the EuO reference film only shows EuO components. Comparing this with the XMCD signal, we find that only the EuO related fractions exhibit a significant XMCD and the Eu_2O_3 parts show no XMCD as is expected.

The over-oxidation of the films is attributed to a rough Co over layer, which lead to an insufficient capping. Due to this the XAS integral r is constant, as it is a measure for the available Eu transitions. However, p and q are smaller, as the fraction of EuO is reduced. Therefore, the sum rule analysis on mixed valency films leads to lower values for m_{orb} and m_{spin} for over-oxidized films.

[Figure 6.3](#) (b) depicts the XMCD spectra of a thickness series of EuO films. See [Table 6.1](#) for $d_{\text{EuO}}(t)$. For a reference EuO film without cobalt we obtain a negative XMCD signal (black line), as expected for the XMCD sign convention. Co/EuO heterostructures show an antiferromagnetic coupling of EuO to the Co over layer, observed by the positive XMCD signal at the M_5 edge for small d_{EuO} . The Co thickness of $d = 4$ nm is thick enough to be the pinning layer, as we find, that in all our experiments the Co layer exhibits a ferromagnetic behavior. The XMCD signal is inverted for $d_{\text{EuO}} < 6.4$ nm, indicating as expected that the antiferromagnetic coupling between Co and EuO is an interface effect.

Applying the sum rules to the measured spectra, we obtain the thickness-dependent magnetic moment per formula unit shown in [Figure 6.4](#). As expected from the model developed in the previous section, the thin EuO films show a negative m_{Spin} indicating the antiferromagnetic coupling of EuO to the Co layer. The magnetic moment increases towards the bulk value of the EuO reference with increasing thickness. For m_{Orb} , we find small contributions $m_{Orb} < 1 \mu_B/\text{f.u.}$ – in line with the expectation of $l = 0$ from the $4f^7$ configuration of EuO. The presence of a non-zero m_{Orb} can not be excluded and could indicate an induced orbital moment from the Co over layer, because Co has a non-zero m_{Orb} , as can be seen by its electron configuration with $l = 3/2$.

Fitting m_{Spin} with the previously developed model, we obtain a good fit using the obtained m_{Spin}^{ref} from the reference EuO film and $2\lambda_{AFM} = (5.6 \pm 1.4)$ nm in this way, we determine the exchange length for the antiferromagnetic coupling between Co/EuO. The value of λ shows that this effect is not limited to the interface only, as $\lambda \approx 6 \mu\text{c}$ EuO.

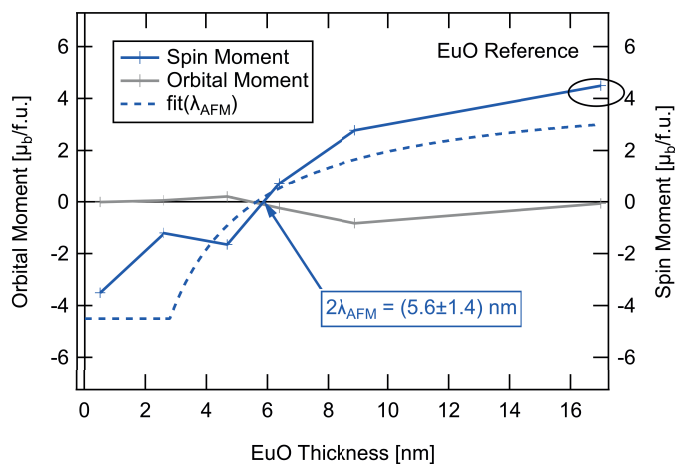


Figure 6.4.: Thickness-dependent magnetic moment of the Co/EuO heterostructure obtained by applying the $3d-4f$ sum rules to the XMCD spectra. We observe a negative magnetic moment for the thin EuO films confirming the antiferromagnetic ordering at the interface of Co and EuO. Fitting the spectra with the model for the exchange length λ_{AFM} we obtain $2\lambda = (5.6 \pm 1.4)$ nm. Measured at 5 K.

XAS Hysteresis at 4 K and 300 K

Having established the presence of an antiferromagnetic coupling and the exchange length λ_{AFM} at low temperatures, hysteresis loops of Co/EuO at $T = 4$ K and 300 K are compared. At $T = 4$ K the Co layer, the Co/EuO interface and the bulk of EuO are ferromagnetic. By contrast, at room temperature bulk EuO has no ferromagnetic properties and we expect only an XMCD signal from Co and the Co/EuO interface. Two hysteresis loops at $T = 4$ K and 300 K are shown in Figure 6.5 (a) and (c).

At low temperature, EuO and Co show a similar field response. The Co/EuO interface is opposed by the ferromagnetic interaction in the bulk of EuO. Due to this the antiferromagnetic orientation of the magnetization of EuO at the Co interface is restricted to small fields as shown in (b). The antiferromagnetic region is in the range between 1800 Oe and -1100 Oe. The hysteresis loops are recorded in between 14 T and -14 T and only the branch of decreasing field is depicted, due to limited time in the experiments. Also for time reasons, the hysteresis loops are obtained using the intensity at 4 energies, the pre-edge and on edge energy for Eu M_5 and Co L_3 respectively. Due to this we can measure only a , the asymmetry

$$a = (I(E_{on}) - I(E_{pre})) / (I(E_{on}) + I(E_{pre})) \quad (6.7)$$

where $I(E_{on})$ is the intensity of the edge and $I(E_{pre})$ is the intensity in the pre-edge region. As the L_3 edge for Co and the M_5 edge are recorded, $a < 0$ values indicate $m > 0$,

in accordance with the XMCD sign convention. Consequently, in the region shown in (b) EuO has a positive asymmetry (negative m) while Co shows the opposite behavior.

In Figure 6.5 (c) a hysteresis at $T = 300$ K is presented. At these temperatures far above the $T_C = 69$ K of bulk EuO, no magnetic moment is expected for bulk EuO. Yet, a sizable EuO XMCD signal is detected. This indicates, that the exchange mechanism between EuO and Co leads to an induced magnetic moment of EuO at room temperature. Only above high fields of $H_C > (7.22 \pm 0.58)$ T the EuO magnetization reverse.

The Zeeman energy, is the energy required to "flip a spin", in the sense, that it resembles the potential energy of a magnetized body in an external magnetic field. We use the Zeeman energy in order to evaluate the magnetic coupling strength between EuO and Co at the switching field H_C

$$E_{exch} \approx E_{Zeeman} = 7\mu_B \cdot (7.2 \pm 0.6) \text{ T} = (2.90 \pm 0.23) \text{ meV} \quad (6.8)$$

where, E_{exch} denotes the exchange energy and E_{Zeeman} the Zeeman energy for the seven unpaired electrons in the Eu $4f$ valence level. An estimate for the exchange coupling strength is obtained by using $J = E_{exch}/2S_{\text{EuO}}S_{\text{Co}} \approx 0.278 \text{ meV}$ [151], where S denotes the spin configuration of the respective material. This is a large value for J , as the reported values for the exchange interaction strength in bulk EuO is $J_1 = 0.052 \text{ meV}$ [18]. Therefore, we report a strong interface interaction between Co/EuO which induces magnetic moments even at room temperature.

By the Bloch law it can be shown that the Curie temperature scales proportionally with J [154] as:

$$M(T) = M_S \left[1 - \frac{\alpha}{S} \left(\frac{k_B T}{2JS} \right)^{3/2} \right] \Leftrightarrow T_C \propto J \Rightarrow T_C/T_{bulk} = J/J_{bulk} \approx 5 \quad (6.9)$$

where M is the magnetization at temperature T , M_S is the saturation magnetization, S is the number of spins, k_B is the Boltzmann constant, T_C is the Curie temperature and J is the exchange interaction strength. As seen by solving for $M(T_C) = 0$, the Curie temperature depends directly on J and therefore it is to be expected, that the enhanced J of Co/EuO is the cause for the significant increase of T_C to values above room-temperature.

In comparison, the study of a multi-layer Co/EuS system has reported a switching field $H_C \approx 4$ T indicating, that the interface effect is stronger for the Co/EuO case.

Concluding, the XMCD effect was used to study the Co/EuO interface. The sum rules for the $3d$ - $4f$ transition have been applied enabling a quantitative description of the magnetic properties and a determination of the exchange interaction length $2\lambda_{AFM} = (5.6 \pm 1.4) \text{ nm}$ (about 5ML). The hysteresis curves obtained at 4 K and at 300 K show a strong interfacial interaction between Co/EuO leading to the observation of a room temperature magnetism of the EuO film due to the strong exchange with the $3d$ ferromagnet Co. The result of equation 6.9 indicates an interfacial $T_C \approx 350$ K.

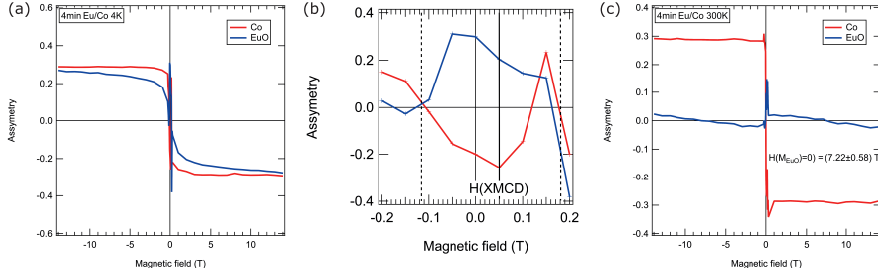


Figure 6.5: (a) Hysteresis of the $d_{\text{EuO}} = 4.9$ nm Co/EuO heterostructure at $T = 4$ K. Only one branch from $H_0 = 14$ T to $H_1 = -14$ T is measured. Plotted is the asymmetry of the Co L_3 and Eu M_5 edge respectively. For high fields, both show a similar scaling behavior. (b) Zoom into $H = \pm 0.2$ Oe, where the antiferromagnetic region can be identified. (c) Hysteresis for Co/EuO at room temperature. Magnetic behavior of the EuO film is observed well above the expected $T_C = 69$ K, indicating a sizable magnetic response of EuO at room temperature. Again, EuO and Co show an antiferromagnetic coupling.

6.2. Room temperature magnetism in ultra-thin Co/EuO interfaces

In a further XMCD experiment a Co/EuO heterostructure is analyzed with $d_{\text{EuO}} = 2$ ML. Instead, of using the high temperature redox process the sample is kept at $T = 300$ K and a low evaporation rate of $r = 0.005 \frac{\text{\AA}}{\text{s}}$ is used. As we show in Section 5.1, this preparation leads to a two dimensional electron gas (2DEG) at the EuO/SrTiO₃ interface. At a thickness of 2ML sizable magnetic properties are observed, which are again restricted to low temperatures of only $T_C \approx 60$ K. In this section the results of adding a Co interface on top of a 2DEG EuO/SrTiO₃ heterostructure are presented.

Figure 6.6 (a) and (b) show the XAS and XMCD spectra of that specimen at $T = 300$ K. In Figure 6.6 (a) the treated spectrum for a sum rule analysis is presented. In Figure 6.6 (b) we compare spectrum of the same heterostructure at $T = 4$ K with $T = 300$ K. We again observe a sizable XMCD signal in both cases. In contrast to the limited T_C of bulk EuO, this indicates a magnetization at room temperature. The sign of the XMCD signal is, as for all thin Co/EuO interfaces, opposite to the expectation for ferromagnetic EuO. Applying the sum rules, we find that this spectrum resembles a spectrum with $-1 \mu_B/\text{f.u.}$ – about 16% of the expected magnetization of bulk EuO.

In conclusion we have identified the Co top-layer the cause for room temperature magnetism in ultra thin EuO thin films. In this way we have successfully utilized a room temperature synthesis for a EuO ultra thin film $d_{\text{EuO}} = 2$ ML with ferromagnetic properties at $T = 4$ K and at room temperature.

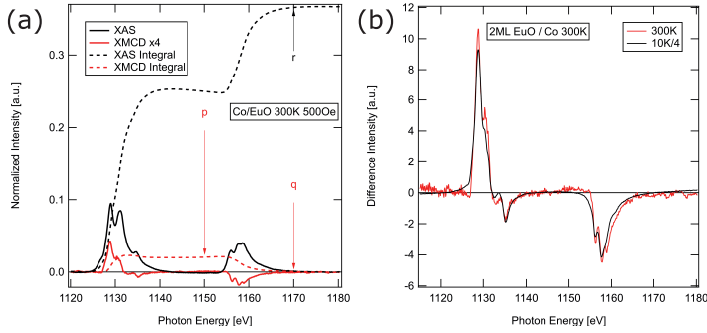


Figure 6.6.: (a) background corrected XAS Eu $M_{5,4}$ spectrum and XMCD with sum rule related integrals p , q and r . (b) XMCD spectrum from Co/2ML EuO at $T = 4$ K and 300 K. Both spectra have a similar shape indicating a similar magnetic properties and a sizable magnetization of $m_{Spin}(300\text{ K}) = 1 \mu_B/f.u.$

6.3. Magnetic proximity effect: Origin of the antiferromagnetic Co/EuO exchange interaction?

The magnetic proximity effect refers to the development of new properties arising due to the proximity of two or more dissimilar materials with different long range ordering [155]. This effect has been identified as the cause of enhanced magnetic properties of a thin layer of a magnetic material A in proximity to a different magnetic layer B. The systems range from non-magnet/ferromagnet (A/B) heterostructures such as Pd/Fe, where Pd showed magnetic behavior [156], to antiferromagnet/ferromagnet systems like $Co_3O_4/Ni_{80}Fe_{20}$ systems. The high T_C of the latter increased the Neél temperature T_N of the first significantly [157]. Also an enhanced T_C of diluted magnetic semiconductors (Ga,Mn)As(100) in contact with Fe was observed [158].

The diluted magnetic semiconductors in particular are a material class which have comparable properties as the ferromagnetic insulator EuO. Both have a small energy gap $E_G = 1.2$ eV (1.4 eV [159]) for EuO ((Ga,Mn)As) and high magnetic moments of $7 \mu_B$ per Eu ($5 \mu_B$ per Mn). By contrast, the Mn concentration is on the order of a few percent and therefore only small degrees of spin-polarization can be observed when using this diluted material.

The (Ga,Mn)As(100)/Fe system was studied with XMCD. At the Fe interface the Mn ions show an antiferromagnetic behavior [158] which decays over the period of $d = 7$ ML, restricting the effect to the interface, in line with our findings in the previous section. The study uses available predictions of the antiferromagnetic exchange between Fe and Mn to explain this behavior, due to the magnetic proximity effect [160]. For the Co/EuO system these calculations do not exist yet and therefore a theoretical foundation needs to be developed in the future.

CHAPTER 7

Conclusion and Outlook

The ferromagnetic insulator EuO has been studied for various interface configurations with oxides and metals and in confined electron systems.

We synthesize EuO on SrTiO₃ (001) and other oxides using a novel approach, the redox reaction with the substrate. For this we develop a quantitative XPS fitting routine on the basis of a set of Eu 3*d* reference spectra. The redox growth is possible for $T_S = 300^\circ\text{C}$ - 600°C , where we detect stoichiometric EuO except for a small interfacial region. The growth rate was evaluated and we find a Mott-Cabrera like growth limited by ionic oxygen conductivity of the substrate. The crystal structure is analyzed and epitaxial integration of EuO(110)/SrTiO₃ (100) and EuO(001)/SrTiO₃ (001) is obtained. We detect bulk magnetic properties and a maximal thickness of $d \approx 15$ nm for this growth method. The proposed growth method reduces the complexity, as the necessity to calibrate the oxygen pressure is circumvented. For films $d > 15$ nm the well known adsorption limited deposition method can be employed after the redox growth.

The electric properties of EuO/oxide heterostructures and a EuO/metal interface is analyzed. Performing ARPES on the EuO/SrTiO₃ interface, we detect a 2DEG which shows comparable properties as the classical 2DEGs, like e.g. LAO/SrTiO₃. Our approach provides two novel prospects. First the preparation of a 2DEG by a redox-controlled interface reaction and second the integration of a ferromagnetic insulator with the 2DEG. Hereby, a magnetically gated 2DEG is prepared. This interface could be interesting to study the transport properties and elucidate whether the 2DEG is spin-polarized. The integration of EuO with BaTiO₃ was studied in a second experiment. Again, a 2DEG is created by the redox process between Eu metal and BaTiO₃. This interface could be of special interest, as other studies have shown BaTiO₃ to retain its ferroelectric properties, while we find that $d_{\text{EuO}} = 2$ ML exhibits sizable magnetic properties. This combination with a 2DEG at the interface could pave the way towards a multiferroic device, as the EuO/BaTiO₃ interface could influence the magnetic properties

as a function of the ferroelectric polarization. The EuO/Pt interface reveals the opposite electric effect. Here a 2DHG is predicted by theoretical modeling and we measure with element specific HAX-XMCD and volumetric magnetometry an enhancement of the Curie temperature. This can be interpreted as a first sign of a magnetic interaction EuO/Pt interface interaction, which leads to the 2DHG.

The magnetic properties of Co/EuO heterostructures are studied with XMCD. We find that the sum rules can be applied to this rare earth material. We use this to determine the exchange length of the Co/EuO interface to $2\lambda_{AFM} = (5.6 \pm 1.4)$ nm, which shows that the effect is localized to the interface and only thin films of EuO will experience the Co/EuO exchange. Measuring a hysteresis loop at room temperature we observe ferromagnetic properties of EuO, far above its bulk $T_C = 69$ K. We utilize the hysteresis loop to obtain the Co/EuO exchange coupling strength $J = 0.278$ meV $\approx 5J_{bulk}$. We interpret this behavior as a magnetic proximity effect. A EuO ultra-thin film of $d_{EuO} = 2$ ML is prepared at room temperature and the Co/EuO interface is also studied. We obtain comparable results and $M(300\text{ K}) = 1 \mu_B/\text{f.u.}$. This shows that a significant magnetic moment is retained at room temperature even for ultra-thin EuO films.

Realizing a device as displayed in [Figure 7.1 \(a\)](#) may pave the way towards a room temperature spintronic application of EuO. In [Figure 7.1 \(b\)](#), the Ti $L_{3,2}$ edge is depicted. We observe an indication of Ti_2O_3 at the interface of EuO/SrTiO₃. This observation of reduced Ti^{3+} cations at the EuO/SrTiO₃ is an indicator for the presence of an interfacial 2DEG, as shown in [Section 5.1](#). Due to the observation of room temperature ferromagnetism of the Co/EuO heterostructure, spin injection into the interfacial 2DEG could become feasible. In the literature, the spin injection efficiency for EuO films down to 7ML thickness has been evaluated to be well above 90% [[11](#)], which indicates, that even for a 2ML EuO thick film sizable spin-polarized electron injection into SrTiO₃ could be possible.

Also, the 2DEG at the EuO/SrTiO₃ interface should be studied more closely and with spin ARPES to assess the spin character of the band structure. In the future, the additional gas feeds at the MBE system could be used to supply N, enabling the growth of nitrides. In conjunction with a second K-Cell filled with Gd metal the EuO/GdN interface could be studied. At this interface a topological state, a so called Chern insulator, is expected, as is published in the literature [[161](#)]. These states can be observed using ARPES, through the collaboration with a local photoemission group at FZ Jülich.

Another future experiment should be devoted to the study of the purported 2DHG at the Pt and EuO interface. We propose to study a buried EuO/Pt interface with HARPES. As we show in [Figure 2.11](#), Pt and Eu both have high Debye-Waller factors and therefore a study of these two elements can be a successful route to observe the 2DHG. This experiment could lead to the observation of a band structure as depicted in [Figure 7.1 \(c\)](#).

In conclusion, we developed a novel route to synthesize high quality EuO by utilizing a redox reaction with the substrate. this further enabled us to observe fascinating interfacial phenomena in oxide and metal heterostructures, ranging from two-dimensional conductivity to magnetic proximity effect induced room temperature ferromagnetism in EuO. This can open up new directions in EuO related research.

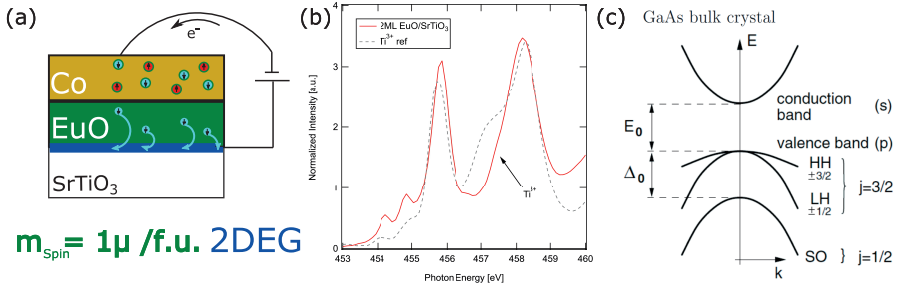


Figure 7.1.: Outlook on future experiments. (a) Sketch of a proposed room-temperature spin filter barrier based on a Co/EuO/SrTiO₃ structure. Here the spin filter injects the polarized electrons directly into a 2DEG at the SrTiO₃ interface. (b) XAS of Co/2ML EuO/SrTiO₃ heterostructure for the Ti L_{3,2} edge. As indicated by the arrow, a small contribution of Ti³⁺ like states is present, showing the signature of the previously studied 2DEG. (c) Exemplary band structure of a two dimensional hole gas in GaAs. [162]

A.1. Umweganregungen

As can be seen in [Figure 4.17](#) the rocking curve is not a simple Gaussian profile as would be expected. It shows a narrow spike at the center of the reflex. The FWHM of the spike is below the width of the substrate reflex as shown in [Figure 4.17](#). This leads to the conclusion, that neither the EuO reflex here measured nor the substrate can explain this observation. In fact this reflex is an artifact caused by so called Umweganregungen.

A ϕ -Scan of an out of plane reflex should show a uniform intensity for a full rotation, as the out of plane reflex is not dependent on the orientation of beam and substrate. Yet, [figure Figure A.1](#) shows that there is a strong dependency on the orientation. Around 0° there is an increase in intensity with a factor of about 100 with respect to the normal intensity.

This effect can be attributed to so called Umweganregungen as presented in 1937 by [\[163\]](#). The authors explain, that the narrow intensity spike is attributed to a double reflex of 2 allowed reflexes whose difference vector in reciprocal space is again the EuO (002) reflex such as e.g. SrTiO₃ (113) and $(-1 - 1 - 1)$.

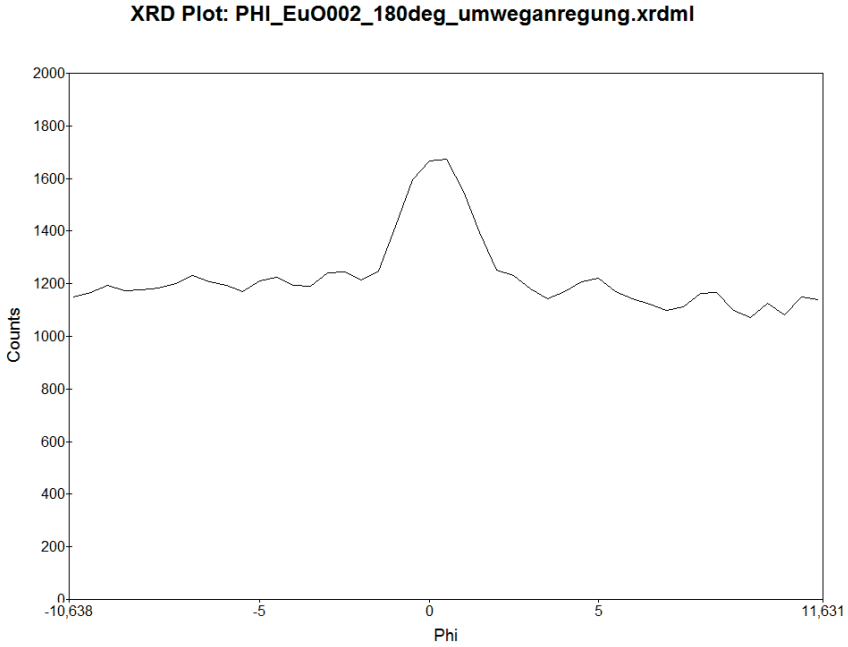


Figure A.1.: ϕ scan of the EuO (002) peak. As this peak has no in plane component, the intensity of the reflection should be constant. The spike along 0° indicates an Umweganregung - causing the sharp peak in the rocking curve found in 4.17.

Step	Process	Duration [min]	Comment
1	Isopropanol bath	3	ultrasound Setting 3
2	Acetone bath	3	ultrasound Setting 3
3	Water bath	3	ultrasound Setting 3
4	Blow dry		
5	BHF etch	0.5	
6	Isopropanol bath	3	upside down, ultrasound Setting 1
7	Acetone bath	3	ultrasound Setting 3
8	Anneal 950°C	120	heat in 90 min, switch off to cool

Table A.1.: Procedure of SrTiO_3 and Nb:SrTiO_3 preparation in the PGI-7 clean room based upon F. Gunkel's PhD thesis [37]. For BHF a VLSI type mixture with a dilution of 7:1 was used.

Bibliography

- [1] W. VAN HEDDEGHEM et al., “Trends in Worldwide ICT Electricity Consumption from 2007 to 2012”, *Computer Communications* **50**, 64, (2014) doi:10.1016/j.comcom.2014.02.008 (cited on page 1).
- [2] G. SCHMIDT et al., “Basic Obstacle for Electrical Spin-Injection from a Ferromagnetic Metal into a Diffusive Semiconductor”, *Physical Review B* **62**, 4, (1999) doi:10.1103/PhysRevB.62.R4790 (cited on page 2).
- [3] T. SANTOS, “Europium Oxide as a Perfect Electron Spin Filter”, PhD Thesis Massachusetts Institute of Technology, Department of Materials Science and Engineering (2007) (cited on pages 2, 34).
- [4] H. MIYAZAKI et al., “Fabrication of Single Crystalline EuO Thin Film with SrO Buffer Layer on SrTiO₃ Substrate”, *Journal of Physics: Conference Series* **391**, 012047, (2012) doi:10.1088/1742-6596/391/1/012047 (cited on pages 2, 30, 68).
- [5] H. MIYAZAKI et al., “Single Crystal Growth and Magnetic, Optical, and Photoelectrical Properties of EuO Thin Film”, *Japanese Journal of Applied Physics* **48**, 055504, (2009) doi:10.1143/JJAP.48.055504 (cited on pages 2, 68).
- [6] N. IWATA et al., “Preparation and Magnetic Properties of EuO Thin Films Epitaxially Grown on MgO and SrTiO₃ Substrates”, *Journal of the Physical Society of Japan* **69**, 230, (2000) doi:10.1143/JPSJ.69.230 (cited on pages 2, 68, 76).
- [7] G. M. PRINZ et al., “Quantum Confinement in EuO Heterostructures”, *Applied Physics Letters* **109**, 202401, (2016) doi:10.1063/1.4966223 (cited on page 2).
- [8] A. OHTOMO and H. Y. HWANG, “A High-Mobility Electron Gas at the LaAlO₃/SrTiO₃ Heterointerface”, *Nature* **427**, 423, (2004) doi:10.1038/nature02308 (cited on pages 2, 84).

- [9] W. HAN et al., “*Spin Injection and Detection in Lanthanum- and Niobium-Doped SrTiO₃ Using the Hanle Technique.*”, *Nature communications* **4**, 2134 (2013) doi:10.1038/ncomms3134 (cited on pages 2, 29).
- [10] A. G. SWARTZ et al., “*Spin-Dependent Transport across Co/LaAlO₃/SrTiO₃ Heterojunctions*”, *Applied Physics Letters* **105**, 032406, (2014) doi:10.1063/1.4891174 (cited on page 2).
- [11] N. JUTONG et al., “*Electronic Transport through EuO Spin-Filter Tunnel Junctions*”, *Physical Review B - Condensed Matter and Materials Physics* **86**, 1 (2012) doi:10.1103/PhysRevB.86.205310 (cited on pages 2, 10, 34, 106, 116).
- [12] COLLABORATION: AUTHORS AND EDITORS OF THE VOLUMES III/17G-41D, in *Non-Tetrahedrally Bonded Binary Compounds II*, Vol. 41D, edited by O. MADELUNG, U. RÖSSLER, and M. SCHULZ (Springer-Verlag, Berlin/Heidelberg, 2000), pages 1–18, ISBN: 978-3-540-64966-3, doi:10.1007/10681735_588 (cited on page 6).
- [13] F. KARLSRUHE, *Inorganic Crystal Structure Database*, (2017) <https://icsd.fiz-karlsruhe.de/search/index.xhtml> (cited on pages 5, 99).
- [14] P. STEENEKEN, “New Light on EuO Thin Films” (Rijksuniversiteit Groningen, 2002) (cited on pages 6, 7, 56, 85).
- [15] T. MAIROSER et al., “*High-Quality EuO Thin Films the Easy Way via Topotactic Transformation*”, *Nature Communications* **6**, 7716, (2015) doi:10.1038/ncomms8716 (cited on pages 6, 56, 68).
- [16] S. BLUNDELL, *Magnetism In Condensed Matter*, Oxford Master Series In Physics (2000), ISBN: 978-0-19-850591-4 (cited on pages 7, 8).
- [17] J. KLINKHAMMER et al., “*Spin-Polarized Surface State in EuO(100)*”, *Physical Review Letters* **112**, 1 (2014) doi:10.1103/PhysRevLett.112.016803 (cited on page 8).
- [18] A. MAUGER and C. GODART, “*The Magnetic, Optical, and Transport Properties of Representatives of a Class of Magnetic Semiconductors: The Europium Chalcogenides*”, *Physics Reports* **141**, 51, (1986) doi:10.1016/0370-1573(86)90139-0 (cited on pages 8, 112).
- [19] R. SCHILLER and W. NOLTING, “*Prediction of a Surface State and a Related Surface Insulator-Metal Transition for the (100) Surface of Stoichiometric EuO*”, *Physical Review Letters* **86**, 3847, (2001) doi:10.1103/PhysRevLett.86.3847 (cited on pages 8, 9, 41, 64, 87, 95).
- [20] M. HOPPE, “Magnetic, Structural, and Electronic Properties of NiFe₂O₄ Ultrathin Films”, Duisburg, Univ, Diss., 2015, Dr. (Duisburg, Univ, Jülich, 2016) (cited on page 9).

-
- [21] W. BUTLER et al., “Spin-Dependent Tunneling Conductance of Fe/MgO/Fe Sandwiches”, *Physical Review B* **63**, 054416, (2001) doi:10.1103/PhysRevB.63.054416 (cited on page 10).
- [22] N. HAMPP, “Temperaturabhängigkeit von Enthalpie H Und Entropie S ”, Apr. 2009 (cited on page 12).
- [23] M. HONG et al., “Surface Diffusion on SrTiO₃ (100): A Temperature Accelerated Dynamics and First Principles Study”, *Surface Science* **617**, 237 (2013) doi:10.1016/j.susc.2013.08.002 (cited on pages 12, 30, 79).
- [24] A. EINSTEIN, “Über Einen Die Erzeugung Und Verwandlung Des Lichtes Betreffenden Heuristischen Gesichtspunkt”, *Annalen der Physik* **322**, 132, (1905) doi:10.1002/andp.19053220607 (cited on page 16).
- [25] S. HÜFNER, *Photoelectron Spectroscopy*, Advanced Texts in Physics (Springer Berlin Heidelberg, Berlin, Heidelberg, 2003), ISBN: 978-3-642-07520-9 978-3-662-09280-4, doi:10.1007/978-3-662-09280-4 (cited on pages 16, 17, 19).
- [26] E.-J. CHO et al., “Origin of the High-Binding-Energy Structure in the 3d Core-Level Spectra of Divalent Eu Compounds”, *Physical Review B* **51**, 10146, (1995) doi:10.1103/PhysRevB.51.10146 (cited on pages 20, 52, 59, 87, 93).
- [27] T. VALLA, “Evidence for Quantum Critical Behavior in the Optimally Doped Cuprate Bi₂Sr₂CaCu₂O₈+”, *Science* **285**, 2110, (1999) doi:10.1126/science.285.5436.2110 (cited on page 20).
- [28] S. TANUMA, C. J. POWELL, and D. R. PENN, “Calculations of Electron Inelastic Mean Free Paths. IX. Data for 41 Elemental Solids over the 50 eV to 30 keV Range”, *Surface and Interface Analysis* **43**, 689, (2011) doi:10.1002/sia.3522 (cited on pages 21, 22).
- [29] J. MAIBACH et al., “Electric Potential Gradient at the Buried Interface between Lithium-Ion Battery Electrodes and the SEI Observed Using Photoelectron Spectroscopy”, *The Journal of Physical Chemistry Letters* **7**, 1775, (2016) doi:10.1021/acs.jpcclett.6b00391 (cited on page 21).
- [30] C. S. FADLEY, “X-Ray Photoelectron Spectroscopy and Diffraction in the Hard X-Ray Regime: Fundamental Considerations and Future Possibilities”, *Nuclear Instruments and Methods in Physics Research Section A: Accelerators, Spectrometers, Detectors and Associated Equipment* **547**, 24, (2005) doi:10.1016/j.nima.2005.05.009 (cited on page 21).
- [31] J. WOJCIK, editor, *Hard X-Ray Photoelectron Spectroscopy (HAXPES)*, Vol. 59, Springer Series in Surface Sciences (Springer International Publishing, Cham, 2016), ISBN: 978-3-319-24041-1 978-3-319-24043-5, doi:10.1007/978-3-319-24043-5 (cited on pages 22, 23).

- [32] K. G. SUBHADRA, B. RAGHAVENDRA RAO, and D. B. SIRDESHMUKH, “X-Ray Determination of the Debye-Waller Factors and Debye Temperatures of Europium Monochalcogenides”, *Pramana* **38**, 681, (1992) doi:10.1007/BF02875064 (cited on pages 22, 23).
- [33] G. VAN DER LAAN and A. I. FIGUEROA, “X-Ray Magnetic Circular Dichroism—A Versatile Tool to Study Magnetism”, *Coordination Chemistry Reviews* **277-278**, 95, (2014) doi:10.1016/j.ccr.2014.03.018 (cited on pages 24, 47).
- [34] J. STÖHR and H. C. SIEGMANN, *Magnetism: From Fundamentals to Nanoscale Dynamics*, Vol. 152, Springer Series in Solid-State Sciences (Springer Berlin Heidelberg, 2006), 1 page, ISBN: 3-540-30282-4 (cited on page 24).
- [35] J. F. WATTS and J. WOLSTENHOLME, *An Introduction to Surface Analysis by XPS and AES* (John Wiley & Sons, Ltd, Chichester, UK, Mar. 25, 2003), ISBN: 978-0-470-86793-8 (cited on pages 25, 63).
- [36] F. SÁNCHEZ, C. OCAL, and J. FONTCUBERTA, “Tailored Surfaces of Perovskite Oxide Substrates for Conducted Growth of Thin Films”, *Chemical Society Reviews* **43**, 2272, (2014) doi:10.1039/c3cs60434a (cited on pages 28–30).
- [37] F. GUNKEL, “The Role of Defects at Functional Interfaces between Polar and Non-Polar Perovskite Oxides” (RWTH Aachen University, Aachen, 2013) (cited on pages 29, 120).
- [38] J. G. CONNELL et al., “Preparation of Atomically Flat SrTiO₃ Surfaces Using a Deionized-Water Leaching and Thermal Annealing Procedure”, *Applied Physics Letters* **101**, 251607, (2012) doi:10.1063/1.4773052 (cited on page 29).
- [39] M. KAREEV et al., “Atomic Control and Characterization of Surface Defect States of TiO₂ Terminated SrTiO₃ Single Crystals”, *Applied Physics Letters* **93**, 061909, (2008) doi:10.1063/1.2971035 (cited on page 29).
- [40] G. KOSTER et al., “Quasi-Ideal Strontium Titanate Crystal Surfaces through Formation of Strontium Hydroxide”, *Applied Physics Letters* **73**, 2920, (1998) doi:10.1063/1.122630 (cited on pages 29, 85).
- [41] K. SZOT and W. SPEIER, “Surfaces of Reduced and Oxidized SrTiO₃ from Atomic Force Microscopy”, *Physical Review B* **60**, 5909, (1999) doi:10.1103/PhysRevB.60.5909 (cited on page 30).
- [42] PRINSEN, “Nucleation and Growth on SrTiO₃ Substrates Characterize by Ex-Situ AFM” (2007) (cited on page 31).

-
- [43] A. PICOLIN, “Wasser Auf Ungestuften Und Gestuften Platinflächen”, Diploma (Universität zu Köln, May 2008) (cited on pages 32, 33).
- [44] M. MÜLLER, G.-X. MIAO, and J. S. MOODERA, “*Thickness Dependence of Ferromagnetic- and Metal-Insulator Transition in Thin EuO Films*”, *Journal of Applied Physics* **105**, 07C917, (2009) doi:10.1063/1.3063673 (cited on pages 34, 64, 85).
- [45] M. MÜLLER, G.-X. MIAO, and J. S. MOODERA, “*Exchange Splitting and Bias-Dependent Transport in EuO Spin Filter Tunnel Barriers*”, *EPL (Europhysics Letters)* **88**, 47006, (2009) doi:10.1209/0295-5075/88/47006 (cited on pages 34, 56, 87).
- [46] K. NEUREITER, “Entwicklung Und Elektrische Charakterisierung von Oxid-Basierten Transportstrukturen”, Master Thesis (Universität Duisburg-Essen, Jan. 3, 2017) (cited on page 34).
- [47] A. NAUMKIN et al., *NIST X-Ray Photoelectron Spectroscopy Database*, (Sept. 12, 2012) <https://srdata.nist.gov/xps/Default.aspx> (visited on 09/23/2017) (cited on page 35).
- [48] J. A. BEARDEN, “*X-Ray Wavelengths*”, *Reviews of Modern Physics* **39**, 78, (1967) doi:10.1103/RevModPhys.39.78 (cited on page 35).
- [49] M. ESCHBACH, “Band Structure Engineering in 3D Topological Insulators Investigated by Angle-Resolved Photoemission Spectroscopy”, Dr. (Duisburg, Jülich, 2016) (cited on page 35).
- [50] G. RIJNDERS, “The Initial Growth of Complex Oxides : Study and Manipulation” (2001) (cited on pages 36, 37).
- [51] F. JONA, J. A STROZIER, and W. S. YANG, “*Low-Energy Electron Diffraction for Surface Structure Analysis*”, *Reports on Progress in Physics* **45**, 527 (2000) doi:10.1088/0034-4885/45/5/002 (cited on pages 37, 38).
- [52] R. HAMMER et al., “*Surface Reconstruction of Pt(001) Quantitatively Revisited*”, *Physical Review B* **94**, (2016) doi:10.1103/PhysRevB.94.195406 (cited on pages 38, 100).
- [53] Y. A. ABRAMOV et al., “*The Chemical Bond and Atomic Displacements in SrTiO₃ from X-Ray Diffraction Analysis*”, *Acta Crystallographica Section B Structural Science* **51**, 942, (1995) doi:10.1107/S0108768195003752 (cited on page 39).
- [54] ASYLUM, *Arrow NCR*, (2017) <https://afmprobes.asylumresearch.com/arrow-ncr.html> (visited on 09/23/2017) (cited on page 38).
- [55] D. NEČAS and P. KLAPETEK, “*Gwyddion: An Open-Source Software for SPM Data Analysis*”, *Open Physics* **10**, (2012) doi:10.2478/s11534-011-0096-2 (cited on page 39).

- [56] M. FALEY, in *Applications of High-Tc Superconductivity*, edited by A. LUIZ (InTech, June 27, 2011), ISBN: 978-953-307-308-8, doi:10.5772/16302 (cited on page 39).
- [57] O. PETRACIC and B. SCHMITZ, *Crosscalibration of Dynacool and MPMS*, 2016 (cited on page 40).
- [58] S. G. ALTENDORF et al., “*Oxygen Off-Stoichiometry and Phase Separation in EuO Thin Films*”, *Physical Review B - Condensed Matter and Materials Physics* **84**, 155442 (2011) doi:10.1103/PhysRevB.84.155442 (cited on pages 41, 105).
- [59] L. SPIESS et al., *Moderne Röntgenbeugung* (Vieweg+Teubner, Wiesbaden, 2009), 5 pages, ISBN: 978-3-8351-0166-1 (cited on pages 41–43, 99).
- [60] M. H. MENDENHALL et al., “*High-Precision Measurement of the x-Ray Cu K γ Spectrum*”, *Journal of Physics B: Atomic, Molecular and Optical Physics* **50**, 115004, (2017) doi:10.1088/1361-6455/aa6c4a (cited on page 42).
- [61] C. KITTEL, editor, *Introduction to Solid State Physics*, 8th ed., english (Wiley, New York, NY, 2005), ISBN: 978-0-471-68057-4 (cited on page 42).
- [62] F. SCHAEFERS, M. MERTIN, and M. GORGOI, “*KMC-1: A High Resolution and High Flux Soft x-Ray Beamline at BESSY*”, *Review of Scientific Instruments* **78**, 123102, (2007) doi:10.1063/1.2808334 (cited on page 44).
- [63] M. GORGOI et al., “*The High Kinetic Energy Photoelectron Spectroscopy Facility at BESSY Progress and First Results*”, *Nucl. Instr. Meth. Phys. Res. A* **601**, 48, (2009) doi:http://dx.doi.org/10.1016/j.nima.2008.12.244 (cited on pages 44, 58).
- [64] J. STREMPFER et al., “*Fast Helicity Switching of X-Ray Circular Polarization at Beamline P09 at PETRA III*”, in (2016), page 030017, doi: 10.1063/1.4952840 (cited on page 45).
- [65] A. GLOSKOVSKII et al., “*Magnetometry of Buried Layers-Linear Magnetic Dichroism and Spin Detection in Angular Resolved Hard X-Ray Photoelectron Spectroscopy*”, *Journal of Electron Spectroscopy and Related Phenomena* **185**, 47 (2012) doi:10.1016/j.elspec.2011.11.005 (cited on page 45).
- [66] J. STREMPFER et al., “*Resonant Scattering and Diffraction Beamline P09 at PETRA III*”, *Journal of Synchrotron Radiation* **20**, 541, (2013) doi: 10.1107/S0909049513009011 (cited on page 45).
- [67] SCHLÜTER, *Beamline Parameters*, (2017) http://photon-science.desy.de/facilities/petra_iii/beamlines/p09_resonant_scattering_and_diffraction/beamline_specifications/index_eng.html (visited on 09/25/2017) (cited on page 45).

-
- [68] F. BERTRAN, *Cassiopeé Beamline and Endstations*, (2017) <https://www.synchrotron-soleil.fr/en/beamlines/cassiopee> (visited on 09/26/2017) (cited on page 45).
- [69] H. WANG et al., “Complete Polarization Analysis of an APPLE II Undulator Using a Soft X-Ray Polarimeter”, *Journal of Synchrotron Radiation* **19**, 944, (2012) doi:10.1107/S0909049512034851 (cited on page 47).
- [70] W. H. HOCKING and J. A. D. MATTHEW, “Electron Spectroscopy of Europium”, *Journal of Physics: Condensed Matter* **2**, 3643, (1990) doi:10.1088/0953-8984/2/15/019 (cited on page 51).
- [71] C. CASPERS, “Magnetic Oxide Heterostructures : EuO on Cubic Oxides and on Silicon” (2013), 152 pages (cited on pages 51, 58, 59, 79).
- [72] M. W. SHAFER, “Preparation and Crystal Chemistry of Divalent Europium Compounds”, *Journal of Applied Physics* **36**, 1145, (1965) doi:10.1063/1.1714142 (cited on page 55).
- [73] M. BARBAGALLO et al., “Thickness-Dependent Magnetic Properties of Oxygen-Deficient EuO”, *Physical Review B* **84**, (2011) doi:10.1103/PhysRevB.84.075219 (cited on pages 55, 97, 98).
- [74] G.-X. MIAO, M. MÜLLER, and J. S. MOODERA, “Magnetoresistance in Double Spin Filter Tunnel Junctions with Nonmagnetic Electrodes and Its Unconventional Bias Dependence”, *Phys. Rev. Lett.* **102**, 076601 (2009) doi:10.1103/PhysRevLett.102.076601 (cited on page 56).
- [75] R. B. H. TAHAR et al., “Tin Doped Indium Oxide Thin Films: Electrical Properties”, *J. Appl. Phys.* **83**, 2631 (1998) (cited on page 56).
- [76] M. MATSUBARA et al., “Giant Third-Order Magneto-Optical Rotation in Ferromagnetic EuO”, *Phys. Rev. B* **86**, 195127 (2012) doi:10.1103/PhysRevB.86.195127 (cited on page 56).
- [77] G. KOSTER, M. HUIJBEN, and G. RIJNDERS, editors, *Epitaxial Growth of Complex Metal Oxides*, 1st edition (Woodhead Publishing, 2015) (cited on page 56).
- [78] R. W. ULBRICHT et al., “Adsorption-Controlled Growth of EuO by Molecular-Beam Epitaxy”, *Applied Physics Letters* **93**, 102105, (2008) doi:10.1063/1.2973180 (cited on pages 56, 85).
- [79] R. SUTARTO et al., “Epitaxial and Layer-by-Layer Growth of EuO Thin Films on Yttria-Stabilized Cubic Zirconia (001) Using MBE Distillation”, *Physical Review B* **79**, (2009) doi:10.1103/PhysRevB.79.205318 (cited on pages 56, 61).

- [80] D. F. FÖRSTER, “EuO and Eu on Metal Crystals and Graphene: Interface Effects and Epitaxial Films”, Inaugural (Universität zu Köln, Köln, Oct. 14, 2011) (cited on page 56).
- [81] C. CASPERS et al., “Chemical Stability of the Magnetic Oxide EuO Directly on Silicon Observed by Hard X-Ray Photoemission Spectroscopy”, *Physical Review B* **84**, (2011) doi:10.1103/PhysRevB.84.205217 (cited on page 56).
- [82] C. CASPERS et al., “Heteroepitaxy and Ferromagnetism of EuO/MgO (001): A Route towards Combined Spin- and Symmetry-Filter Tunneling”, *Physical Review B* **88**, (2013) doi:10.1103/PhysRevB.88.245302 (cited on pages 56, 85, 87).
- [83] C. CASPERS et al., “Ultrathin Magnetic Oxide EuO Films on Si(001) Using SiO_x Passivation-Controlled by Hard x-Ray Photoemission Spectroscopy”, *Journal of Applied Physics* **113**, 17C505 (2013) doi:10.1063/1.4795010 (cited on page 56).
- [84] A. SCHMEHL et al., “Epitaxial Integration of the Highly Spin-Polarized Ferromagnetic Semiconductor EuO with Silicon and GaN”, *Nature Materials* **6**, 882 (2007) doi:10.1038/nmat2012 (cited on page 56).
- [85] D. V. AVERYANOV et al., “Direct Epitaxial Integration of the Ferromagnetic Semiconductor EuO with Silicon for Spintronic Applications”, *ACS Applied Materials & Interfaces* **7**, 6146 (2015) doi:10.1021/am5089007 (cited on page 56).
- [86] K. J. HUBBARD and D. G. SCHLOM, “Thermodynamic Stability of Binary Oxides in Contact with Silicon”, *J. Mater. Res.* **11**, 2757 (1996) (cited on page 56).
- [87] D. G. SCHLOM and J. H. HAENI, “A Thermodynamic Approach to Selecting Alternative Gate Dielectrics”, *MRS bulletin* **27**, 198 (2002) (cited on page 56).
- [88] L. P. H. JEURGENS et al., “Thermodynamic Stability of Amorphous Oxide Films on Metals: Application to Aluminum Oxide Films on Aluminum Substrates”, *Phys. Rev. B* **62**, 4707 (2000) doi:10.1103/PhysRevB.62.4707 (cited on page 56).
- [89] C. S. FADLEY, “X-Ray Photoelectron Spectroscopy: Progress and Perspectives”, *Journal of Electron Spectroscopy and Related Phenomena* **178-179**, 2, (2010) doi:10.1016/j.elspec.2010.01.006 (cited on page 57).
- [90] J. ZEGENHAGEN, “Photoelectron Spectroscopy of Transition Metal Oxide Interfaces”, *Eur. Phys. J.-Appl. Phys.* **70**, 20701 (2015) (cited on page 57).

-
- [91] H. OHTA et al., “*Highly Electrically Conductive Indium–Tin–Oxide Thin Films Epitaxially Grown on Yttria-Stabilized Zirconia (100) by Pulsed-Laser Deposition*”, *Appl. Phys. Lett.* **76**, 2740 (2000) doi:<http://dx.doi.org/10.1063/1.126461> (cited on pages 57, 59).
- [92] C. BUCHAL et al., “*Epitaxial BaTiO₃ Thin Films on MgO*”, *Mater. Sci. Eng. B* **56**, 234 (1998) (cited on pages 57, 91).
- [93] M. QUAAS et al., “*Investigation of Diffusion and Crystallization Processes in Thin ITO Films by Temperature and Time Resolved Grazing Incidence X-Ray Diffractometry*”, *Surf. Sci.* **540**, 337 (2003) (cited on page 61).
- [94] M. BURGNER and A. GOLDMANN, “*Oxidation of Ultrathin Indium Layers on W(110) - A Core-Level Photoemission Study*”, *Surf. Sci.* **540**, 89 (2003) doi:[10.1016/S0039-6028\(03\)00775-1](https://doi.org/10.1016/S0039-6028(03)00775-1) (cited on page 62).
- [95] V. CHRISTOU et al., “*High Resolution X-Ray Photoemission Study of Plasma Oxidation of Indium–Tin–Oxide Thin Film Surfaces*”, *J. Appl. Phys.* **88**, 5180 (2000) doi:<http://dx.doi.org/10.1063/1.1312847> (cited on page 62).
- [96] C. POWELL and A. JABLONSKI, “*Surface Sensitivity of X-Ray Photoelectron Spectroscopy*”, *Nuclear Instruments and Methods in Physics Research Section A: Accelerators, Spectrometers, Detectors and Associated Equipment* **601**, 54 (2009) doi:[10.1016/j.nima.2008.12.103](https://doi.org/10.1016/j.nima.2008.12.103) (cited on page 63).
- [97] W. S. M. WERNER, W. SMEKAL, and C. J. POWELL, editors, *NIST Database for the Simulation of Electron Spectra for Surface Analysis, Version 2.0* (National Institute of Standards and Technology, 2014) (cited on page 63).
- [98] R. J. KONINGS et al., “*The Thermodynamic Properties of the F-Elements and Their Compounds. Part 2. The Lanthanide and Actinide Oxides*”, *J. Phys. Chem. Ref. Data* **43**, 013101 (2014) doi:[10.1063/1.4825256](https://doi.org/10.1063/1.4825256) (cited on page 64).
- [99] W. M. HAYNES, *CRC Handbook of Chemistry and Physics*, 95th edition (CRC press, 2013) (cited on page 64).
- [100] H. J. T. ELLINGHAM, “*Reducibility of Oxides and Sulphides in Metallurgical Processes*”, *J. Soc. Chem. Ind.* **63**, 125 (1944) doi:[10.1002/jctb.5000630501](https://doi.org/10.1002/jctb.5000630501) (cited on pages 65, 68).
- [101] P. S. MANNING et al., “*The Kinetics of Oxygen Transport in 9.5 Mol% Single Crystal Yttria Stabilised Zirconia*”, *Solid State Ion.* **100**, 1, (1997) doi:[http://dx.doi.org/10.1016/S0167-2738\(97\)00345-7](http://dx.doi.org/10.1016/S0167-2738(97)00345-7) (cited on page 66).
- [102] K. L. NGAI, J. SANTAMARIA, and C. LEON, “*Dynamics of Interacting Oxygen Ions in Yttria Stabilized Zirconia: Bulk Material and Nanometer Thin Films*”, *Eur. Phys. J. B* **86**, 1 (2013) (cited on page 66).

- [103] C. MITRA et al., “*Electronic Structure of Oxygen Vacancies in SrTiO₃ and LaAlO₃*”, *Physical Review B* **86**, (2012) doi:10.1103/PhysRevB.86.155105 (cited on page 69).
- [104] N. CABRERA and N. F. MOTT, “*Theory of the Oxidation of Metals*”, *Reports on Progress in Physics* **12**, 163, (1949) doi:10.1088/0034-4885/12/1/308 (cited on page 73).
- [105] J. KRUGER and H. T. YOLKEN, “*Room Temperature Oxidation of Iron at Low Pressures*”, *CORROSION* **20**, 29t, (1964) doi:10.5006/0010-9312-20.1.29t (cited on page 73).
- [106] M. ADACHI et al., in *Oxides*, Vol. 36A1, edited by Y. SHIOZAKI, E. NAKAMURA, and T. MITSUI (Springer-Verlag, Berlin/Heidelberg, 2002), pages 1–7, ISBN: 978-3-540-63274-0, doi:10.1007/10426842_33 (cited on page 80).
- [107] D. N. MÜLLER, *Private Communication*, E-mail (cited on page 80).
- [108] Y. WANG et al., “*Prediction of a Spin-Polarized Two-Dimensional Electron Gas at the LaAlO₃ / EuO (001) Interface*”, *Physical Review B* **79**, (2009) doi:10.1103/PhysRevB.79.212408 (cited on page 80).
- [109] K. D. FREDRICKSON and A. A. DEMKOV, “*Spin-Polarized, Orbital-Selected Hole Gas at the EuO/Pt Interface*”, *Journal of Applied Physics* **119**, 095309, (2016) doi:10.1063/1.4942837 (cited on pages 83, 97, 99, 102, 104).
- [110] S. THIEL, “*Tunable Quasi-Two-Dimensional Electron Gases in Oxide Heterostructures*”, *Science* **313**, 1942, (2006) doi:10.1126/science.1131091 (cited on page 84).
- [111] K. UENO et al., “*Electric-Field-Induced Superconductivity in an Insulator*”, *Nature Materials* **7**, 855, (2008) doi:10.1038/nmat2298 (cited on page 84).
- [112] H. NAKAMURA et al., “*Tuning of Metal–Insulator Transition of Quasi-Two-Dimensional Electrons at Parylene/SrTiO₃ Interface by Electric Field*”, *Journal of the Physical Society of Japan* **78**, 083713, (2009) doi:10.1143/JPSJ.78.083713 (cited on page 84).
- [113] N. REYREN et al., “*Superconducting Interfaces Between Insulating Oxides*”, *Science* **317**, 1196, (2007) doi:10.1126/science.1146006 (cited on page 84).
- [114] A. BRINKMAN et al., “*Magnetic Effects at the Interface between Non-Magnetic Oxides*”, *Nature Materials* **6**, 493, (2007) doi:10.1038/nmat1931 (cited on page 84).
- [115] A. D. CAVIGLIA et al., “*Electric Field Control of the LaAlO₃/SrTiO₃ Interface Ground State*”, *Nature* **456**, 624, (2008) doi:10.1038/nature07576 (cited on page 84).

-
- [116] A. D. CAVIGLIA et al., “Tunable Rashba Spin-Orbit Interaction at Oxide Interfaces”, *Physical Review Letters* **104**, (2010) doi:10.1103/PhysRevLett.104.126803 (cited on page 84).
- [117] A. JOSHUA et al., “Gate-Tunable Polarized Phase of Two-Dimensional Electrons at the LaAlO₃/SrTiO₃ Interface”, *Proceedings of the National Academy of Sciences* **110**, 9633, (2013) doi:10.1073/pnas.1221453110 (cited on page 84).
- [118] T. D. NGO et al., “Polarity-Tunable Magnetic Tunnel Junctions Based on Ferromagnetism at Oxide Heterointerfaces”, *Nature Communications* **6**, 8035, (2015) doi:10.1038/ncomms9035 (cited on page 84).
- [119] E. LESNE et al., “Highly Efficient and Tunable Spin-to-Charge Conversion through Rashba Coupling at Oxide Interfaces”, *Nature Materials* **15**, 1261, (2016) doi:10.1038/nmat4726 (cited on page 84).
- [120] Q. SONG and H. ZHANG, “Observation of Inverse Edelstein Effect in Rashba-Split 2DEG between SrTiO₃ and LaAlO₃ at Room Temperature”, eprint arXiv:1609.06207 (2016) (cited on page 84).
- [121] D. STORNAIUOLO et al., “Tunable Spin Polarization and Superconductivity in Engineered Oxide Interfaces”, *Nature Materials advance on*, **1** (2015) doi:10.1038/nmat4491 (cited on page 84).
- [122] V. T. TRA et al., “Ferroelectric Control of the Conduction at the LaAlO₃ / SrTiO₃ Heterointerface”, *Advanced Materials* **25**, 3357, (2013) doi:10.1002/adma.201300757 (cited on page 84).
- [123] A. F. SANTANDER-SYRO et al., “Two-Dimensional Electron Gas with Universal Subbands at the Surface of SrTiO₃”, *Nature* **469**, 189, (2011) doi:10.1038/nature09720 (cited on pages 84, 86, 88, 89, 94).
- [124] W. MEEVASANA et al., “Creation and Control of a Two-Dimensional Electron Liquid at the Bare SrTiO₃ Surface”, *Nature Materials* **10**, 114, (2011) doi:10.1038/nmat2943 (cited on pages 84, 88).
- [125] A. F. SANTANDER-SYRO et al., “Orbital Symmetry Reconstruction and Strong Mass Renormalization in the Two-Dimensional Electron Gas at the Surface of KTaO₃”, *Physical Review B* **86**, (2012) doi:10.1103/PhysRevB.86.121107 (cited on pages 84, 88).
- [126] C. BAREILLE et al., “Two-Dimensional Electron Gas with Six-Fold Symmetry at the (111) Surface of KTaO₃”, *Scientific Reports* **4**, (2015) doi:10.1038/srep03586 (cited on pages 84, 88).
- [127] A. F. SANTANDER-SYRO et al., “Giant Spin Splitting of the Two-Dimensional Electron Gas at the Surface of SrTiO₃”, *Nature Materials* **13**, 1085, (2014) doi:10.1038/nmat4107 (cited on page 84).

- [128] T. C. RÖDEL et al., “Engineering Two-Dimensional Electron Gases at the (001) and (101) Surfaces of TiO₂ Anatase Using Light”, *Physical Review B* **92**, (2015) doi:10.1103/PhysRevB.92.041106 (cited on pages 84, 88).
- [129] E. FRANTZESKAKIS et al., “2D Surprises at the Surface of 3D Materials: Confined Electron Systems in Transition Metal Oxides”, *Journal of Electron Spectroscopy and Related Phenomena* **219**, 16, (2017) doi:10.1016/j.elspec.2016.10.001 (cited on page 84).
- [130] T. TANIUCHI et al., “Imaging of Room-Temperature Ferromagnetic Nano-Domains at the Surface of a Non-Magnetic Oxide”, *Nature Communications* **7**, 11781, (2016) doi:10.1038/ncomms11781 (cited on page 84).
- [131] T. C. RÖDEL et al., “Universal Fabrication of 2D Electron Systems in Functional Oxides”, *Advanced Materials* **28**, 1976, (2016) doi:10.1002/adma.201505021 (cited on pages 85, 86, 88–90, 94).
- [132] C. T. CAMPBELL, “Metal Films and Particles on Oxide Surfaces: Structural, Electronic and Chemisorptive Properties”, *Journal of the Chemical Society, Faraday Transactions* **92**, 1435, (1996) doi:10.1039/ft9969201435 (cited on page 85).
- [133] T. GERBER et al., “Thermodynamic Stability and Control of Oxygen Reactivity at Functional Oxide Interfaces: EuO on ITO”, *J. Mater. Chem. C* **4**, 1813, (2016) doi:10.1039/C6TC00170J (cited on pages 85, 87).
- [134] R. SUTARTO, “EuO and Gd – Doped EuO Thin Films : Epitaxial Growth and Properties” (2009) (cited on page 85).
- [135] D. F. FÖRSTER et al., “Epitaxial Europium Oxide on Ni(100) with Single-Crystal Quality”, *Physical Review B* **83**, (2011) doi:10.1103/PhysRevB.83.045424 (cited on page 85).
- [136] C. CASPERS et al., “Electronic Structure of EuO Spin Filter Tunnel Contacts Directly on Silicon”, *Physica Status Solidi - Rapid Research Letters* **5**, 441 (2011) doi:10.1002/pssr.201105403 (cited on pages 85, 87).
- [137] C. CASPERS et al., “Interface Engineering to Create a Strong Spin Filter Contact to Silicon”, *Scientific Reports* **6**, (2016) doi:10.1038/srep22912 (cited on page 85).
- [138] G. M. PRINZ et al., “Quantum Confinement in EuO Heterostructures”, *Applied Physics Letters* **109**, 202401, (2016) doi:10.1063/1.4966223 (cited on page 85).
- [139] T. C. RÖDEL, “Two-Dimensional Electron Systems in Functional Oxides Studied by Photoemission Spectroscopy” (Université Paris-Saclay, Saint-Aubin, Sept. 8, 2016) (cited on pages 88, 94).

-
- [140] C. CHEN et al., “*Observation of a Two-Dimensional Liquid of Fröhlich Polarons at the Bare SrTiO₃ Surface*”, *Nature Communications* **6**, 8585, (2015) doi:10.1038/ncomms9585 (cited on page 88).
- [141] Z. WANG et al., “*Tailoring the Nature and Strength of Electron–phonon Interactions in the SrTiO₃(001) 2D Electron Liquid*”, *Nature Materials*, (2016) doi:10.1038/nmat4623 (cited on page 89).
- [142] S. CAO et al., “*Magnetoelectric Coupling at the EuO/BaTiO₃ Interface*”, *Applied Physics Letters* **102**, 172402 (2013) doi:10.1063/1.4803492 (cited on page 90).
- [143] R. L. KURTZ and V. E. HENRICH, “*UHV-Cleaved Single Crystal Ti₂O₃ (101-2) by UPS and XPS*”, *Surface Science Spectra* **5**, 182, (1998) doi:10.1116/1.1247849 (cited on page 93).
- [144] R. SCHILLER, “*Correlation Effects and Temperature Dependencies in Thin Ferromagnetic Films: Magnetism and Electronic Structure*” (2000), 110 pages (cited on page 95).
- [145] J. SON, J. CAGNON, and S. STEMMER, “*Strain Relaxation in Epitaxial Pt Films on (001) SrTiO₃*”, *Journal of Applied Physics* **106**, 043525, (2009) doi:10.1063/1.3207795 (cited on page 98).
- [146] M. E. SCHRADER, “*Young-Dupre Revisited*”, *Langmuir* **11**, 3585, (1995) doi:10.1021/la00009a049 (cited on page 99).
- [147] M. B. YAZDI et al., “*Possible Evidence for a Spin-State Crossover in the Verwey State in Fe₃O₄ Thin Films*”, *Physical Review B* **93**, (2016) doi:10.1103/PhysRevB.93.014439 (cited on page 104).
- [148] S. D. PAPPAS et al., “*Direct Evidence for Significant Spin-Polarization of EuS in Co/EuS Multilayers at Room Temperature.*”, *Scientific reports* **3**, 1333 (2013) doi:10.1038/srep01333 (cited on pages 105, 106).
- [149] T. KONNO et al., “*Structure and Magnetic Properties of Fe/EuO Granular Films*”, *Materials Science and Engineering: A* **217-218**, 331, (1996) doi:10.1016/S0921-5093(96)10328-2 (cited on page 106).
- [150] C. T. CHEN et al., “*Experimental Confirmation of the X-Ray Magnetic Circular Dichroism Sum Rules for Iron and Cobalt*”, *Physical Review Letters* **75**, 152, (1995) doi:10.1103/PhysRevLett.75.152 (cited on pages 106, 107).
- [151] C. WÄCKERLIN et al., “*Strong Antiferromagnetic Exchange between Manganese Phthalocyanine and Ferromagnetic Europium Oxide*”, *Chem. Commun.* **51**, 12958, (2015) doi:10.1039/C5CC01823D (cited on pages 106, 107, 112).

- [152] B. T. THOLE et al., “*X-Ray Circular Dichroism as a Probe of Orbital Magnetization*”, *Physical Review Letters* **68**, 1943, (1992) doi:10.1103/PhysRevLett.68.1943 (cited on page 106).
- [153] P. CARRA et al., “*X-Ray Circular Dichroism and Local Magnetic Fields*”, *Physical Review Letters* **70**, 694, (1993) doi:10.1103/PhysRevLett.70.694 (cited on page 106).
- [154] F. BLOCH, “*Zur Theorie Des Ferromagnetismus*”, *Zeitschrift für Physik* **61**, 206, (1930) doi:10.1007/BF01339661 (cited on page 112).
- [155] C. CHIEN and D. H. REICH, “*Proximity Effects in Superconducting/Magnetic Multilayers*”, *Journal of Magnetism and Magnetic Materials* **200**, 83, (1999) doi:10.1016/S0304-8853(99)00318-2 (cited on page 114).
- [156] O. RADER et al., “*Fe-Induced Magnetization of Pd: The Role of Modified Pd Surface States*”, *Physical Review Letters* **72**, 2247, (1994) doi:10.1103/PhysRevLett.72.2247 (cited on page 114).
- [157] J. VAN LIEROP et al., “*Proximity Effects in an Exchange-Biased Ni 80 Fe 20 / Co 3 O 4 Thin Film*”, *Physical Review B* **75**, (2007) doi:10.1103/PhysRevB.75.134409 (cited on page 114).
- [158] F. MACCHEROZZI et al., “*Evidence for a Magnetic Proximity Effect up to Room Temperature at Fe / (Ga , Mn) As Interfaces*”, *Physical Review Letters* **101**, (2008) doi:10.1103/PhysRevLett.101.267201 (cited on page 114).
- [159] E. JOHNSTON-HALPERIN et al., “*Spin-Polarized Zener Tunneling in (Ga,Mn)As*”, *Physical Review B* **65**, (2002) doi:10.1103/PhysRevB.65.041306 (cited on page 114).
- [160] A. LIECHTENSTEIN et al., “*Local Spin Density Functional Approach to the Theory of Exchange Interactions in Ferromagnetic Metals and Alloys*”, *Journal of Magnetism and Magnetic Materials* **67**, 65, (1987) doi:10.1016/0304-8853(87)90721-9 (cited on page 114).
- [161] K. F. GARRITY and D. VANDERBILT, “*Chern Insulator at a Magnetic Rocksalt Interface*”, *Physical Review B* **90**, (2014) doi:10.1103/PhysRevB.90.121103 (cited on page 116).
- [162] WINKLER, *Spin-Orbit Coupling Effects in Two-Dimensional Electron and Hole Systems*, Springer Tracts in Modern Physics (Springer-Verlag, Berlin Heidelberg, 2003) (cited on page 117).
- [163] M. RENNIGER, “*Umweganregung*”, *Eine Bisher Unbeachtete Wechselwirkungerscheinung Bei Raumgitterinterferenzen*”, *Zeitschrift für Physik* **106**, 141 (1937) doi:10.1007/BF01340315 (cited on page 119).

Own Publications

- [1] T. GERBER et al., “*Thermodynamic Stability and Control of Oxygen Reactivity at Functional Oxide Interfaces: EuO on ITO*”, *J. Mater. Chem. C* **4**, 1813, (2016) doi:10.1039/C6TC00170J.
- [2] P. LÖMKER et al., “*Two-Dimensional Electron System at the Magnetically Tunable EuO/SrTiO₃ Interface*”, *Physical Review Materials*, Rapid Communications **1**, 062001(R) (2017).

Conference Contributions

- [1] P. LÖMKER, “*Redox Controlled Magnetic Oxide Hybrids: EuO on SrTiO₃(001)*”, 7th International Conference on Hard X-Ray Photoelectron Spectroscopy, Nov. 9, 2017.
- [2] P. LÖMKER, “*Tunable Redox-Created 2DES at the EuO/SrTiO₃ Interface*”, DPG Frühjahrstagung, Mar. 24, 2017.
- [3] P. LÖMKER, “*Utilizing Substrate Properties for Oxygen “Free” Growth of EuO on SrTiO₃*”, 8th Joint BER II and BESSY II User Meeting, Aug. 12, 2016.
- [4] P. LÖMKER, “*Introducing Magnetic Functionality into Oxide Heterostructures by Thermodynamic Stabilization: EuO/SrTiO₃*”, DPG Frühjahrstagung, Oct. 3, 2016.
- [5] P. LÖMKER, “*Electronic Structure and Ferromagnetic Properties of Al EuO SrTiO₃ Heterostructures*”, 580. WEH Seminar - Oxide Spintronics, July 1, 2015.

Patrick Lömker

Curriculum Vitae

Personal data

Date of birth **19th January 1990**
Place of birth **Leverkusen**
Nationality **German**

Experience

since 11/2014 **Forschungszentrum Jülich GmbH, Jülich**
PhD student at the Peter-Grünberg-Institut (PGI-6)
10/2013 - 09/2014 **Forschungszentrum Jülich GmbH, Jülich**
Master student at the Peter-Grünberg-Institut (PGI-6)
01/2013 - 09/2013 **Head Acoustics GmbH, Herzogenrath**
Student assistant in the acoustics research department
10/2011 - 03/2012 **RWTH Aachen University, Aachen**
Student assistant at the Institute for Solid State Physics
10/2007 - 10/2008 **University of Cologne, Cologne**
High school student at the university
08/2006 - 06/2007 **Saint John's Jesuit High School, Toledo, OH, USA**
Exchange student programme

Education

since 11/2014 **Technical University Dortmund, Dortmund**, PhD student in Physics
10/2012 - 09/2014 **RWTH Aachen University, Aachen**, Physics, Qualification: Master of Science in Physics
10/2009 - 09/2012 **RWTH Aachen University, Aachen**, Physics
Qualification: Bachelor of Science in Physics
06/2000 - 06/2009 **Otto-Hahn Gymnasium, Monheim am Rhein**
Qualification: Abitur
06/1996 - 06/2000 **Geschwister-Scholl-Grundschule, Monheim am Rhein**

Voluntary Social Service

10/2014 - present **Die Johanniter, Aachen**
Leader of the disaster relief team
03/2010 - present **Die Johanniter, Aachen**
Volunteer in a disaster relief team
11/2009 - 11/2013 **RWTH Aachen University, Aachen**
Active participant in the student body for Physics at RWTH Aachen University, organization of first year's events.

Eidesstattliche Versicherung

Ich, Patrick Lömker, geb. 19.01.1990 in Leverkusen, versichere an Eides statt, dass die vorliegende Doktorarbeit eigenständig erstellt wurde und alle in Anspruch genommenen Quellen und Hilfen in der Dissertation vermerkt wurden.



Patrick Lömker, Aachen, 30.10.2017

Erklärung

Die vorliegende Doktorarbeit wurde weder vollständig noch in Teilen in der gegenwärtigen oder in einer anderen Fassung an der Technischen Universität Dortmund oder an einer anderen Hochschule im Zusammenhang mit einer staatlichen oder akademischen Prüfung bereits vorgelegt.



Patrick Lömker, Aachen, 30.10.2017

Acknowledgment

This work has been greatly benefited from many people which I would like to acknowledge:

- Martina Müller, for enabling research of this interesting topic in the scope of her engaging Young Investigators Group, initiating and continuing cooperations with numerous international scientists and research facilities. Thankyou also for your ongoing support.
- Carsten Westphal, for the interest in the topic and for agreeing to take up the second referee
- Wolfgang Rhode, for chairing the promotion examination
- Catalin Gainaru, for agreeing to take up the role of the scientific member of the examiners
- Katrin Neureiter, who contributed to this work with her master thesis
- Correction readers: Tim Flatten, Tristan Heider, Ronja Hinz, Mai Hussein and Marek Wilhelm

I thank Claus Michael Schneider for providing a very good working environment in his institute PGI-6@FZ Jülich. The colleagues from PGI-6@FZ Jülich have provided my work with a great atmosphere. In particular I want to thank Umut Parlak for his help preparing Pt/SrTiO₃ substrates. The technical support from Thomas Jansen, Heinz Peiffer and Norbert Schnitzler was invaluable - thank you!

I want to thank especially Timm Gerber, who was an excellent colleague and discussion partner. Further more I thank the present and former colleagues in the Young Investigators Group.

The discussions on thermodynamic potentials with Claire Besson and David Müller were very insightful and lead to the idea of oxygen-free growth of EuO on SrTiO₃ - thank you very much for your support!

The collaboration with Andres Santander-Syro, Tobias Chris Rödel, Emmanuel Frantzeskakis and Ji Dai has lead to great results for the ARPES studies of 2DEGs between SrTiO₃ and BaTiO₃.

The support of synchrotron measurements was excellent and I want to thank the beamline staff at the beamlines:

- KMC-1 (BESSY, HZB, Berlin): Mihaela Gorgoi
- P09 (PETRA III, DESY, Hamburg): Anrei Gloskovskii, Christoph Schlueter and Wolfgang Drube, and
- I10 (Diamond Light Source, Didcot): Peter Bencok and Paul Steadman.

I thank Jürgen Schubert for his support with discussions on X-ray diffraction and preparation of PLD grown thin films of indium tin oxide and BaTiO₃.

I thank Thomas Brückel for being able to use the magnetometers at JCNS-2/PGI-4 and Oleg Petravic for discussions on magnetism.

Last but not least, I want to dearly thank my family and friends, for all their support and that I have the high honor of having them.

Band / Volume 160

***Corynebacterium glutamicum* – a novel platform for the production of plant polyphenols**

N. Kallscheuer (2018), X, 98 pp

ISBN: 978-3-95806-291-7

Band / Volume 161

Neurons on 3D polymer nanostructures

A. Belu (2018), vii, 135 pp

ISBN: 978-3-95806-296-2

Band / Volume 162

Tailoring and Characterisation of Bioelectronic Interfaces

A. Markov (2018), 75 pp

ISBN: 978-3-95806-298-6

Band / Volume 163

Epitaxy of group IV Si-Ge-Sn alloys for advanced heterostructure light emitters

N. von den Driesch (2018), viii, 149 pp

ISBN: 978-3-95806-300-6

Band / Volume 164

Impact and Regulatory Control of the CGP3 Prophage in *Corynebacterium glutamicum*

E. Pfeifer (2018), IV, 206 pp

ISBN: 978-3-95806-301-3

Band / Volume 165

Establishment of Bacterial Microcompartments in the Industrial Production Strain *Corynebacterium glutamicum*

I. Huber (2018), X, 114, XI-XXXIV pp

ISBN: 978-3-95806-302-0

Band / Volume 166

Current-Induced Magnetization Dynamics in Ferromagnetic Nanowires

M. I. Khan (2018), vi, 138 pp

ISBN: 978-3-95806-308-2

Band / Volume 167

Management of Electrophysiological Data & Metadata

Making complex experiments accessible to yourself and others

L. Zehl (2018), 182 pp

ISBN: 978-3-95806-311-2

Band / Volume 168

**Investigation of GeSn as Novel Group IV
Semiconductor for Electronic Applications**

C. Schulte-Braucks, Christian (2018), xx, 165, XII pp
ISBN: 978-3-95806-312-9

Band / Volume 169

**Tailoring the Electronic Properties of Epitaxial Oxide Films
via Strain for SAW and Neuromorphic Applications**

Y. Dai (2018), VI, 133 pp
ISBN: 978-3-95806-319-8

Band / Volume 170

**The electronic structure of transition metal dichalcogenides investigated
by angle-resolved photoemission spectroscopy**

M. Gehlmann (2018), ii, 108, XVIII pp
ISBN: 978-3-95806-324-2

Band / Volume 171

Control of neuron adhesion by metal nanoparticles

A. Q. Tran (2018), viii, 108 pp
ISBN: 978-3-95806-332-7

Band / Volume 172

Neutron Scattering

Lectures of the JCMS Laboratory Course held at Forschungszentrum Jülich
and at the Heinz-Maier-Leibnitz Zentrum Garching
edited by T. Brückel, S. Förster, G. Roth, and R. Zorn (Eds.) (2018),
ca 300 pp
ISBN: 978-3-95806-334-1

Band / Volume 173

Spin scattering of topologically protected electrons at defects

P. Rüßmann (2018), vii, 230 pp
ISBN: 978-3-95806-336-5

Band / Volume 174

Interfacing EuO in confined oxide and metal heterostructures

P. Lömker (2018), vi, 140 pp
ISBN: 978-3-95806-337-2

Weitere **Schriften des Verlags im Forschungszentrum Jülich** unter
<http://www.zb1.fz-juelich.de/verlagextern1/index.asp>

Schlüsseltechnologien / Key Technologies
Band / Volume 174
ISBN 978-3-95806-337-2